A statistical framework for the characterisation of WIMP dark matter with the LUX-ZEPLIN experiment

Imperial College London

Ibles Olcina Samblas

Department of Physics

A thesis submitted for the degree of

Doctor of Philosophy

November 2019

Abstract

Several pieces of astrophysical evidence, from galactic to cosmological scales, indicate that most of the mass in the universe is composed of an invisible and essentially collisionless substance known as dark matter. A leading particle candidate that could provide the role of dark matter is the Weakly Interacting Massive Particle (WIMP), which can be searched for directly on Earth via its scattering off atomic nuclei. The LUX-ZEPLIN (LZ) experiment, currently under construction, employs a multi-tonne dual-phase xenon time projection chamber to search for WIMPs in the low background environment of the Davis Campus at the Sanford Underground Research Facility (South Dakota, USA). LZ will probe WIMP interactions with unprecedented sensitivity, starting to explore regions of the WIMP parameter space where new backgrounds are expected to arise from the elastic scattering of neutrinos off xenon nuclei.

In this work the theoretical and computational framework underlying the calculation of the sensitivity of the LZ experiment to WIMP-nucleus scattering interactions is presented. After its planned 1000 live days of exposure, LZ will be able to achieve a 3σ discovery for spin independent cross sections above $3.0 \times 10^{-48}\,\mathrm{cm}^2$ at $40\,\mathrm{GeV/c^2}$ WIMP mass or exclude at 90% CL a cross section of $1.3 \times 10^{-48}\,\mathrm{cm}^2$ in the absence of signal. The sensitivity of LZ to spin-dependent WIMP-neutron and WIMP-proton interactions is also presented. All the sensitivity projections are calculated using the `LZStats` software package, which is discussed in detail in this thesis. In addition, this work classifies key systematic uncertainties by their impact on the WIMP sensitivity and motivates the inclusion of the highest-ranked into the analysis likelihood function. The effect of some of these systematics on the reconstruction of the WIMP cross section is also studied and it is found to be sub-dominant.

Declaration

I hereby declare that the contents in this thesis are my own work, except where explicit reference is made to the work of others. My specific contributions in each chapter are listed below.

Chapter 2 reviews the main pieces of evidence favouring the dark matter hypothesis and the different types of WIMP searches are discussed. All the figures in this chapter are borrowed from the references indicated in the caption, except for Figure 2.5, which is my own.

Chapter 3 describes direct detection WIMP searches with a liquid xenon time projection chamber and presents the main characteristics of the LZ experiment. In this chapter I compared the prediction of the liquid xenon yields between the two most used (until recently) versions of the NEST software package: libNEST `5.0.0` and NEST `v2.0.0`. I used NEST in combination with a parametrisation of the LZ detector system, which is based on the extensive body of simulations described in the LZ Technical Design Report [1] that were done by LZ collaborators, to generate probability density functions as a function of S1 and S2 observables. This allowed me to give an estimation of the electron recoil discrimination in LZ. Also, I presented the main background contributions to the WIMP search in Table 3.3, which are based on a similar table developed by the LZ collaboration in Ref. [2], but it contains the most up-to-date estimates.

In Chapter 4 I presented the `LZStats` package, which I developed and has become a key analysis tool used by the LZ collaboration. Although I have been the main developer of the code for most of my PhD, I got valuable input from other members of the collaboration and the original design was partly based on previous work developed by Alastair Currie and Attila Dobi. I was responsible for implementing the spin-independent and spin-dependent calculations, described in Chapter 3, into `LZStats`. Then, and in collaboration with other LZ members, we calculated the sensitivity projections shown in Ref. [2] (submitted for publication). This chapter describes that calculation in detail and provides the most up-to-date sensitivity projections.

Chapter 5 describes an analysis of the systematic uncertainties that are expected to be most relevant for the projected performance of the LZ experiment. I presented the relative impact of each systematic uncertainty ranked by the combined impact when the nominal value is shifted by 1σ in either direction. This is my own work, but it was inspired by similar studies conducted by the ATLAS and CMS collaborations, amongst others.

The copyright of this thesis rests with the author and is made available under a Creative Commons Attribution Non-Commercial No Derivatives licence. Researchers are free to copy, distribute or transmit the thesis on the condition that they attribute it, that they do not use it for commercial purposes and that they do not alter, transform or build upon it. For any reuse or redistribution, researchers must make clear to others the licence terms of this work.

Ibles Olcina Samblas
November 2019

Acknowledgements

There are so many people that have accompanied me in this journey and whose support was vital to make the writing of this thesis possible. I would like to thank first my colleagues at Imperial: Brais, Nellie and Rob (and our beloved plant Lidia too!). You became my second family, and you made the PhD experience a great deal more exciting. Also, I would like to extend my gratitude to those who I shared the corridor with at some point, and who made me grow both professionally and personally: Alfredo, Francis and Alastair.

I also would like to thank my supervisor Henrique, who has been my physics (plus grammar, math and politics) educator during the entire duration of the PhD. You have been a source of constant inspiration and I feel fortunate of having had the opportunity to work closely with you.

Special thanks go to all the members of the LZ collaboration, whose dedication and hard work have been inspiring since the very beginning. With an almost certain 100% probability that I will forget to mention someone, I would like to acknowledge those people who I have interacted with more closely over the past years and who I have enjoyed dearly working with: Asher, Jim, Hugh, Maria Elena, Aaron, Carmen, Theresa, Cees, Umit, Sally, Nicolas, Amy, Maria Francesa, Elizabeth, Athoy, Curt, Ben K. , Björn, Greg, Jordan, Luke, Quentin, Andrew S. , Andew N. , Scott H. and Billy. Also, I would like to extend my thanks to Glen Cowan, who put everything in order in my very disorganised mental section on statistics.

I would like to thank the President's PhD Scholarship for kindly funding my studies at Imperial College London. I am grateful of the friends I have made because of this incredible opportunity and of the warm community of fellow scholars that I found right from the beginning of my PhD.

I would also like to thank, hoping not to appear too pedantic, those great composers who have brought so much enjoyment to my life. Vivaldi, Beethoven and Sarasate always gave me the strength back when I most needed it, while Brahms, Schubert and Bach made me levitate from my seat in those long hours sitting in front of the computer. Also, thank you Liam for teaching me how to *enjoy* playing music.

Thanks Pedro for always bringing that aura of knowledge around you, from which I somehow still managed to learn one thing or two. For starters, I would not be writing this thesis in `Vim` (and secretly enjoying it), if it wasn't for you. Thanks also to all my former flatmates for all the great moments that we shared: Andy, Dani and Chris (plus the regular visitors to the Fort Comfort: Alan, Ignacio, Mada, Dylan, Irene, Erica and Zhiyu). I learned something valuable from each of you.

This would not have been possible without that amazing group of friends that I feel so fortunate to have around me. Thanks for all the support you have given me and for holding on there waiting during my (embarrassingly frequent) long silences during the writing period. Thanks Guillem, Arianna, Alex C. , Alex B. , Ruben, Elias, Irene, Bea and Sarah.

I don't have words to describe my gratitude towards Julie and Duncan. You have done so much for me and I will always carry your affection wherever I go. Also, my special thanks to Alan, Katie and Polly for turning the big and scary city of London into a cosy and friendly environment.

Thanks also to my family for the immeasurable love you have given me. I always felt your proximity despite the distance, and your support and undertanding has been my refuge for years. Gràcies Freix, Violeta i Joansa de tot cor.

And of course you, senyoreta meua. You deserve half the credit for this thesis (maybe more). Tú encengueres la flama.

"Tot està per fer, tot és possible avui."
Miquel Martí i Pol

Contents

List of figures

List of tables

Symbols and Acronyms

Greek Symbols

$\boldsymbol{\alpha}$ Parameters of interest

$\boldsymbol{\nu}$ Nuisance parameters

$\boldsymbol{\theta}$ Model parameters

μ_j Mean of likelihood component j

Other Symbols

$\mathscr{L}$ Likelihood function

$\mathscr{D}$ Data set

$\mathcal{N}$ Normal probability distribution

Roman Symbols

$\boldsymbol{g}_p$ Vector of global observables for the nuisance parameter ν_p

$\boldsymbol{x}_e$ Vector of observables for event e

n_0 Number of events in a data set

w Critical region

Acronyms

AGN Active Galactic Nuclei

ALP Axion-Like Particle

BAO Baryon Acoustic Oscillations

BAU	Baryon Asymmetry of the Universe
BBN	Big Bang Nucleosynthesis
CDM	Cold Dark Matter
CEνNS	Coherent Elastic Neutrino-Nucleus Scattering
CJPL	China Jinping Underground Laboratory
CL	Confidence Level
CMB	Cosmic Microwave Background
DEC	Double Electron Capture
DM	Dark Matter
ER	Electron Recoil
GW	Gravitational Waves
GXe	Gaseous Xenon
HDM	Hot Dark Matter
ICV	Inner Cryostat Vessel
LHC	Large Hadron Collider
LN	Liquid Nitrogen
LNGS	Laboratory Nazionali del Gran Sasso
LSP	Lightest Supersymmetric Particle
LSS	Large Scale Structure
LXe	Liquid Xenon
LZ	LUX-ZEPLIN
MACHO	Massive Astronomical Halo Object
MLE	Maximum Likelihood Estimator

MOND Modified Newtonian Dynamics

MSDM Minimal Simplified Dark Matter model

MSSM Minimal Supersymmetric Standard Model

nEDM Neutron Electric Dipole Moment

NEST Noble Element Simulation Technique

NIR Near Infrared

NP Nuisance Parameter

NR Nuclear Recoil

OCV Outer Cryostat Vessel

OD Outer Detector

PBH Primordial Black Hole

PCL Power-Constrained Limit

PDE Photon Detection Efficiency

PDF Probability Density Function

PLR Profile Likelihood Ratio

pMSSM Phenomenological Minimal Supersymmetric Standard Model

PMT Photomultiplier Tube

POI Parameter Of Interest

PQ Peccei-Quinn symmetry

PTFE Polytetrafluoroethylene

QCD Quantum Chromodynamics

RFR Reverse-Field Region

RMS Root Mean Square

S1	Prompt scintillation signal in the liquid phase
S2	Delayed proportional scintillation signal in the gas phase
SD	Spin Dependent
SE	Single Electron
SHM	Standard Halo Model
SI	Spin Independent
SM	Standard Model
SURF	Sanford Underground Research Facility
SUSY	Supersymmetry
TDR	Technical Design Report
TPC	Time Projection Chamber
UED	Universal Extra Dimensions
VUV	Vacuum Ultraviolet
WIMP	Weakly Interacting Massive Particle

Chapter 1

Introduction

There is a large and growing body of evidence that indicates that most of the mass in the universe is composed of a non-baryonic, gravitationally-interacting and invisible substance: dark matter. In fact, there is approximately five times as much dark matter than ordinary (baryonic) matter. This is accounted for in the predominant theory of cosmology, the ΛCDM model, which entails the existence of large amounts of cold dark matter that clump gravitationally and guide ordinary matter to coalesce into the large scale structure that we observe in the present universe. The ΛCDM model continues to withstand stricter tests from ever more precise astronomical observations, but non-gravitational interactions of dark matter have not been conclusively observed yet.

One suitable hypothesis that explains the observational evidence is that dark matter is composed of one, or several, new particles outside of the Standard Model of particle physics. Other ideas have been suggested, such as modifying our understanding of the laws of gravity, but these have not been as successful as the particle interpretation at explaining the wide range of evidence. Dark matter particles are currently being sought in colliders (the LHC), in searches for annihilation products in the cosmos and in direct searches of weak-force mediated scatters off nuclei. In this thesis we focus our attention on direct searches, and we explore their sensitivity to a well-motivated class of dark matter particles: WIMPs.

WIMPs are expected to interact very weakly with ordinary matter. They could, in principle, scatter off nuclei and create measurable nuclear recoils (NR) in the target medium at the core of a radiation detector. Although their predicted scattering rates are extraordinarily small, of less than 1 event per year and kilogram of target, their detection is in principle possible with experiments that employ ultra-low background detectors installed beneath a large rock overburden (underground or inside a mountain). By contrast, the majority of background sources will create electron recoil (ER) events, and their predicted rates are considerably higher.

The LUX-ZEPLIN (LZ) experiment constitutes a major effort in this front. LZ will start operations in 2020, and it will accumulate 1000 live days of exposure with a liquid xenon time projection chamber (LXe-TPC) that contains approximately 7 tonnes of liquid xenon. With this exposure, LZ will probe WIMP interactions before a significant (and perhaps irreducible) background sets in due to coherent nuclear scattering of astrophysical neutrinos.

This thesis is organised as follows. Chapter 2 starts with a historical account on the "issue" of dark matter. The idea that luminous matter in the universe is exceeded by matter that neither absorbs nor emits light has a long history, but it was generally dismissed by the scientific community for decades. This gradually changed as more evidence appeared, and in this chapter we highlight the main discoveries that led to the establishment of dark matter as the accepted model. Additionally, we motivate the particle interpretation of dark matter and we discuss three well-motivated particle candidates: WIMPs, axions and sterile neutrinos. The chapter concludes with the description of three different types of WIMP detection techniques, namely, direct searches, indirect searches and collider searches.

In Chapter 3 we delve into direct searches of WIMPs, focusing our attention on one of the leading detection instruments: the dual-phase (liquid and gas) xenon time projection chamber. The chapter begins with a description of the different elements that are involved in the calculation of the WIMP-induced event rate. We emphasise the canonical WIMP-nucleus elastic scattering calculation, but we point to other alternatives too. The chapter continues with a discussion on the emission mechanisms of light and charge in liquid xenon, followed by the description of the operational principle of the dual-phase xenon TPC. An overview of the LZ experiment, highlighting its various detector systems and the dominant background contributions to the WIMP search, concludes the chapter. In addition, simulated data from two key calibration sources are discussed to assess the expected ER discrimination level of the LZ experiment.

Chapter 4 presents the projected LZ sensitivity to WIMP dark matter. After introducing some statistical terminology, the `LZStats` software package is presented. This is a generic software framework that provides straightforward procedures to conduct statistical analyses that are of general interest within the direct detection community. The code is being used extensively by LZ analysers and this represents an important contribution of my own to the collaboration. The chapter continues with the presentation of results from the calculation of the projected WIMP sensitivity using `LZStats`. These results are then compared to previous sensitivity projections published by the LZ collaboration and the origin of any differences is discussed.

Chapter 5 explores the impact that some key systematic uncertainties have on the sensitivity projections presented in the previous chapter. Accounting for some of these sources of uncertainty in the statistical analysis might be computationally expensive. Therefore, the goal of this study is to classify the sources of uncertainty by their impact on the WIMP sensitivity and motive the inclusion into the analysis likelihood of only those with the highest ranking. In addition, we investigate how some of these uncertainties affect the reconstruction of the WIMP cross section in a scenario where a discovery has been firmly established.

The conclusions are presented in Chapter 6, where we summarise the main findings of this work and discuss future improvements.

Chapter 2

Dark matter

The idea of "dark matter" has seen a profound transformation over the last century. Presently, those words are most likely used to refer to any of the particle species that are believed to account for the majority of mass in the universe. This is in stark contrast with the use of the phrase several decades ago, when the word "dark" was merely an adjective used to describe those astronomical objects that were not bright enough to be detected by a telescope.

In this chapter we review how we arrived at the modern concept of dark matter, highlighting in the process some of the key pieces of evidence that support the existence of this unknown, but abundant, substance. Furthermore, the main properties of dark matter are explained and some of the leading particle candidates are presented. The chapter concludes with a summary of the different experimental strategies that currently exist to search for one of the prime dark matter candidates: weakly interacting massive particles, or WIMPs.

2.1 A jigsaw puzzle

The concept of dark matter (DM) is deeply ingrained in our understanding of modern cosmology. Despite early hints for the existence of this invisible substance, it was only a few decades ago that it came to be accepted as the standard explanation for a broad spectrum of astrophysical and cosmological observations. In fact, the "dark matter problem" has evolved over the last century from a minor observational puzzle to a major challenge for cosmology, astrophysics and particle physics. We begin by highlighting some of the key evidence pointing towards the existence of dark matter.

Several methods exist to estimate the mass of an astronomical body. On the one hand, the mass could be estimated from the brightness of the object. On the other hand, the motions of other bodies around or inside the object of study could also be used to infer its mass. At the beginning of the 20th century, some astronomers started to realise that the mass estimates from the second method exceeded those from the first one by a large factor. This apparent discrepancy between the gravitational mass of a celestial object and its luminous mass drove some scientists to hypothesise the existence of "dark matter", which at the time was defined as matter that is not bright enough to be observed from Earth.

One such measurement came from Zwicky in 1933, when he was studying the *internal motion of galaxies* within the Coma cluster [3]. He observed an unusually large dispersion in the radial velocities of the individual galaxies that he measured, of the order of $1000\,\mathrm{km/s}$. Using the best estimation existing at the time of the average mass and size of a galaxy, he applied the virial theorem to independently estimate the total kinematic energy of the cluster, inferring from this a velocity dispersion of only $80\,\mathrm{km/s}$. This estimate was in striking contrast with the measured value, and he concluded:

> *"If this should be verified, it would lead to the surprising result that dark matter exists in much greater density than luminous matter."*

This sentence is sometimes cited as the first reference to the phrase "dark matter", but that is incorrect. Previous astronomers, such as Kapteyn, Oort and Jeans, had already suggested the idea that there could be dark matter within our own galaxy and elsewhere [4]. Although there were several issues with Zwicky's original calculation from a modern perspective, his claim that the Coma cluster exhibits a large mass-to-light ratio has survived to the present day.

Shortly after, Smith reported the observation of a similar effect in the Virgo Cluster, where estimations of its dynamical mass exceeded significantly those of its luminous mass [5]. Nevertheless, such claims were treated with great scepticism by the scientific community at the time. For instance, this is an extract from an article of 1940 by Holmberg, who was a contemporary of Zwicky and Smith [6]:

> *"It does not seem to be possible to accept the high velocities [in the Virgo and Coma cluster] as belonging to permanent cluster members, unless we suppose that the greater part of the total mass of the cluster is contributed by dark material distributed among the cluster members—an unlikely assumption."*

However, the scientists' perception of dark matter started to change when new data appeared regarding the *rotation curves of spiral galaxies*. A galactic rotation curve tracks the circular velocity of objects within a galaxy as a function of their distance to the galactic centre. Most importantly, the mass distribution of the galaxy can be estimated from its rotation curve under some reasonably simple assumptions.

In the middle of the 20th century, Oort and Hulst managed to measure a significant large fraction of the rotation curve of the Andromeda galaxy, or M31. They benefited from two technological innovations to carry out their studies: a vast array of military radars that were abandoned after World War II [7], and the discovery of the 21-cm emission line from neutral hydrogen [8]. Their results indicated that the rotation curve of the Andromeda galaxy appeared to be almost "flat" at large radii. Such measurement was completely at odds with the classical Keplerian interpretation, which predicts a roll-off of the rotation curve at large radii. Later, in the 1970s, a plethora of rotation curve measurements using both optical and radio data started to appear, mainly led by the pioneering work of Rubin and Ford [9]. Such measurements not only confirmed the flatness of the rotation curve of the Andromeda galaxy at distances far beyond the edge of the visible disc (Figure 2.1), but showed that several other spiral galaxies followed a similar behaviour too [10].

The implications of the observed flatness in galactic rotation curves were immense, and many astronomers started to argue that the actual edge of spiral galaxies might be far beyond the optical bulge. In fact, these puzzling observations could be explained by assuming that spiral galaxies were embedded in a halo of dark matter extending to large radii, as suggested for instance by Rubin, Ford and Thonnard in 1978 [11]:

> *"Such models imply that the galaxy mass increases significantly with increasing radius, which in turn requires that rotational velocities remain high for large radii. The observations presented here are thus a necessary but not sufficient condition for massive halos."*

However, this is not the only explanation that was proposed to explain the flatness of rotation curves in spiral galaxies. In 1982, Milgrom suggested a simple but consequential idea: what if Newton's second law did not hold in the limit of very low accelerations? Under this new theoretical framework he demonstrated that the flat rotation curves could be explained without having to introduce any dark matter component [14, 15]. This proposal came to be known as Modified Newtonian Dynamics, or MOND in short. However, it proved to be extremely challenging to embed MOND within a complete relativistic theory of gravity, and it was not until 2004 that Bekenstein introduced a relativistic version of MOND, the so-called TeVeS theory [16].

Despite the success of MOND-like theories in explaining observations at galactic scale, they have not been nearly as successful on the scale of galactic clusters. According to the general theory of relativity, matter can bend and focus light, an effect that is referred to as *gravitational lensing*. It is currently possible to study the mass profile of galactic clusters by measuring the gravitational lensing effects originating from the bending of light by the cluster

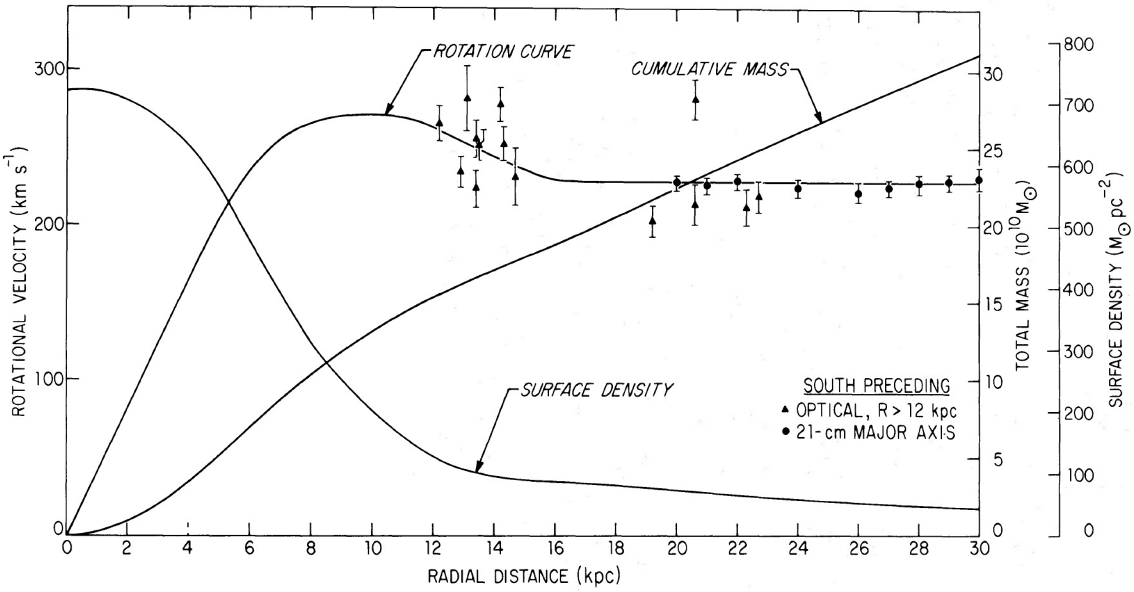

Figure 2.1: The rotation curve of Andromeda galaxy, also known as M31. Results from both optical measurements [9] (filled triangles) and 21-cm radio measurements [12] (filled circles) are shown. The rotation curve remains almost constant over radial distances of 16 kpc to 30 kpc, which is beyond the optical bulge of the galaxy. Figure from Ref. [13].

mass distribution [17]. In the past two decades, several cases have been reported where the comparison of the weak gravitational lensing and X-ray maps of a galactic cluster reveals that the distribution of baryons is manifestly detached from the dominant gravitational potential of the system. The "Bullet Cluster" is a prime example of such observations and due to the special properties regarding the formation of this cluster, it provides evidence that dark matter behaves as an essentially collisionless component not only with ordinary matter, but also with itself [18].

Such clear observations of the separation between luminous and non-luminous mass in galactic clusters are difficult to explain by the MOND hypothesis. Alternatively, the dark matter hypothesis offers a plausible explanation: the distribution of mass estimated via weak gravitational lensing is mainly due to this invisible substance that behaves differently than baryons. In addition, the recent coincident observation of gravitational waves (GW) and electromagnetic radiation from a neutron merger [19, 20] has effectively ruled out TeVeS [21, 22], which predicts a difference between the propagation velocity of gravitational waves and gamma-rays larger than has been observed.

There is also evidence for dark matter at cosmological scales. In 1965, the *cosmic microwave background* (CMB) radiation was discovered [23, 24], which is a nearly isotropic radiation of microwave photons. The CMB radiation is very accurately represented by a Planck blackbody spectrum with temperature $T = 2.728 \pm 0.004$ K, as measured by the COBE satellite in the 1990s [25]. This radiation was released shortly after the epoch of "recombination", when the first neutral hydrogen atoms were formed and photons were allowed to travel freely through the universe. Earlier than this, photons were being constantly scattered by free electrons and the universe was opaque. Therefore, the CMB radiation is the oldest "snapshot" that we have of the universe and its discovery represented an emphatic triumph of the Big Bang theory.

The CMB radiation has a wealth of information encrypted on it about the history of the universe, providing some of the tightest constraints on cosmological parameters. However, initial measurements of the CMB radiation by the COBE satellite were not precise enough to make any meaningful inference of cosmological parameters. The situation changed in the 2000s with the WMAP satellite [26], which was launched in 2001 and took data for 9 years, and later the Planck satellite [27], which was launched in 2009 and took data for 3 years. First WMAP, and then Planck, mapped the temperature anisotropies of the CMB radiation to an extremely high precision and small angular resolution. Figure 2.2 shows an example of the CMB temperature map measured by Planck.

The total baryon density Ω_b can be precisely estimated from the angular power spectrum of the CMB radiation[1]. The angular power spectrum shows how large the temperature fluctuations are from point to point on the sky as a function of the angular scale. A combination of data from satellite and balloon-borne and ground-based experiments is usually required for a complete measurement of the CMB power spectrum across a large range of angular scales. An example of the CMB power spectrum is shown in Figure 2.3.

This plot can reveal much about the distribution of matter (both baryons and dark matter) in the early universe. Shortly after the Big Bang, the universe was very hot and highly ionised, and the photon pressure was high enough to prevent baryons from clustering. As a result, any density perturbation did not grow, but instead oscillated in potential wells created by the interplay between the gravitational attraction and photon pressure. These adiabatic density fluctuations can be well modelled as a driven oscillator with a restoring pressure, which gives rise to standing waves. Since these waves travel through a dense medium, they are commonly referred to as "baryon acoustic oscillations" (BAO).

These standing waves remained active until the time when the CMB radiation was released. The fundamental mode and the first overtones of these standing waves appear in the CMB power spectrum as "acoustic peaks" (see Figure 2.3). Strong constraints can be set on some cosmological parameters from these peaks. For instance, the ratio of heights between the even

[1] Ω_i is the density of species i relative to the critical density ρ_c, which is the mean density required for a spatially flat universe.

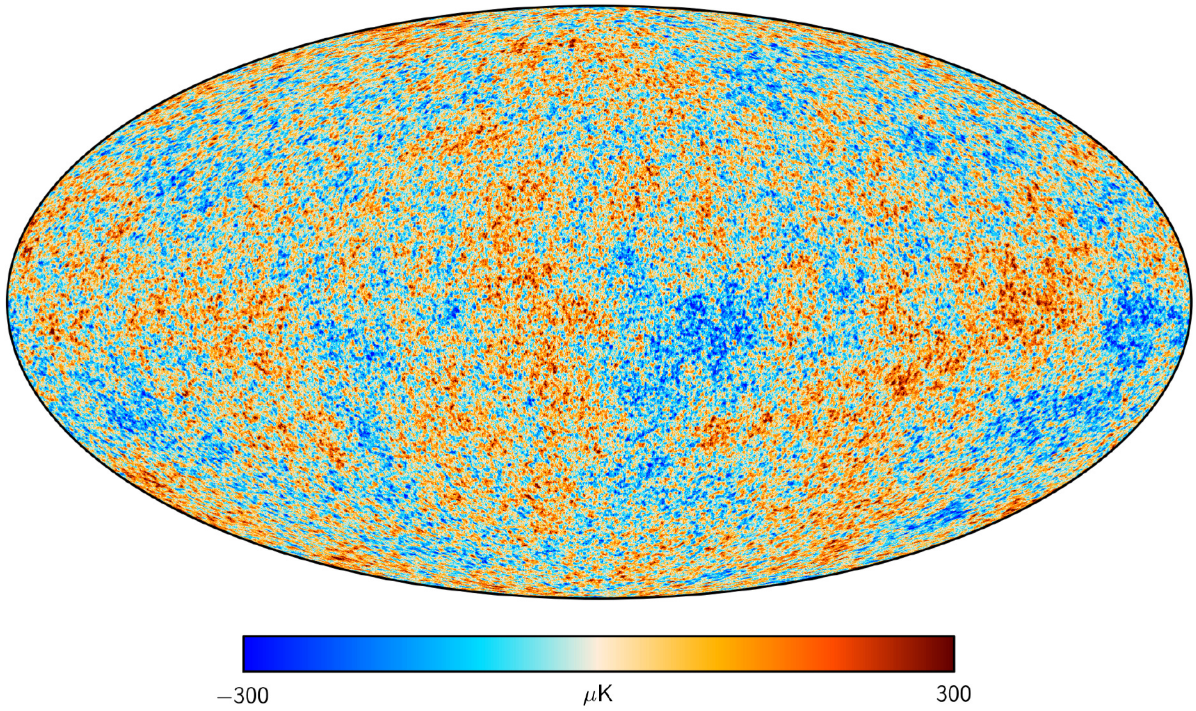

Figure 2.2: All-sky map of temperature fluctuations of the CMB radiation measured by the Planck satellite. This map shows differences in temperature of 0.0006 K from the coldest (blue) to the hottest (red) regions in the sky. Figure: ESA and the Planck Collaboration.

and odd peaks is sensitive to the total baryon density, Ω_b; inertia in the fluid caused by the baryons enhances the odd peaks (compression) with respect to the even ones (rarefaction). The most recent results from the Planck collaboration constrains the baryon density to [28]

$$\Omega_b h^2 = 0.02237 \pm 0.00015, \tag{2.1}$$

which has an uncertainty of less than 1%. Here h is the reduced Hubble constant, which has an estimated value of 0.67 [28].

Moreover, cosmological parameters can also be constrained from a global fit to the CMB power spectrum using the standard model of cosmology: the ΛCDM model. This model, which has been incredibly successful at explaining the wealth of currently available cosmological data, postulates that the universe is mainly composed of two fluids: one accelerating the expansion of the universe (dark energy), and the other acting much like ordinary matter to slow it down (dark matter). The present thesis is focused on the latter component, while good reviews on the former can be found elsewhere (see for instance Ref. [29]). A global fit of this kind is shown in Figure 2.3, where a good agreement between the model (in green) and the experimental data (in red) is observed across across all the angular scales except the largest ones, which are subject

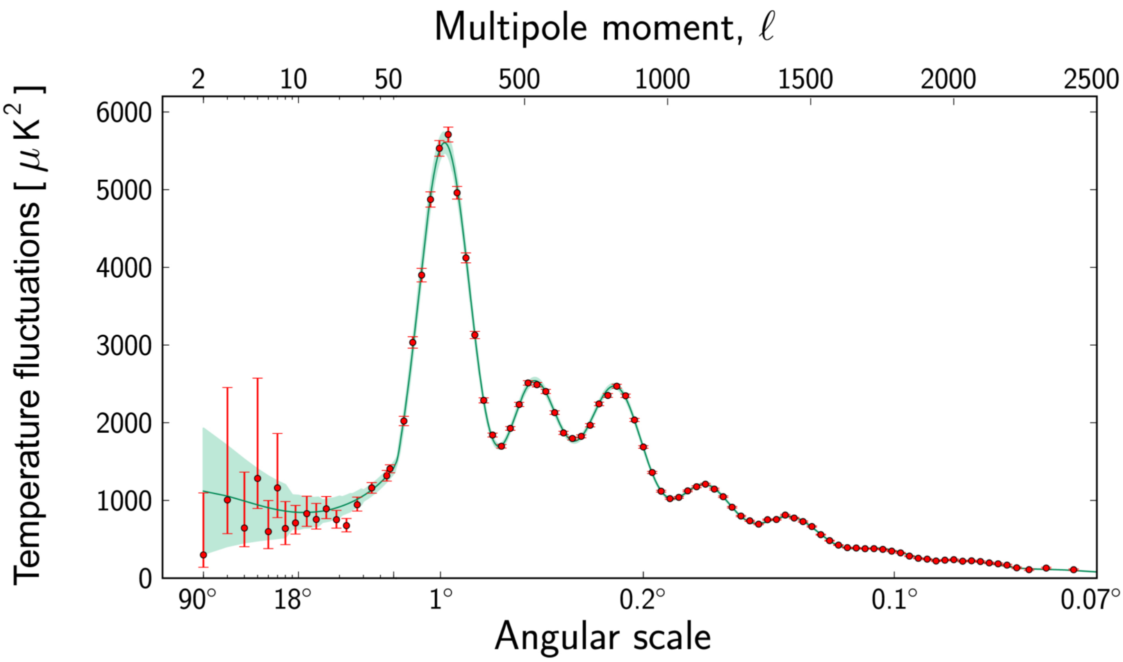

Figure 2.3: Angular power spectrum of the CMB radiation measured by the Planck satellite and several balloon-borne and ground-based experiments. This figure shows the temperature fluctuations in the CMB at different angular scales on the sky, which can be represented in angular degrees (lower horizontal axis) or with the multipole moment l (upper horizontal axis). Data are shown with red dots, whereas the green curve shows the best fit to data of the ΛCDM models. The agreement between data and model is excellent on small and intermediate angular scales, allowing for a precise determination of cosmological parameters. Figure: ESA and the Planck Collaboration.

to a higher uncertainty. From such fit to the CMB power spectrum, the Planck collaboration has constrained the total matter and dark energy abundances, respectively, to [28]

$$\Omega_{\rm m} = 0.3153 \pm 0.0073 \tag{2.2a}$$

$$\Omega_{\Lambda} = 0.6847 \pm 0.0073 \tag{2.2b}$$

Comparing the value of the total matter density, $\Omega_{\rm m}$, to the prediction of the total baryon density, $\Omega_{\rm b}$ in (2.1), one arrives to the striking conclusion that baryonic matter accounts for less than one fifth of the total matter content of the universe. Dark matter makes up the rest.

Furthermore, the total baryon abundance can be estimated independently from Big Bang nucleosynthesis (BBN). BBN refers to the process that took place just minutes after the Big Bang when the lightest elements were created, such as deuterium (D), ^{3}He, ^{4}He and ^{7}Li. The predicted light element abundances are finely tuned to the baryon-to-photon ratio η, since a larger value of η would trigger an earlier start of BBN and enhance the light nuclear production. Deuterium is the main starting building block and most nuclear reactions end with the creation of ^{4}He, because of the unusually large binding energy of helium and the absence of stable nuclei with atomic number $A = 5$ [30]. The theoretical predictions of the nuclear abundance of several light elements as a function of η and the baryon density are shown in Figure 2.4.

The D/H ratio is the most sensitive to changes in η and provides the best constraint on this parameter from all the light element abundances [31]. Alternatively, the baryon-to-photon ratio is well constrained by the CMB as well [28]. Using a baryon-to-photon ratio of $\eta = (5.921 \pm 0.051) \times 10^{-10}$, the current best constraint on the total baryon density from BBN is [32]

$$\Omega_b h^2 = 0.02235 \pm 0.00016 \pm 0.00033, \tag{2.3}$$

where the first uncertainty comes from the measurement of the D/H ratio and the second term refers to the theoretical uncertainty from BBN calculations. This result is in excellent agreement with the CMB result shown in (2.1).

The advent of powerful computing in the late 20th century brought about the development of *cosmological simulations* to study the evolution of structure in the universe. In addition, the publication of the first large scale 3D survey of galaxies, the CfA Redshift Survey in 1982, provided an invaluable source of data with which to compare the results of numerical simulations [33]. Alongside these advances, the hypothesis that dark matter could be composed of one, or more, new particle species started to grow strongly within the scientific community.

Cosmological simulations are excellent testing grounds for different dark matter models. For the purpose of studying structure formation in the universe the actual composition of dark matter is irrelevant, since it simply acts as a massive but practically "collisionless" component. However, its initial velocity distribution is crucial. In this respect, dark matter can be broadly divided into two categories: cold dark matter (CDM) in which particles move slowly at the epoch when they decouple from radiation, and hot dark matter (HDM) in which particles move at relativistic velocities at the time of decoupling. It quickly became clear that the CDM model reproduced much better the observed distribution of matter from galaxy surveys [34, 35], and the HDM model was abandoned.

Moreover, it was suggested that there could be a link between the large scale structure (LSS) in the universe—that is, the distribution of galaxies forming clusters, filaments and voids—and the small density fluctuations that are imprinted onto the CMB. However, as we saw earlier the anisotropies observed in the CMB are vanishingly small (of the order of 10^{-5}), and they cannot grow quickly enough during the age of the universe to match the currently

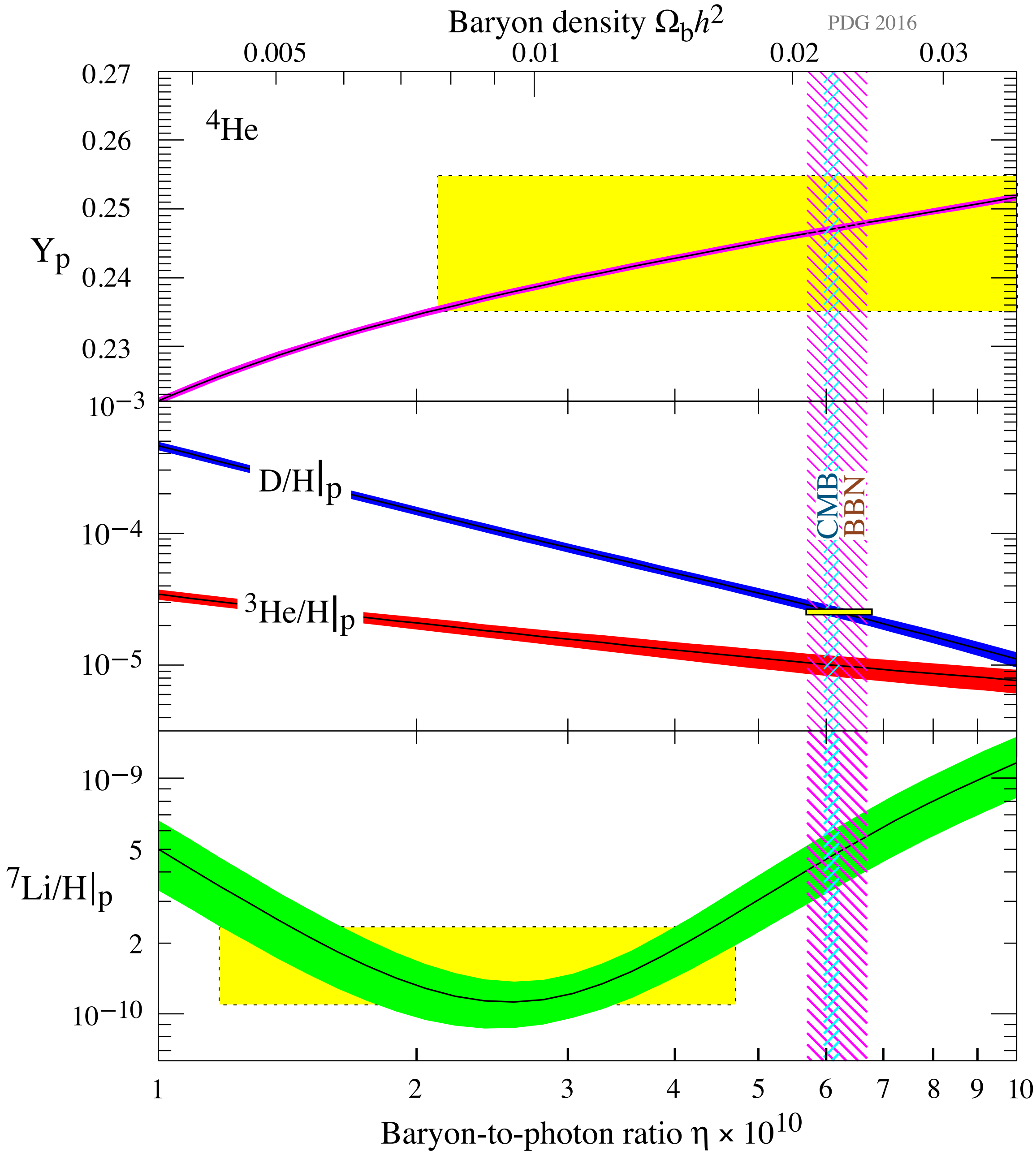

Figure 2.4: The primordial abundances of light elements D, ^{3}He, ^{4}He and ^{7}Li predicted by the BBN model as a function of the baryon-to-photon ratio η. All the abundances are normalised to the hydrogen abundance H. The higher the value of η, the earlier deuterium production starts and the larger the ^{4}He yield (Y_p) becomes. The narrow vertical bands indicate the CMB measure of the baryon density $\Omega_\mathrm{b}h^2$ (cyan) and the BBN estimate of η (magenta) at 95% CL. The observed light element abundances are indicated with yellow boxes. Figure from Ref. [30].

observed LSS. However, if a non-baryonic CDM component were introduced, its density fluctuations could start growing earlier than baryonic matter because they are not coupled to photons, and they could provide the required amplitude at the epoch of recombination without affecting the CMB radiation [7]. In this regard, the CDM model gives an even more fundamental role to the dark matter: to provide the required seeds in the early universe so that baryonic matter can coalesce into the currently observed large scale structure. More recent cosmological simulations, including the Millenium Simulation [36] and the Illustris Project [37], have confirmed the validity of the CDM model.

In conclusion, all the apparently disconnected observations that have been highlighted in this section, from galactic to cosmological scales, could be explained if one assumes that a dominant fraction of the mass content in the universe is composed of essentially collisionless, cold and non-baryonic particles.

2.2 Particle landscape

Despite the body of evidence presented in the previous section, little is known about the nature of dark matter. A particle interpretation seems plausible and it is supported by the CMB measurements, while modifications to Newton's law of gravitation fail to explain some of the evidence. In this section we give a summary of the main properties of dark matter that have been inferred via their interaction with baryonic matter, and we introduce some of the currently most favoured particle candidates.

Firstly, dark matter is *non-baryonic*, as deduced from the CMB power spectrum and gravitational lensing observations, amongst other evidence; on the other hand, BBN accounts for all the baryons of the universe independently. It is important to mention that "dark baryonic objects", collectively known as Massive Compact Halo Objects (MACHO), indeed exist. However, their predicted abundance is too low to account for all the dark matter in the universe. For instance, the EROS-2 collaboration has constrained the contribution of MACHOs in the Milky Way to only a small fraction of the total galactic mass from a survey of 7 million stars [38].

Alternatively, it could be argued that dark matter is composed of black holes that were formed before the epoch of BBN. This idea was originally proposed by Carr and Hawking in 1974 [39], and has been actively developed since then. Although the possibility of such "primordial black holes" (PBH) making up a fraction of the total dark matter abundance remains open, stringent constraints have been placed on their mass range [40].

Secondly, dark matter is *electrically neutral*, since it neither absorbs nor emits light. It is *not strongly interacting*, or otherwise abnormally heavy isotopes could be formed, which have not been observed experimentally. Moreover, it should be *stable*, or very long-lived, to account for the fact that its effects have been noted throughout the entire history of the universe. Not only that, but any particle candidate of dark matter should be produced in the early universe with the right abundance to match the observed dark matter density.

As already mentioned, models of "hot dark matter" reproduce poorly the large scale structure observed in the universe. By contrast, *cold dark matter* is better motivated from numerical simulations and they are currently part of the standard model of cosmology, i.e. the ΛCDM model. As a result, the mass of current candidates of dark matter thermally produced in the early universe is constrained to be either much larger than keV (cold DM), or of the order of keV ("warm" DM) [34].

Originally, neutrinos were proposed as dark matter candidates, and a substantial amount of theoretical work was developed to understand the cosmological role of this particle [41–43]. Ultimately, neutrinos were ruled out as dark matter candidates for constituting hot DM and not being abundant, or massive, enough [44]. However, this initial research on neutrinos served an even more important role: it provided a template for another type of weakly interacting particle that would become the most extensively studied dark matter candidate, as explained next.

2.2.1 WIMPs

Currently, a favoured hypothesis is that dark matter is composed of weakly interacting massive particles (WIMPs), moving at non-relativistic velocities at the epoch in which they departed from thermal equilibrium, and hence constituting cold dark matter. WIMPs are assumed to be stable, to interact via gravity and any other force that is as weak in strength as the weak nuclear force, and to have a mass in the GeV–TeV range [45].

In the early universe, WIMPs would be in thermal equilibrium with ordinary matter. Such thermal equilibrium is broken when the rate of expansion of the universe becomes larger than the annihilation rate of WIMPs:

$$H(t) \geq n_\chi \langle \sigma_{\mathrm{ann}} v \rangle, \tag{2.4}$$

where $H(t)$ is the Hubble parameter, n_χ is the WIMP number density and $\langle \sigma_{\mathrm{ann}} v \rangle$ is the thermally averaged WIMP annihilation cross section times the relative velocity v. At such point, the WIMP number density "freezes out" and a substantial number of relic particles are introduced. This "relic density" can then be compared to the presently observed dark matter density of $\Omega_{\mathrm{dm}} \approx 0.26$ (see Eq. (2.1) and (2.2a)). For instance, the WIMP relic density can be approximately expressed as follows for s-wave only (velocity-independent) annihilation [46]:

$$\Omega_\chi h^2 \approx \frac{3 \times 10^{-27}\,\mathrm{cm}^3/\mathrm{s}}{\langle \sigma_{\mathrm{ann}} v \rangle} \,. \tag{2.5}$$

According to this expression the WIMP relic density is inversely proportional to the annihilation cross section and it is independent of the WIMP mass. Larger annihilation cross sections lead to a delayed departure from thermal equilibrium, and therefore a smaller relic density. Remarkably enough, in order to get a relic density that matches the current value of Ω_{dm}, one needs to assume an annihilation cross section of the order of magnitude of that expected for weak force interactions. This rather unexpected connection between particle physics and cosmology has been commonly referred to as the "WIMP miracle".

No evidence exists at present that forbids dark matter from interacting via the weak force with ordinary matter, and the WIMP model relies heavily on this assumption. However, and quoting the popular aphorism "absence of evidence is not evidence of absence", we note that this is a strong assumption and it is certainly one of the most disputable points of the WIMP hypothesis. In addition, the WIMP hypothesis does not provide any satisfactory explanation to the fact that the current DM and baryon abundances are comparable to each other (i.e. $\Omega_{\mathrm{dm}} \approx 5\Omega_{\mathrm{b}}$), even though their production mechanisms are very different. The present density of ordinary matter is known to be due to the baryon asymmetry of the universe (BAU). Similarly, asymmetric dark matter (ADM) models have been introduced, in which the present DM density is due to an early DM particle-antiparticle asymmetry. Such asymmetry would be directly linked to the baryon asymmetry by some common process in the early universe, but later decoupled from it (see for instance Refs. [47, 48]).

One of the most favoured WIMP candidates arises from "supersymmetry" (SUSY). Supersymmetry is an extension of the Standard Model (SM) of particle physics that introduces a new global symmetry between fermions and bosons. According to this theory, for each particle there is an associated "superpartner" with the same internal quantum numbers apart from spin, which is different by one half. Hence, every boson has a supersymmetric fermion partner (suffixed with "-ino"), while every fermion has a boson superpartner (prefixed with "s-"). No superparticle has been experimentally observed yet, so it is commonly assumed that SUSY is spontaneously broken and the predicted mass of the superpartners is significantly larger than that of the SM particles to avoid detection.

One of the successes of the theory is its ability to solve the hierarchy problem in the Standard Model. Without SUSY, the quadratically divergent loop corrections that appear in the renormalization of the Higgs mass have to be finely tuned to yield the relatively small and finite value of 125 $\mathrm{GeV/c^2}$, which has been experimentally measured at the LHC [49, 50]. Supersymmetric particles have loop corrections with the opposite sign to the ones provided by the Standard Model particles, and as a result, SUSY provides a cancellation mechanism that avoids the fine-tuning.

SUSY particles are expected to be created in pairs, with opposite values of a new global symmetry called R-parity:

$$R = (-1)^{L+3B+2S}, \tag{2.6}$$

where L is the lepton number, B the baryon number and S is the spin. Within this framework, Standard Model particles have $R = +1$, while supersymmetric partners have $R = -1$. In most supersymmetric models R-parity is conserved. This conservation law controls the decay process of heavier SUSY particles into lighter ones, ultimately ending up with the lightest supersymmetric particle (LSP), which cannot decay any further. The LSP is therefore stable, neutral and weakly interacting, making it an excellent WIMP candidate. Under minimal supersymmetric extensions of the Standard Model (MSSM), the LSP is identified with the neutralino, which arises from a linear combination of a wino, a bino, and two higgsinos [46].

Therefore, SUSY is able to solve some of the outstanding problems of the Standard Model of particle physics at the same time that it provides a good particle candidate for dark matter, which explains the great attention that this theory has received since its conception. However, a large part of the allowed parameter space for the most straightforward MSSM models has already been ruled out experimentally—mostly by the combination of searches at the LHC and direct searches with underground experiments [51, 52]. Other models with a larger number of free parameters exist, such as the phenomenological MSSM (pMSSM), but this raises the question of how much fine-tuning one is willing to accept before ruling out SUSY entirely [53].

Apart from supersymmetry, it should be emphasised that there are also valid WIMP dark matter candidates arising from other theories. Ideas range from models with Universal Extra Dimensions (UED) [54] to non-thermal dark matter of huge masses, the so-called “WIMPzillas” [55]. Underground experiments such as LUX-ZEPLIN (LZ) will be searching for WIMP dark matter. Working alongside the LHC, these experiments will cover the parameter space favoured by various SUSY models, but they are in fact more general and will be able to test other models predicting dark matter scatters from ordinary matter too [1].

2.2.2 Axions

Axions were originally postulated to provide a solution to one of the outstanding problems of the Standard Model of particle physics, as explained next. The current theory of Quantum Chromodynamics (QCD) predicts a non-negligible electric dipole moment of the neutron (nEDM) as a direct manifestation of the violation of the strong CP symmetry, which is not a conserved quantity in the theory. However, the neutron electric dipole moment has been experimentally measured to be vanishingly small, which suggests an unnatural conservation of the strong CP symmetry [56]. This puzzling observation is usually referred to as the "strong CP problem". It has been argued that this is unlikely to be a fortuitous coincidence, and it could instead be a demonstration of new physics beyond the Standard Model [57].

In 1977, Peccei and Quinn proposed a solution to this problem. Their suggestion was to introduce a new hidden and spontaneously broken global symmetry, the "PQ symmetry", which would make the QCD Lagrangian CP-conserving [58, 59]. The PQ symmetry would spontaneously break at an energy scale f_a, and via this mechanism a massive pseudo-Goldstone boson would be generated [60, 61]. This particle became known as the "axion", named after a laundry detergent [62]. The mass of the axion is predicted to be inversely proportional to the symmetry breaking scale f_a [58], specifically

$$m_a \simeq (0.6\ \mathrm{eV})\frac{10^7\ \mathrm{GeV}}{f_a}\ . \tag{2.7}$$

Although f_a is a free parameter of the theory, it is constrained to be much larger than the electroweak symmetry-breaking scale to accommodate existing experimental bounds [63], making axions very light particles.

Several production mechanisms have been proposed since the axion was conceived. Although thermal production in the early universe is possible for axions, they would contribute to the cosmic hot dark matter and strong constraints have been placed on the predicted mass of thermal axions [64]. However, other mechanisms have been proposed that could generate non-relativistic axions, such as the "re-alignment mechanism" [65, 66]. This makes axions a valid cold dark matter candidate despite their predicted low mass. Currently, the dark matter window in which axions could still account for the dark matter in the universe is constrained to the region $10^{-6} \lesssim m_a \lesssim 10^{-3}\ \mathrm{eV}/c^2$ [67]. Also, and unlike fermionic dark matter (e.g. WIMPs), axions can share a single quantum state and form a Bose-Einstein condensate, which could plausibly explain the dark matter problem if their number density is large enough.

Although axions are expected to have such low mass and even smaller interaction cross sections with ordinary matter than WIMPs, they could potentially be detected via their coupling to photons [68]. This leads to photon-axion oscillations in the presence of a strong magnetic field, a process known as the Primakoff effect, which opens a window for its detection. Moreover, "axion-like particles" (ALP) have been proposed, which share some of the axion phenomenology, like the coupling to photons and its predicted low mass, but do not hold such a direct link with the PQ symmetry. In these models, the ALP mass and its coupling to photons are both free parameters, enlarging the available parameter space compared to the original QCD axions. Recent axion and ALP searches include:

- **Axion haloscope**: they look for galactic axions via their resonant conversion into a microwave signal in a high-Q electromagnetic cavity embedded in a strong magnetic field. The cavity frequency is tunable, and it can be gradually adjusted to test a narrow range of axion masses with very high sensitivity. The leading experiment with the currently lowest sensitivity is ADMX [69].

- **Axion helioscope**: axions might be generated inside the Sun, and they could be detected at Earth as X-rays after triggering an $a \to \gamma$ conversion in the presence of a strong magnetic field. This type of searches allows for the exploration of a vast range of axion masses, but their sensitivity to axion couplings is not as good as haloscopes. In this category we find CAST, which used a decommissioned LHC magnet of 9 T and recently concluded operations [70]. The upgraded project IAXO is currently under way.

- **Light shinning through walls**: in these searches, a laser beam is propagated between the bore of two superconducting magnets separated by an optical barrier. The initial photon beam is expected to be transformed into an axion beam and then converted back into photons, producing a light signal through the opaque wall. This is the least sensitive approach, but it is not affected by the cosmological or astrophysical uncertainties of the previous two. Experiments such as OSQAR [71] and ALPS [72] have placed limits on axion couplings based on this concept.

- **Direct detection**: underground direct detection experiments can also search for axions via the axio-electric effect, in which an axion is absorbed and an atomic electron is ejected. The outgoing electron can be detected as an electron recoil, and this signal could be identified from its characteristic energy spectrum in a noble gas TPC. An analysis of this type from LUX has constrained the axion-electron coupling constant to $g_{ae} < 3.5 \times 10^{-12}$ for massless solar axions and to $g_{ae} < 4.2 \times 10^{-13}$ for ALPs in the mass range 1–16 keV/c^2 [73].

- **Astrophysical probes**: the solar photon luminosity or the luminosity of stars on the Horizontal Branch (HB) are fixed quantities. Hence, and assuming that these stars are affected by photon losses from Primakoff-like axion emission, it is possible to set constraints on the axion-photon coupling from such astrophysical measurements [74, 75]. In addition, constraints on the axion-electron coupling can be derived from other astrophysical sources, such as red giants and white dwarfs, assuming that axions couple directly to electrons [76, 77]. Similarly, energy-loss effects can also be searched for in supernova explosions or in the gamma-ray spectrum of distant active galactic nuclei (AGN) [78–80].

2.2.3 Sterile neutrinos

In the early 1990s, Dodelson and Widrow proposed another candidate for dark matter: an additional neutrino species that only interacts gravitationally with matter [81]. Although these neutrinos would not interact via the weak nuclear force, they would interact "feebly" with ordinary matter via oscillations with Standard Model neutrinos. To distinguish them from the "active" SM neutrinos, they received the name of "sterile neutrinos".

The expected interaction rate of such particle with ordinary matter is so small that they would never reach thermal equilibrium in the early universe. Nevertheless, a few production mechanisms have been suggested in which the sterile neutrino could still achieve the observed dark matter abundance [82]. Depending on their assumed mass, these sterile neutrinos can either constitute warm ($m_{\nu_s} \sim$ keV) or cold ($m_{\nu_s} \gg$ keV) dark matter.

The detection of an unidentified 3.55 keV line from the stacked X-ray spectra of several dark matter-dominated galactic clusters has given rise to a great deal of interest [83]. This could potentially be interpreted as the decay signature of keV-scale dark matter, favouring the sterile neutrino as dark matter candidate. However, the discussion is still open, and other authors have explicitly ruled out a DM interpretation [84, 85].

2.3 WIMP detection

We have mentioned above some of the leading candidates for particle dark matter, and several dozen more exist with varying levels of theoretical motivation. Such richness in phenomenology is translated into a broad range of possible experimental searches for dark matter. In this section we focus on WIMP searches, but it is important to highlight that the current scope of dark matter searches is indeed vast (see e.g. Ref. [86] for a recent synopsis).

At present, WIMP searches can be classified as follows:

- **Direct detection:** they search for the scattering signal between galactic dark matter and a target made of ordinary matter. This requires ultra-low background detectors with low energy thresholds, operating deep underground or inside a mountain.

- **Indirect detection:** they look for the reaction products of dark matter annihilations, such as gamma rays, neutrinos, positrons, or antiprotons. Astronomical objects with an expected large accumulation of dark matter are prime targets for these experiments, including dwarf spheroidal galaxies orbiting around the Milky Way, the Milky Way's galactic centre, the Sun's core or even the centre of the Earth.

- **Particle colliders:** they aim at producing dark matter particles from the energy released in particle collisions. One common signature in this type of searches is missing momentum in the plane perpendicular to the collision, as dark matter particles are expected to leave the collider undetected. At present, the Large Hadron Collider (LHC) is the highest energy particle collider in operation.

Despite their differences, these approaches are complementary to each other and they allow for a more extensive exploration of the WIMP parameter space [87].

2.3.1 Direct searches

The scattering of WIMPs off atomic nuclei would result in nuclear recoils. Note that this scattering could be either elastic or inelastic, where the latter type relates to nuclear excitations in the target [88, 89] or excited dark matter states [90–92]. The corresponding recoil energy spectrum depends on the assumed properties of the WIMP particle and the atomic target, but in general most nuclear recoils will have an energy below $\sim 100\,\mathrm{keV}$ [93]. Starting from some basic assumptions, one can estimate that the expected scattering rate for a WIMP mass of $100\,\mathrm{GeV/c^2}$ moving with a mean velocity relative to the target of $220\,\mathrm{km/s}$ is $\lesssim 1$ event/kg/year [94]. Direct detection searches try to overcome the difficulty of detecting a signal of such an extraordinarily small rate by employing detectors with an ultra-low background level and installed underground or inside a mountain to decrease the cosmic ray background. Moreover, a low energy threshold and a target mass as large as possible are desirable features.

Direct detection WIMP searches are mainly focused on detecting nuclear recoils (NR) created in DM-nucleon interactions, and they generally treat electron recoils (ER) as background. However, it should be noted that searches for DM-electron interactions also exist [86]. Focusing on elastic scattering, the kinetic energy imparted to the nucleus can manifest itself in three different channels: atomic motion (heat), excitation or ionisation. Most importantly, electron and nuclear recoils distribute their energy deposition differently between these channels [95]—an effect that can potentially be exploited to reject electron recoils efficiently. Different technologies exist to search for these tiny energy depositions, which are usually sensitive to either one or a combination of two of the above channels [96].

The most recent experimental exclusion limits on the spin-independent (SI) WIMP-nucleon cross section from direct dark matter searches are shown in Figure 2.5. Next, we give a brief account of the different technologies employed by the experiments shown in this figure and their future outlook.

Experiments using *liquid xenon (LXe) time projection chambers (TPC)* have been leading the SI WIMP search over the past decade. The success of liquid xenon detectors is explained by several factors: an expected higher WIMP-nucleus interaction cross section due to the A^2 enhancement in the SI channel (as explained in Section 3.1.2), the absence of long-lived radioisotopes in natural xenon, a low detection threshold, the ability to precisely reconstruct the full event position, an excellent ER discrimination achieved through the combined detection of scintillation and ionisation signals, and the procurement of a highly radiopure target and detector components.

Currently, the most stringent constraints on the SI WIMP-nucleon scattering cross section above $5\,\mathrm{GeV/c^2}$ are set by experiments such as LUX, PandaX-II and XENON1T, which have excluded cross sections below $10^{-46}\,\mathrm{cm^2}$ at their peak sensitivity. The LUX experiment was located at the Sanford Underground Research Facility (SURF) at the Homestake mine in the US, and it operated a dual-phase (liquid and gas) LXe TPC with 250 kg of active mass [97]. LUX has already been decommissioned, and the same infrastructure is being used to install the LZ experiment, which will contain 7 tonnes of active liquid xenon [1]. By contrast, the XENON Collaboration has hosted all their subsequent detectors at the Laboratory Nazionali del Gran Sasso (LNGS), in Italy. The laboratory is situated below the Gran Sasso mountain, which makes its access more convenient compared to underground laboratories. XENON1T acquired data from 2016 until 2018, and published the first results with a tonne scale target [98]. They are currently upgrading the experiment for the XENONnT phase [99]. Finally, the PandaX-II experiment is located at the China Jinping Underground Laboratory (CJPL), and it operates a half-tonne scale dual-phase LXe TPC [100]. Plans for a future upgrade to a multi-tonne scale experiment are being considered.

Conversely, there has been a moderate progress from experiments using *liquid argon (LAr) TPCs*. Liquid argon detectors benefit from a lower cost of the target material (compared to e.g. xenon), a comparably easier purification procedure of contaminants, and a higher

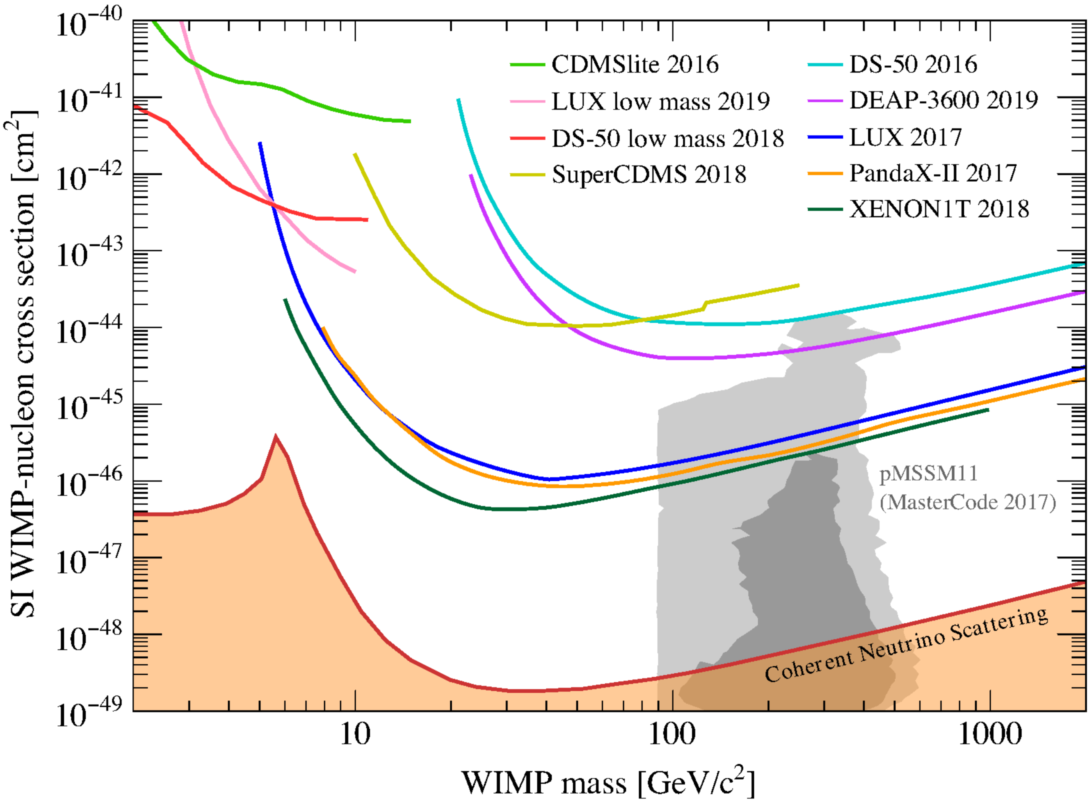

Figure 2.5: Exclusion limits on the spin-independent WIMP-nucleon cross section as a function of WIMP mass from some of the leading direct detection experiments. We find experiments employing cryogenic crystals on the top left corner (CDMSlite [101], SuperCDMS Soudan [102]), as well as low mass analyses from noble liquid detectors (DarkSide-50 [103], LUX [104]). On the top right corner we find results from liquid argon TPCs (DarkSide-50 [105], DEAP-3600 [106]), while those from liquid xenon TPCs are shown in the centre (LUX [97], PandaX-II [100], XENON1T [98]). The 1σ and 2σ favoured contours from a recent global fit scan based on a pMSSM model are shown in grey [107]. Also, the "neutrino floor" is indicated by the light brown shaded region [108] (see Section 2.3.1).

ER discrimination capability (due to the large difference between the decay times of the two scintillation components in the de-excitation of argon dimers [109]). However, natural atmospheric argon contains an intrinsic radioisotope, ^{39}Ar, which can be challenging to mitigate. Using underground argon with a low level of ^{39}Ar can alleviate the problem [110], but it inevitably increases the cost of the project. Also, liquid argon detectors usually have to define higher energy thresholds than liquid xenon detectors since their ability to discriminate ER interactions via pulse shape discrimination (PSD) only becomes feasible for large enough energy depositions.

Currently, DEAP-3600 is the only running experiment using a single-phase (liquid) argon TPC. Located at SNOLAB in Canada, their current system features 3.6 tonnes of liquid argon and it has been operating since November of 2016. A recent result from the DEAP-3600 collaboration after 231 live days of data has demonstrated the best pulse shape discrimination in LAr to date [106]. Unfortunately, the resulting exclusion limit on the SI WIMP-nucleon cross section, shown in purple in Figure 2.5, has been lower than their predicted sensitivity due to an unexpected large background coming from the neck of the detector. By contrast, experiments such as ArDM [111] and DarkSide-50 [105] employ a dual-phase argon TPC. They are located at the Canfranc Underground Laboratory in Spain and at LNGS in Italy, respectively. DarkSide-50 has has operated a TPC with a 50 kg active mass of liquid argon since 2013, and the collaboration is planning to upgrade its detector to a 20 tonne TPC by 2022 [112].

The low WIMP mass region is accessible by detectors with a very low energy threshold and/or lighter target nuclei (than e.g. xenon or argon). A sub-keV energy threshold can be achieved, for instance, by employing *cryogenic solid-state detectors* coupled to phonon sensors. An energy deposit in these detectors produces a measurable population of athermal phonons. This signal can be combined with a ionisation or scintillation read-out channel to discriminate ER from NR interactions on an event-by-event basis.

These detectors have been extensively improved by the CDMS collaboration, which uses both germanium and silicon targets. Different versions of the CDMS experiment have operated between 1998 and 2015 at Stanford Underground Facility (California, USA), and Soudan Underground Laboratory (Minnesota, USA). The newer generation of experiments will be moved to SNOLAB, in Canada, and the construction is expected to be completed by early 2020. The current best exclusion limits set by SuperCDMS Soudan, using data from cryogenic germanium detectors, are shown in Figure 2.5. The yellow line shows the result using nominal operation conditions [102], while the green line is the result of a special “run” at an increased electric field (CDMSlite) [101].

In addition, the European group EDELWEISS [113] and CRESST [114] have further developed this technology, using germanium and calcium tungstate crystals, respectively. It has long been a goal of these collaborations to build a tonne-scale cryogenic dark matter detector, and the feasibility of a joint project such as EURECA is being explored [94].

Another possible avenue in the direct search for dark matter is to look for an *annual modulation* in the recoil scattering rate. This idea was first introduced by Drukier, Freese and Spergel, who suggested that the combined effect of the Earth's motion around the Sun and the Sun's motion across the dark matter halo could create such annual modulation [115]. In 1998, the DAMA/NaI experiment reported the observation of an annual modulation rate that was consistent with a dark matter interpretation [116], and this result became persistently more statistically significant over the following two decades with new data from the upgraded DAMA/LIBRA detector [117–119]. However, these results are incompatible with the null observation from the vast majority of other direct detection experiments. New experiments have appeared in recent years, such as COSINE-100 [120] or SABRE [121], that aim to resolve the conundrum by conducting an independent test using the same detector materials as DAMA.

Alternatively, it is also possible to explore the low WIMP mass region by developing new analysis techniques, which can lower the energy threshold at the expense of increasing the background rate and therefore sacrificing some sensitivity. On the one hand, this can be achieved in LXe and LAr TPC experiments that have sensitivity to both scintillation and ionisation signal by exclusively using the ionisation signal to determine the recoil energy [122, 103]. Dropping the scintillation signal affects the ability of the experiment to discriminate between electron and nuclear recoils effectively, as well as losing some position information, but takes advantage of the intrinsically larger gain of the ionisation channel. In such cases, it is possible to lower the energy threshold, and lighter dark matter particles of up to 1 $\mathrm{GeV/c^2}$ become accessible. On the other hand, it has been demonstrated that the standard WIMP search in LXe detectors can be extended to single scintillation photons by exploiting the "double photoelectron emission" observed in some photomultiplier models, in which two photoelectrons are detected for one single incident photon [123, 104]. The most constraining upper limits at present based on these novel analysis techniques are shown in Figure 2.5 (red and pink lines, respectively). In addition, new detectors using lighter targets such as superfluid helium are being developed to continue the push down to sub-GeV dark matter [124].

Direct detection searches of WIMPs might ultimately be limited by an irreducible background coming from coherent elastic neutrino-nucleus scatters [125]. Neutrino-induced nuclear recoils from ^{8}B solar neutrinos can mimic a WIMP signal for masses around 5–6 $\mathrm{GeV/c^2}$, whereas atmospheric and diffuse supernova neutrinos can mimic a heavier WIMP signal

[126, 108]. The systematic uncertainty introduced by these neutrino fluxes creates a WIMP discovery limit, also known as the "neutrino floor", below which current direct detection searches become insensitive to dark matter signals. The neutrino floor for SI scattering is shown in Figure 2.5 as the light brown shaded region. Although such limit could potentially be mitigated with an improved understanding of the neutrino fluxes or the development of new technologies with directional sensitivity [127], coherent neutrino-nucleus scatters will undoubtedly become an important background source to take into account by upcoming direct detection dark matter experiments.

2.3.2 Indirect searches

Indirect dark matter detection aims at observing WIMP annihilation products arising in the Milky Way or elsewhere. Intuitively, it is expected that the flux of annihilation products will be higher in those regions where there is a larger concentration of dark matter. Hence, those astronomical sources with a possibly enhanced dark matter concentration have been the prime targets for these searches, such as dwarf spheroidal Milky Way satellites, the Milky Way's galactic centre and halo, or galactic clusters [128].

The calculation of the annihilation particle flux from the astrophysical source to the measuring instrument depends heavily on the assumptions made about the particle dark matter model and the astrophysical input, such as the dark matter distribution or the galactic diffuse model of charged particles. In addition, all the possible backgrounds to a potential dark matter signal must be clearly established, and this can be a challenging task. As a result, large model uncertainties are usually associated with any interpretation of a radiation excess in heavily populated dark matter regions, making trustworthy discovery claims very difficult.

One type of dark matter annihilation products that have attracted a great deal of interest are *gamma-rays*. Mainly, the appeal for these cosmic messengers comes from the fact that they do not scatter appreciably, making it possible to point back to the emitting source. In addition, they have a negligible absorption probability, which enables the possibility of making inferences about the astrophysical process that created them from the observed energy spectrum. Current experimental gamma-ray searches can be divided into two types: satellites (e.g. Fermi spacecraft), and ground-based Cherenkov telescopes (e.g. VERITAS, HESS and MAGIC) [129].

An excess of gamma-rays in the Fermi data around the Milky Way's galactic centre, peaking around 2–3 GeV, has attracted a great deal of interest. Despite early attempts to interpret this observation as a dark matter signal [130–132], evidence that the excess is due to unresolved point sources, such as millisecond pulsars, is strengthening [133, 134]. Future experiments, such as the Square Kilometre Array (SKA) [135], or the Cherenkov Telescope Array (CTA) [136] should be able to shed light on the origin of this signal. In addition, the Fermi-LAT collaboration has reported no excess of gamma-rays in a combined analysis of 15 dwarf spheroidal satellite galaxies orbiting around the Milky Way. This observation, or rather the lack of an observation, represents the strongest limit on the dark matter annihilation cross section to date, constraining $\langle\sigma_{\text{ann}}v_0\rangle < 3\times10^{-26}\,\text{cm}^3/\text{s}$[2] for a DM mass below $100\,\text{GeV}/\text{c}^2$ in the bottom quark and τ-lepton annihilation channels [137].

Other relevant annihilation products are cosmic rays such as *positrons and antiprotons*. Under most dark matter models, equal amounts of matter and anti-matter are created in any dark matter annihilation. Consequently, the detection of an excess of anti-particles of unknown astrophysical origin would be a clear observation of dark matter annihilations.

This possibility has been extensively discussed as a raise of the positron fraction in the Milky Way up to hundreds of GeV was clearly observed by the PAMELA experiment in 2008 [138], and later confirmed by Fermi-LAT and AMS-02 [139, 140]. However, the required annihilation cross sections to explain the position excess in terms of dark matter are incompatible with constraints provided by other dark matter experiments [141]. Alternatively, models based on the idea of positron emission from nearby pulsars have also been suggested [142]. A new generation of satellite-borne instruments with sensitivity to an extended energy range, such as NUCLEON, CALET and DAMPE, might provide further guidance regarding the origin of the positron anomaly.

Next, other possible annihilation products are *neutrinos*. They can easily escape from the astrophysical source in which they were generated, and travel over long distances without being perturbed, which makes them an ideal “cosmic messenger”. On Earth they are detected by neutrino telescopes, with IceCube currently in operation in the South Pole [143] and KM3NeT in construction in the Mediterranean Sea [144], which will replace ANTARES [145]. In their search for astrophysical sources, the most characteristic signature is the detection of “tracks” from upward-moving particles, which unambiguously indicate an interaction from a neutrino that has crossed the Earth without being absorbed.

Alternatively, neutrino telescopes are also sensitive to dark matter self-annihilation reactions. It is expected that dark matter particles in our galaxy will occasionally scatter with nuclei and lose enough momentum to become gravitationally bound to a celestial body, such as the Sun or the Earth. In the case of the Sun, a large enough density of DM particles may have accumulated in its core over the lifetime of the star such that an equilibrium between the

[2] The symbol v_0 is used to indicate that this limit is on the velocity-independent annihilation cross section.

capture rate and the annihilation rate of dark matter is established. Under this assumption, the only relevant astrophysical parameter for this type of search is the local dark matter density, which represents an advantage compared to other searches where an accurate description of the distribution of dark matter in the galaxy is needed. The neutrinos produced in such dark matter annihilations, or via the subsequent decay of other annihilation products, are expected to be highly energetic ($E_\nu > 10\,\mathrm{GeV}$). As a result, such neutrinos could be easily distinguished from the low energy neutrinos produced in nuclear reactions inside the Sun ($E_\nu \sim$ MeV). Consequently, the measurement of a high energy neutrino flux coming from the Sun would represent a clear evidence for dark matter [146].

There are several possible annihilation channels. Since the exact couplings between dark matter and ordinary matter are still unknown, it is typical to compare results under a set of benchmark models. In particular, two extreme cases are considered,

$$\begin{aligned} \text{Soft channel: } \chi\chi &\to b\bar{b} \\ \text{Hard channel: } \chi\chi &\to \tau^+\tau^- \end{aligned} \tag{2.8}$$

where χ represents a dark matter particle, and *soft* and *hard* are used in this context to refer to the fact that the average energy of the corresponding neutrinos arriving at the Earth's surface is lower or higher, respectively. In addition, a 100% branching fraction is usually assumed for each of these benchmark channels in order to ignore model dependencies.

Both ANTARES and IceCube have placed constraints on dark matter properties [147, 148]. In particular, they have placed competitive exclusion limits on the spin-dependent WIMP-proton cross section from their solar dark matter searches. This is due to the fact that the majority of the Sun's mass is composed of hydrogen, and therefore their assumed target mass is comparatively larger than those in direct detection experiments.

To conclude this section, it is worth pointing out that the recent discovery of *gravitational waves* by the LIGO and VIRGO collaborations [149] brought about a new observational window on the universe. The prospect of performing "multi-messenger astronomy" has become a reality, in which astronomical objects could be studied using the coordinated observation of up to four extrasolar messengers: electromagnetic radiation, gravitational waves, neutrinos and cosmic rays. There have already been some remarkable breakthroughs, such as the coincident detection of a neutron star merger by both gravitational waves and gamma-ray observatories [19, 20], or the confirmation of a blazar detection by gamma-ray observatories after being alerted by the IceCube neutrino telescope [150]. Apart from its contribution to the study of astronomical objects, multi-messenger astronomy is also expected to provide further insights in the search for dark matter [151].

2.3.3 Collider searches

Dark matter searches can be conducted at particle colliders, such as the LHC, via their direct production in proton-proton collisions: $pp \rightarrow \chi\chi$ (where p stands for proton and χ represents a dark matter particle). Collider experiments alone might not be able to characterise fully the dark matter, but they are best positioned to discover new “invisible particles” that can lead the way in this quest to better understand DM-SM particle interactions . The LHC is expected to collect a large volume of data operating at a center-of-mass energy of 14 TeV in its High-Luminosity run, planned to start in 2026. With such big collection of proton-proton collision data, the LHC will be in a suitable position to search for extremely feebly DM-SM interactions.

One of the main observables for DM searches in colliders is missing momentum in the transverse plane, the magnitude of which is usually represented with the symbol $\not{E}_T$. Searches for invisible particles at the LHC usually involve looking for an excess of $\not{E}_T$ over the SM background. However, measuring $\not{E}_T$ precisely can be very challenging and that is why many collider searches (from LEP to the LHC) have used the following key signature in order to tag relevant events

$$\mathrm{ISR} + \not{E}_T \ , \tag{2.9}$$

where ISR stands for “initial-state radiation”.

Some examples of ISRs used in recent searches of this type from ATLAS and CMS include: gluon jets, photon and Z bosons, Higgs boson, and third-generation quarks (i.e. top and bottom) [152]. Minimal assumptions about the visible objects are usually made to be as model agnostic as possible. Conversely, if one attempts to set constraints on a complete theory with many free parameters that provides some valid candidate for dark matter, such as SUSY, then the set of potential experimental signatures grows drastically. In order to mitigate this, SUSY searches for dark matter generally target specific decay topologies, applying as a result even stricter event selection cuts. In addition, dark matter interactions can be probed without having to assume to production of invisible particles. This is the case of dijet resonance searches for instance, where the signature is a mediator particle decaying into quarks.

So far none of the dark matter searches at the LHC have reported the discovery of any positive signal. Comparisons of results between the ATLAS and CMS experiments, and between non-collider particle physics experiments is becoming increasingly important to exploit any hint of detection that might appear in the future. However, the connection between the results from collider experiments and those from direct and indirect dark matter searches is not straightforward, since one needs to assume a particular physics model. One common strategy that has been used thus far is to use a set of benchmark simplified models in which the results from different experiments can be compared in equal terms. This is sometimes referred to as the Minimal Simplified Dark Matter (MSDM) model [153, 154].

Under the MSMD model, the LHC has set competitive upper limits on the spin-independent WIMP-nucleon scattering cross section (assuming a vector mediator) for $m_\chi \leq 5\,\mathrm{GeV/c^2}$. In addition, they have set tighter limits than direct detection experiments on the spin-dependent scattering cross section (assuming an axial-vector mediator) at DM masses of up to $\sim 300\,\mathrm{GeV/c^2}$ [155]. However, it should be highlighted that this comparison of results is only valid for the particular combination of model and parameter choices that is assumed.

Most importantly, collider and direct detection searches are complementary to each other. Collider searches are limited by the fact that the dark matter particle mass can only be approximately half the mediator mass, whereas direct detection searches have currently a sensitivity barrier imposed by the coherent scattering of solar neutrinos (i.e. the neutrino floor). In the future, the LHC will continue to set constraints on the mediator mass (which can be translated to limits on the WIMP-nucleon scattering cross section for light to medium DM masses under the MSMD model), while direct detection searches will have the largest sensitivity to scattering cross sections for dark matter masses above a few hundred $\mathrm{GeV/c^2}$.

Chapter 3

Direct detection of WIMPs with dual-phase xenon

In this chapter we provide the theoretical and experimental foundations for the work that will be presented in the following chapters. Firstly, we explore the different ingredients that are needed for the calculation of the expected nuclear recoil rate from WIMP-nucleus interactions. Secondly, we give an account of the advantages that the noble element xenon offers as a target for WIMP detection, and we present the description of arguably the most sensitive technology to date for the direct search of WIMP dark matter: the liquid xenon time projection chamber.

The chapter then introduces the LUX-ZEPLIN (LZ) experiment and some of its main characteristics are discussed. A figure of merit for the electron recoil discrimination level in LZ is discussed based on simulated data similar to those that will be obtained during the detector's calibration campaign. The chapter concludes with a summary of the dominant backgrounds for the WIMP search in LZ.

3.1 WIMP-induced nuclear recoil rate

In the previous chapter it was argued that one well motivated dark matter candidate is the weakly interacting massive particle (WIMP). If the dark matter halo of our own Milky Way galaxy were composed of WIMPs, then a WIMP flux should be crossing the Earth continuously. Despite the fact that WIMP-nucleon interactions are predicted to be extremely rare, this flux of WIMPs is large enough to be, in principle, detectable in Earth-based detectors via their elastic scattering off atomic nuclei (as originally proposed in Ref. [156]).

The differential scattering rate of such nuclear recoils, expressed as a function of deposited energy per day and per kilogram of detector material, takes the form [157]

$$\frac{dR}{dE_R} = \frac{\rho_0}{m_\chi m_A} \int_{v_{\min}}^{\infty} v f_\oplus(\boldsymbol{v},t) \frac{d\sigma_A}{dE_R} d^3v \, . \tag{3.1}$$

In this expression m_χ is the WIMP mass, ρ_0 is the local WIMP density and m_A is the target nucleus mass; $f_\oplus(\boldsymbol{v},t)$ is the WIMP velocity distribution in the detector rest frame and $v = |\boldsymbol{v}|$ represents the WIMP velocity in the galactic rest frame. The details regarding the scattering between WIMPs and atomic nuclei are contained in the velocity integral. The WIMP-nucleus differential cross section, $d\sigma_A/dE_R$, encodes the nuclear response to its interaction with WIMPs, while $(\rho_0/m_\chi)vf_\oplus(\boldsymbol{v},t)$ is the velocity-weigthed flux of WIMPs passing through the experiment. Therefore, the product of those two factors becomes the probability of a WIMP interacting with a target nucleus and imparting an energy E_R. This is integrated over all the kinematically-allowed WIMP velocities to complete our calculation of the expected differential scattering rate.

The lower bound of the integral is given by the minimum WIMP velocity that can induce a nuclear recoil of energy E_R, given by

$$v_{\min} = \sqrt{\frac{m_A E_R}{2\mu_A^2}} \, . \tag{3.2}$$

Here, $\mu_A = m_\chi m_A/(m_\chi + m_A)$ is the WIMP-nucleus reduced mass. Thus, note that the expression for the minimum WIMP velocity depends on the recoil energy E_R, the target mass m_A and the WIMP mass m_χ. The upper integration limit is formally set to infinity, although a maximum velocity v_{esc} is usually assumed above which WIMPs are no longer gravitationally bound to the Milky Way. This is usually taken into account by the WIMP velocity distribution, as we discuss next.

3.1.1 WIMP astrophysics

Equation (3.1) highlights the degeneracy between the WIMP-induced differential scattering rate and the *local WIMP density*, ρ_0. Consequently, any uncertainty on this parameter will have a direct impact on a measurement of the scattering rate, ultimately affecting our ability to place constraints, or measure, scattering cross sections accurately.

In direct dark matter searches the canonical assumption to date has been that $\rho_0 = 0.3\,\mathrm{GeV/cm^3}$ (or equivalently $0.008\,\mathrm{M_\odot pc^{-3}}$). Estimates of this parameter have fluctuated over the past three decades (see e.g. , Ref. [158]). More recent calculations, especially after the second data release from the Gaia space mission [159], suggest larger values around $\rho_0 = 0.5\,\mathrm{GeV/cm^3}$ [160, 161].

Regarding the *WIMP velocity distribution*, a Maxwell-Boltzmann distribution truncated at the Milky Way's escape velocity, v_{esc}, is the most common choice. This is part of the so-called Standard Halo Model (SHM), which assumes an isotropic and spherically symmetric distribution of dark matter around the Milky Way's galaxy. Such a model provides an asymptotically flat rotation curve, which as we saw in Section 2.1 is a characteristic feature of spiral galaxies. In the galactic frame, the SHM velocity distribution takes the form

$$f(\boldsymbol{v}) = \begin{cases} \frac{N_{\mathrm{SHM}}}{(2\pi\sigma_r^2)^{3/2}} e^{-\frac{|\boldsymbol{v}|^2}{2\sigma_r^2}} & |\boldsymbol{v}| < v_{\mathrm{esc}} \\ 0 & |\boldsymbol{v}| > v_{\mathrm{esc}} \end{cases} \tag{3.3}$$

where $\boldsymbol{v}$ is the WIMP velocity in the galactic rest frame, σ_r is the radial velocity dispersion and N_{SHM} is a normalisation factor, which converges asymptotically to one for larger values of v_{esc}.

Under hydrostatic equilibrium, as it is assumed in the SHM model, the radial velocity dispersion can be expressed in terms of the circular velocity at the solar position, v_0, as follows (see Appendix A of Ref. [162] for the full derivation)

$$\sigma_r^2 = \frac{v_0^2}{2} \,. \tag{3.4}$$

Taking the above into account, we can rewrite the SHM velocity distribution as

$$f(\boldsymbol{v}) = \begin{cases} \frac{N_{\mathrm{SHM}}}{(\pi v_0^2)^{3/2}} e^{-\frac{|\boldsymbol{v}|^2}{v_0^2}} & |\boldsymbol{v}| < v_{\mathrm{esc}} \\ 0 & |\boldsymbol{v}| > v_{\mathrm{esc}} \end{cases} \tag{3.5}$$

This alternative expression has the advantage that it is fully specified with only two parameters: the modulus of the local circular velocity, v_0, and the galactic escape velocity, v_{esc}. The canonical values for these two parameters are $220\,\mathrm{km/s}$ [163] and $544\,\mathrm{km/s}$ [164], respectively.

The above velocity distribution has to be translated to the detector rest frame in order to be used in the recoil rate formula from (3.1). This can be achieved by carrying out a Galilean translation to the Earth frame, such that

$$f_{\oplus}(\boldsymbol{v},t) = f(\boldsymbol{v}+\boldsymbol{v}_{\mathrm{E}}(t),t). \tag{3.6}$$

In this expression $\boldsymbol{v}_{\mathrm{E}}(t)$ is the velocity of the Earth relative to the galactic rest frame, which has three components:

$$\boldsymbol{v}_{\mathrm{E}}(t) = \boldsymbol{v}_0 + \boldsymbol{v}_{\odot,\mathrm{pec}} + \boldsymbol{v}_{\oplus,\mathrm{orb}}(t); \tag{3.7}$$

$\boldsymbol{v}_0$ is the Sun's circular velocity in the galaxy given in galactic coordinates, $\boldsymbol{v}_{\odot,\mathrm{pec}}$ is the peculiar velocity of the Sun, and $\boldsymbol{v}_{\oplus,\mathrm{orb}}(t)$ is the Earth's orbital velocity around the Sun. Typical values for the first and second components are $(0,220,0)$ and $(8.5,13.4,6.5)$ km/s [165], while specific parametrisations for $\boldsymbol{v}_{\oplus,\mathrm{orb}}(t)$ can be found in Refs. [166, 167]. The last component changes in value throughout the year, with an average value of approximately 30 km/s. Consequently, $\boldsymbol{v}_{\mathrm{E}}(t)$ introduces a putative annual modulation in the expected WIMP recoil rate, and there exist dedicated experiments looking for this time dependent signal, as mentioned in the previous chapter.

Although the standard halo model is a reasonable approximation and fulfils the goal of making the comparison of results between different direct dark matter searches easier, there are firm reasons to believe that it is not an accurate description of the dark matter distribution in the Milky Way. We will return to this topic in Chapter 5, where we consider more recent models.

3.1.2 WIMP-nucleus cross section

The WIMP-nucleus differential cross section in Eq. (3.1), $d\sigma_A/dE_R$, contains the details regarding the interaction between WIMPs and nuclei. The scattering of WIMPs off nuclei occurs at relatively small velocities ($v \sim 0.001c$), and hence the interactions is generally treated as non-relativistic. Many theoretical approaches have been proposed to describe WIMP-nucleus interactions. One possible avenue is to treat WIMP-nucleon scattering in a model independent way by introducing a complete set of momentum- and velocity- dependent WIMP-nucleon operators. This approach, known as the non-relativistic effective field theory (EFT) of direct dark matter detection, can be considered as the most general modelling of the WIMP-nucleus response, and it is best summarised in Refs. [168, 169]. In addition, an expansion of the effective theory of QCD, the so-called chiral effective field theory (chiral EFT) [170], has revealed a new interaction channel based on the coupling of WIMPs to virtual pions exchanged between two nucleons within the nucleus, which has recently been constrained by the XENON1T experiment [171].

In order to compare experimental results, direct dark matter experiments have traditionally identified two main types of interaction between WIMPs and nuclei: the spin-independent (SI) interaction, in which the WIMP couples to the mass of the nucleus, and the spin-dependent (SD) interaction, in which the WIMP couples to the spin of the nucleus [46]. This is also the approach that will be adopted in the present thesis, so that the LZ sensitivity to WIMP dark matter presented in the next chapter can be easily compared to other experimental searches. However, it is worth highlighting that other scattering models exist. In fact, the SI and SD interactions are special cases of the EFT formalism.

In the standard SI and SD analysis the differential WIMP-nucleus cross section is composed of two parts:

$$\frac{d\sigma_A}{dE_R} = \left(\frac{d\sigma_A}{dE_R}\right)_{\mathrm{SI}} + \left(\frac{d\sigma_A}{dE_R}\right)_{\mathrm{SD}} . \tag{3.8}$$

Both contributions are equally important, but their actual weight to the total scattering rate is unknown. Therefore, and mainly to make the comparison of results between different experimental searches more straightforward, the two types of interaction are usually considered independently. The two terms in (3.8) are discussed below separately.

Spin-independent scattering

The spin-independent scattering arises to first order from WIMP couplings to quarks, mediated via a Higgs or squark exchange [46]. The dependence on the momentum transfer in the WIMP-nucleus interaction is usually parametrised by a nuclear form factor, $F^2(E_R)$. This captures the loss of scattering coherence with increasing momentum transfer as predicted by the nuclear optical model. For low momentum transfers the scattering off nucleons is in phase, resulting in a coherent addition of amplitudes that introduces an enhancement in the probability of interaction proportional to the square of the number of nucleons [93].

The differential WIMP-nucleus cross section for SI scattering is [157]

$$\left(\frac{d\sigma_A}{dE_R}\right)_{\mathrm{SI}} = \frac{m_A}{2\mu_A^2 v^2} F_{\mathrm{SI}}^2(E_R)\sigma_A , \tag{3.9}$$

where $F_{\mathrm{SI}}^2(E_R)$ is the spin-independent form factor, v is the WIMP velocity as defined in the previous section, μ_A is the WIMP-nucleus reduced mass and σ_A is the WIMP-nucleus cross section at zero momentum transfer.

It is preferable to write the differential WIMP-nucleus cross section in terms of the WIMP-*nucleon* cross section, which is a more common parameter used across different dark matter experiments to compare results. Assuming that the coupling of WIMPs to neutrons and protons is similar ($f_p \approx f_n$), these two cross sections are related by [172]

$$\sigma_A = \left(\frac{\mu_A}{\mu_p}\right)^2 A^2 \sigma_N^{\mathrm{SI}} , \tag{3.10}$$

where σ_N^{SI} is the SI WIMP-nucleon cross section, μ_p is the WIMP-proton reduced mass and A is the mass number of the target. The above expression contains the A^2 enhancement that was mentioned previously, which motivates the use of heavy targets to increase the sensitivity to SI scattering ($A > 20$, in practice). As a result, (3.9) becomes

$$\left(\frac{d\sigma_A}{dE_R}\right)_{\mathrm{SI}} = \frac{m_A}{2\mu_p^2 v^2} A^2 F_{\mathrm{SI}}^2(E_R) \sigma_N^{\mathrm{SI}} . \tag{3.11}$$

We adopt the Helm form factor for $F_{\mathrm{SI}}^2(E_R)$, which treats the atom as a solid sphere with a smooth nucleon density transition to zero in the skin [173]. It is usually written as

$$F_{\mathrm{SI}}^2(E_R) = \left(\frac{3 j_1(q r_n)}{q r_n}\right)^2 e^{-(qs)^2}, \tag{3.12}$$

where $q = \sqrt{2 m_A E_R}$ is the momentum transfer, and we consider the Lewin-Smith parametrisation of the nuclear radius [93], that is, $r_n = \sqrt{c^2 + 7/3\pi^2 a^2 - 5s^2}$ with $c = 1.23 A^{1/3} - 0.60$ fm, $s = 0.9$ fm and $a = 0.52$ fm. A pronounced loss of coherence is expected to occur when the incoming de Broglie wavelength ($\lambda_{\mathrm{B}} = h/q$) becomes similar to the size of the nucleus ($\sim r_n$) [93],

$$\begin{aligned} \lambda_{\mathrm{B}} &\approx r_n \\ \frac{h}{\sqrt{2 m_A E_R}} &\approx 1.14 A^{1/3} \end{aligned} \tag{3.13}$$

where a simpler parametrisation for the nuclear radius was used. Rearranging this expression we can find the recoil energy at which a sharp decrease of the scattering probability is expected. Some examples of this pronounced decrease in the form factor are shown in the right panel of Figure 3.1 for different target elements, where A is taken as the standard atomic weight in each case (i.e. the average of the mass number of all the stable isotopes weigthed by their abundance). It is important to highlight that the position of this resonance varies slightly for each of the different isotopes of one given element. Henceforth, we will use the “averaged A” form factor as a representative of each target element, but note that this is yet another approximation.

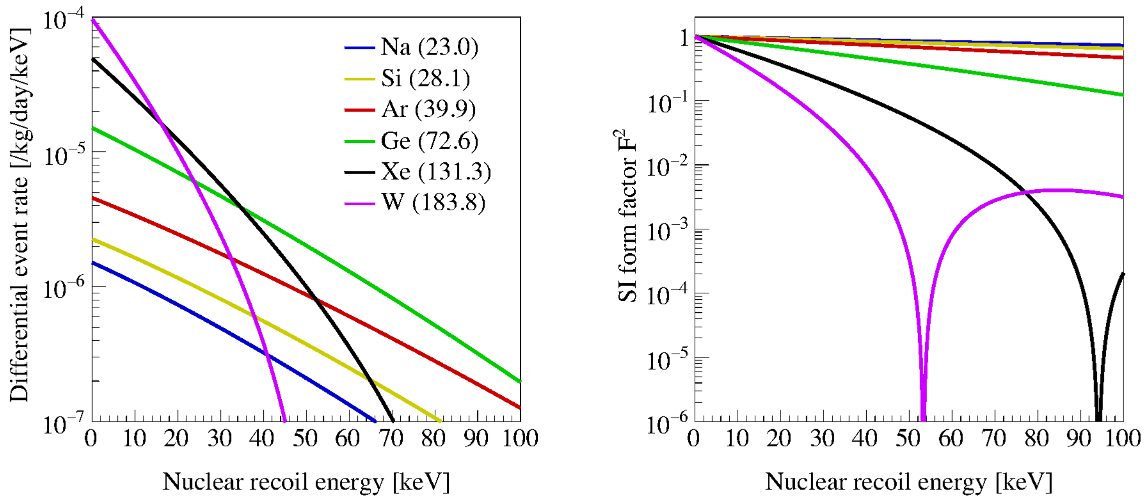

Figure 3.1: *Left:* The SI nuclear recoil rate for several target elements. A WIMP mass of 100 GeV/c^2 and a WIMP-nucleon cross section of $\sigma_N^{\rm SI} = 1$ zb are assumed, as well as the SHM WIMP velocity distribution. The averaged atomic mass of each target element at natural abundance is indicated next to its symbol in the legend. *Right:* The SI form factor defined in (3.12) for several target nuclei. The different colours correspond to the same elements considered in the plot on the left.

Putting all of these elements together, we arrive at the following expression for the SI differential event rate

$$\left(\frac{dR}{dE_R}\right)_{\rm SI} = \frac{\rho_0 A^2 \sigma_N^{\rm SI}}{2m_\chi \mu_p^2} F_{\rm SI}^2(E_R) \int_{v_{\rm min}}^{\infty} \frac{f_\oplus(\mathbf{v},t)}{v} d^3v \,. \tag{3.14}$$

Note that in this expression we have been able to factorise the differential event rate into two parts: one that parametrises the nuclear response with the form factor, and another one that contains all the dependence on the WIMP velocity, which henceforth will be referred to as

$$\zeta(E_R,t) = \int_{v_{\rm min}(E_R)}^{\infty} \frac{f_\oplus(\mathbf{v},t)}{v} d^3v \,. \tag{3.15}$$

An analytic expression of $\zeta(E_R,t)$ assuming the SHM velocity distribution, defined in (3.5), can be found in Ref. [174].

The left plot of Figure 3.1 shows the expected SI differential event rate for a collection of target elements. A WIMP mass of 100 GeV/c^2 and a SI WIMP-nucleon cross section of 1 zb (i.e. 10^{-45} cm^2) are considered. Heavy target nuclei such as Xe or W show a larger event rate for low energy nuclear recoils, which is a direct effect of the A^2 enhancement of the scattering cross section discussed previously. In contrast, the event rate is larger at higher nuclear recoil energies for lighter nuclei, while a more pronounced decrease is observed for heavier nuclei. This can be understood as a combination of two effects: the recoil rate suppression due to the form factor, and a decrease in the number of kinematically-allowed WIMP velocities as v_{min} increases for heavier targets and larger recoil energies. However, the former effect is expected to be dominant, as it becomes apparent in the right panel of Figure 3.1, where the corresponding form factors for the same targets are shown.

Apart from the expected recoil rate, there are other factors to take into account when choosing a particular target element to search for WIMP elastic scattering. Firstly, the lowest feasible energy threshold, which will determine the total integrated rate. This can vary widely amongst different technologies, and it is a key parameter for light WIMP searches. Secondly, the scalability of the experiment, since some targets are easier to scale up than others whilst maintaining a low threshold and background level. Broadly speaking, the target mass of a direct detection experiment can currently range from several kilograms in experiments using crystals (e.g. Ge, NaI or $CaWO_4$) to several tonnes in those using xenon or argon [172].

Spin-dependent scattering

The spin-dependent scattering arises from the axial-vector interaction between WIMPs and quarks [46]. The WIMP-nucleus cross section in this case depends on the total nuclear spin, J, and the spin structure functions, $S_A(q)$, which represent the spin distribution inside the nucleus and they are analogous to the form factor in the SI case.

The nuclear spin can be described by the nuclear shell model which, analogously to the atomic shell model describing the arrangement of electrons in the atom, explains the structure of the nucleus in terms of energy levels. According to this model, contributions to the spin content of the nucleus are cancelled out between pairs of nucleons, and it is only when a nucleus has an odd number of protons or neutrons that the nuclear spin becomes significant. The exact coupling of WIMPs to protons or neutrons is not known, and although in reality there are probably contributions from the two types, it is standard to consider "proton-only" and "neutron-only" interactions separately; that is, the WIMP can only couple to protons in the first case or neutrons in the second one. Consequently, heavy isotopes with and odd number of neutrons will have in general a much larger SD sensitivity to the WIMP-neutron channel—e.g. $^{73}_{32}$Ge, or $^{129}_{54}$Xe and $^{131}_{54}$Xe. Conversely, important odd-proton isotopes include $^{19}_{9}$F, $^{23}_{11}$Na and $^{127}_{53}$I.

Earlier calculations of the spin structure functions were limited to two-body interactions (also referred to as "1-body currents"). With the advent of large-scale computing and the refinement of nuclear shell models this calculation can be currently performed for three-body particle interactions too ("2-body currents"). In particular, Ref. [175] provides parametrisations of the spin structure functions ($S_A(q)$) for several target elements of interest. This calculation takes into account that mixed interactions between one WIMP and both a neutron and a proton can occur. As shown in Fig. 6 of Ref. [175], this can represent an important effect for those isotopes with an odd number of neutrons and an even number of protons, such as $^{129}_{54}$Xe and $^{131}_{54}$Xe, resulting in an increase of sensitivity to WIMP-proton scattering.

The corresponding differential WIMP-nucleus scattering cross section for the SD case is [176]

$$\left(\frac{d\sigma_A}{dq^2}\right)_{\mathrm{SD}} = \frac{\pi\sigma_{n,p}^{\mathrm{SD}}}{3\mu_{n,p}^2(2J+1)v^2} S_{n,p}(q) \;, \tag{3.16}$$

where $q = \sqrt{2m_A E_R}$ is the momentum transfer, J is the total nuclear spin and v is the WIMP velocity. The remainder of the parameters are specific to the WIMP-neutron or WIMP-proton case, with μ being the reduced mass, σ^{SD} the corresponding WIMP-nucleon cross section and $S(q)$ the spin structure function.

The above expression can be transformed into the more common $d\sigma/dE_R$ form by writing

$$\begin{aligned} \frac{d\sigma(E_R)}{dq^2} &= \frac{d\sigma}{dE_R}\frac{dE_R}{dq^2} \\ &= \frac{1}{2m_A}\frac{d\sigma}{dE_R} \end{aligned} \tag{3.17}$$

where in the last derivation we used $E_R = q^2/(2m_A)$.

Integrating these results into (3.1), we obtain the following expression for the SD differential event rate

$$\left(\frac{dR}{dE_R}\right)_{\mathrm{SD}} = \frac{2\pi\rho_0\sigma_{n,p}^{\mathrm{SD}}}{3m_\chi\mu_{n,p}^2(2J+1)} S_{n,p}(E_R) \int_{v_{\min}}^{\infty} \frac{f_\oplus(\boldsymbol{v},t)}{v} d^3v \;, \tag{3.18}$$

where $f_\oplus(\boldsymbol{v},t)$ is the WIMP velocity distribution introduced in Section 3.1.1.

It is important to highlight that only some isotopes of the target material will be sensitive to the SD interaction. Each of the sensitive isotopes will have different total spins and structure functions. Therefore, the above expression has to be summed over all the significant isotopes with the appropriate weighting factor of

$$f_A N_T \,, \tag{3.19}$$

where f_A is the relative abundance of each isotope and N_T is the number of target atoms with isotope T. As a result, the total SD differential rate becomes

$$\left(\frac{dR}{dE_R}\right)_{\mathrm{SD}} = \sum_{i=1}^{N_{\mathrm{iso}}} \frac{(f_A N_T)_i 2\pi\rho_0\sigma_{n,p}^{\mathrm{SD}}}{3m_\chi\mu_{n,p}^2(2J_i+1)} \left(S_{n,p}(E_R)\right)_i \zeta(E_R,t) \;, \tag{3.20}$$

where the summation index i goes over the different isotopes in the target material with an unpaired number of nucleons (i.e. neutrons or protons), N_{iso}. As previously mentioned, $\zeta(E_R,t)$ is the mean inverse velocity function, and a specific parametrisation of it assuming the SHM model can be found in Ref. [174].

The expected WIMP recoil rates from SI, SD neutron-only and SD proton-only scattering on a xenon target are compared in Figure 3.2. Four different WIMP masses are considered, and a nominal scattering cross section of 1 zb is assumed in all cases. The effect of the A^2 enhancements on the SI recoil rate is apparent, making this event rate at least 5 orders of magnitude larger than the corresponding SD recoil rates for all the WIMP masses considered. In addition, the SI scattering rate is greatly affected by the form factor for large recoil energies, as can be seen in the two plots at the bottom. By contrast, the SD scattering rates do not show any abrupt decrease in rate due to the spin nuclear functions in the range of energies considered. Furthermore, a consistent decrease in rate is observed for larger WIMP masses in all the recoil rates. This is due to the fact that the differential rate formulas in Eq. (3.14) and (3.20) lose their implicit dependence on m_χ in both v_{min} and the reduced mass parameters $\mu_{n,p}$ at large values of m_χ. Consequently, the differential recoil rate scales as $1/m_\chi$ in that case.

Henceforth, the expression "vanilla WIMP model" will be used to refer to the standard SI and SD scattering introduced in this section. Moreover, and unless stated otherwise, the parameterisation from Ref. [174] for the mean inverse velocity function $\zeta(E_R,t)$ will be used.

3.2 WIMP identification with dual-phase xenon

We have now introduced expressions to calculate the expected WIMP-nucleus differential recoil rate, and shown examples of such distributions for a variety of nuclear targets. In this section we motivate the use of liquid xenon (LXe) as a WIMP target material, describe its main properties and outline some of the physics opportunities that this target offers.

As previously mentioned, the high atomic mass of Xe provides a high sensitivity to SI WIMP-nucleon scattering interactions due to the A^2 enhancement. The left panel in Figure 3.1 shows the expected scattering recoil rate for a range of targets. This plot shows that a Xe target offers a good compromise between large recoil rates at low recoil energies and a less

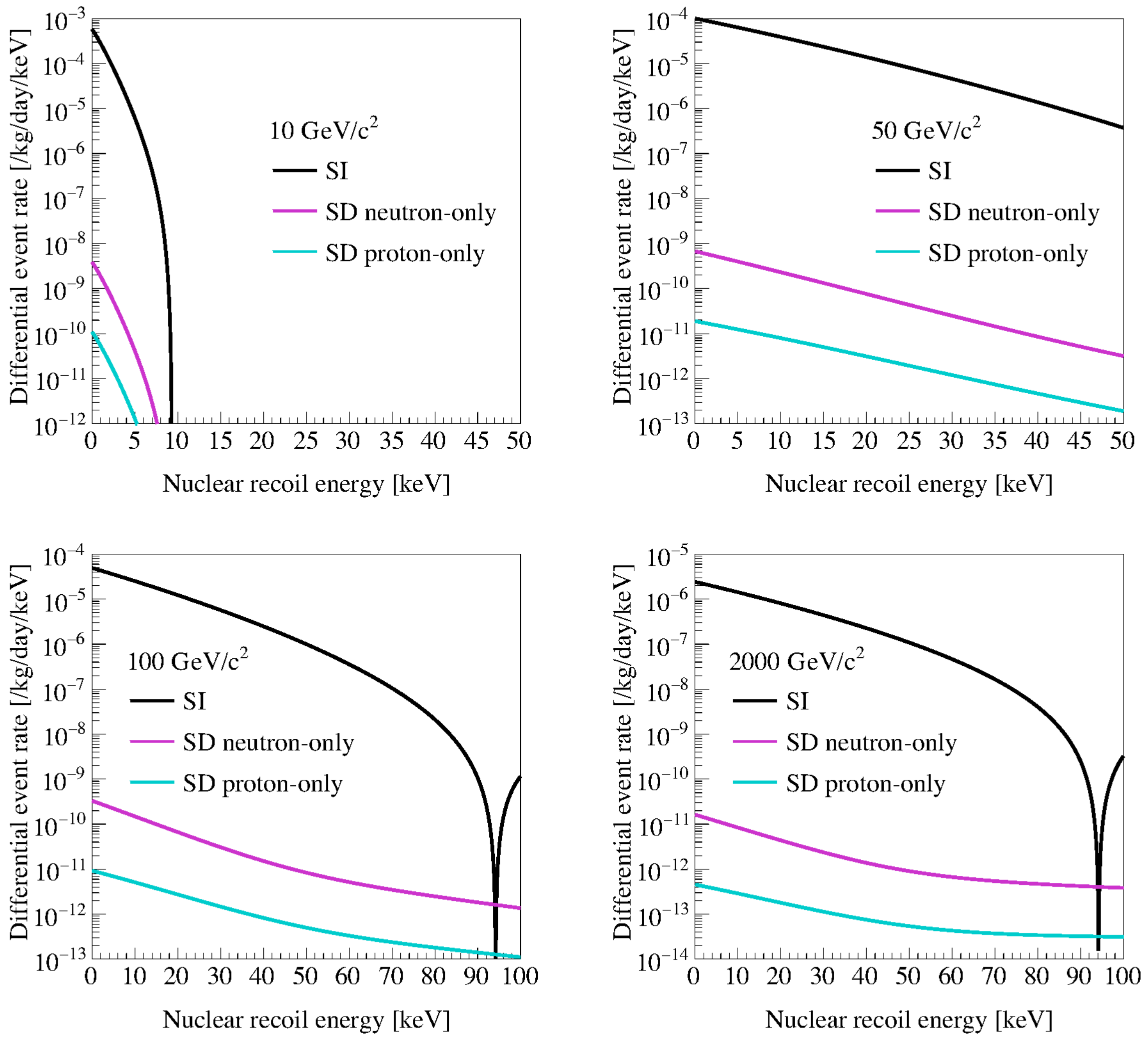

Figure 3.2: The SI, SD neutron-only and SD proton-only differential recoil rate in a Xe target for several WIMP masses: 10, 50, 100 and 2000 GeV$/$c^2 (from top left to bottom right). A nominal WIMP-nucleon cross section of 1 zb is assumed as well as the SHM WIMP velocity distribution. The recoil spectra are normalised per kilogram of natural xenon. Only the odd-neutron isotopes $^{129}_{54}$Xe and $^{131}_{54}$Xe make a significant contribution to the SD scattering rates, while the standard atomic weight of xenon is considered to calculate the SI scattering rate.

pronounced fall-off at larger energies, compared to even heavier targets such as tungsten (W). Moreover, it is sensitive to spin-dependent interactions via the two odd-neutron isotopes ^{129}Xe and ^{131}Xe. These two isotopes constitute approximately half of the isotopic abundance of natural Xe (26.4% and 21.1%, respectively), making the search for SD WIMP scattering with a Xe target competitive. In addition, if particle dark matter scattering were discovered, the properties of this new particle could be further studied—in the same experiment—by altering the isotopic composition.

In addition, natural Xe does not contain either problematic long-lived radioactive isotopes or activation products with a long lifetime. The only isotopes of concern are those that could be cosmogenically produced while the Xe is in storage, such as ^{127}Xe, ^{129m}Xe, ^{131m}Xe[1] and ^{133}Xe. Fortunately, they are expected to decay rapidly (their half-life is of the order of tens of days), and their contribution to the background of an experiment becomes negligible after the first few months of commissioning before the start of data taking.

All the stable isotopes of Xe are listed in Table 3.1. Apart from the SI and SD scattering already mentioned, some of the Xe isotopes are also sensitive to double electron capture (DEC), which is a rare weak process in which two electron capture (EC) processes happen simultaneously. This decay can be accompanied by the emission of two electron neutrinos, a process that has recently been measured in ^{124}Xe [177], or with zero neutrinos which, if observed, would imply the violation of lepton number conservation and that neutrinos are Majorana particles [178]. Furthermore, ^{134}Xe and ^{136}Xe are sensitive to double beta decay with two neutrino emission $(2\nu\beta\beta)$, a process already observed in ^{136}Xe [179, 180], and to neutrinoless double beta decay $(0\nu\beta\beta)$. The discovery of neutrinoless double beta decay would also imply that neutrinos are Majorana particles. In fact, this is currently an active field of research, with several experiments worldwide employing ^{136}Xe in various technologies (e.g. EXO-200 [181], KamLAND-Xen [182] and NEXT-100 [183]).

In addition, liquid xenon is an excellent medium to be used for self-shielding. The relatively high density of Xe in the liquid phase—approximately $3\,\mathrm{g/cm^3}$ at boiling point [184]—combined with a technology capable of reconstructing the full event position with high precision, allows for the definition of an outer layer of the target (in data analysis) that shields a low background fiducial region at the centre of the detector. Neutrons and MeV gamma-rays have a mean interaction length of only a few centimetres in LXe, while for X-rays it is even shorter, of the order of a few millimetres [1]. Consequently, defining an outer layer of LXe of only a few centimetres can drastically reduce the background expectation from external radiation and neutrons in the fiducial region. Multi-tonne experiments will benefit greatly from

[1] The "m" in the superscript indicates that these are metastable isomers of Xe.

Table 3.1: List of isotopes in natural xenon. For each isotope the following information is given: natural abundance (N.A.), half-life, nuclear spin and physics processes they are sensitive to. SD for "spin-dependent scattering", DEC stands for "double electron capture" and $n\nu\beta\beta$ for "double beta decay", where the last two could have both a two-neutrino (2ν) and zero-neutrino mode (0ν). Isotopic abundances are from [190], and lower limits on the half-life of some of the isotopes are indicated (the ones marked with a dash are known to be stable).

Isotope	**N.A.** (%)	$T_{1/2}$ (y)	J	**Sensitive to**
^{124}Xe	0.09	$> 1.8 \times 10^{22}$ [177]	0	$n\nu$DEC
^{126}Xe	0.09	$[5\text{-}12] \times 10^{25}$ [187]	0	$n\nu$DEC
^{128}Xe	1.92	–	0	–
^{129}Xe	26.44	–	$1/2$	SD
^{130}Xe	4.08	–	0	–
^{131}Xe	21.18	–	$3/2$	SD
^{132}Xe	26.89	–	0	–
^{134}Xe	10.44	$> 5 \times 10^{24}$ [188]	0	$n\nu\beta\beta$
^{136}Xe	8.87	2.17×10^{21} [189]	0	$n\nu\beta\beta$

this: LZ, for instance, will have a fiducial mass of approximately 6 tonnes, which represents 85% of the active mass of the detector. This is comparably larger than the case of previous experiments such as LUX and XENON100, whose fiducial regions were about half of their active mass [185, 186].

Next, we review the emission mechanism of scintillation and ionisation quanta in liquid xenon, followed by a description of the operational principle of the liquid xenon time projection chamber.

3.2.1 Response of liquid xenon to particle interactions

Production mechanisms of light and charge

When a particle interacts in the liquid xenon, it leads to either an electron recoil (ER) or a nuclear recoil (NR). Having the ability to discriminate between these two types of signal is important, since WIMPs are expected to interact with the nucleus, while the dominant backgrounds are expected to create ER events. After a WIMP scatters off an atomic nucleus, the recoiling atom will move through the liquid transferring a significant fraction of its kinetic energy to nearby atoms and, therefore, producing a cascade of secondary recoils.

The track structure is different for nuclear and electron recoils. In general, nuclear recoils leave shorter and higher density tracks due to their larger stopping power compared to electron recoils. In addition, in nuclear recoils a significant fraction of the recoil energy is transferred to other atoms, which generates heat via atomic motion. These two effects result in a distinct signature for ER and NR events that can be exploited experimentally. To understand this properly, we must look first at the other two mechanisms, apart from atomic motion, in which a particle can transfer energy to the electronic systems of atoms in the medium: excitation and ionisation.

Both scintillation photons and ionisation electrons will be produced as a result of the energy transfer from the interacting particle to atomic electrons. On the one hand, photons are emitted from the relaxation of diatomic excited molecules (Xe_2^*), which can be created from two possible mechanisms. Firstly, when an excited Xe atom finds another Xe atom and forms a strongly bound diatomic molecule in the excited state (i.e. an excimer). A single electronically excited atom (Xe^*) is usually referred to as an "exciton", so this process is known as *exciton luminescence* and proceeds along the following steps:

$$
\begin{array}{ll}
e^- + \mathrm{Xe} \to \mathrm{Xe}^* + e^- & \text{impact excitation} \\
\mathrm{Xe}^* + \mathrm{Xe} \to \mathrm{Xe}_2^{*\nu} & \text{excimer formation} \\
\mathrm{Xe}_2^{*\nu} + \mathrm{Xe} \to \mathrm{Xe}_2^* + \mathrm{Xe} & \text{relaxation} \\
\mathrm{Xe}_2^* \to 2\mathrm{Xe} + \gamma & \text{VUV emission}
\end{array}
$$

The star in the superscript is used to indicate that the molecule is electronically excited, while ν indicates that the molecule is vibrationally excited too. The vibrational relaxation is mostly non-radiative, and only a small intensity of near infrared (NIR) emission is expected in LXe. By contrast, the dissociation of the excimer is always accompanied by the emission of a photon, as indicated in the last step. These scintillation photons have a wavelength in the vacuum ultraviolet (VUV) region, centred near 175 nm [191].

Secondly, VUV photons can also be emitted from the recombination of ionisation electrons with positive ions. This process, hereafter referred to as *recombination luminescence*, has the following steps:

$$
\begin{array}{ll}
e^- + \mathrm{Xe} \to \mathrm{Xe}^+ + 2e^- & \text{ionisation} \\
\mathrm{Xe}^+ + \mathrm{Xe} + \mathrm{Xe} \to \mathrm{Xe}_2^+ + \mathrm{Xe} & \\
e^- + \mathrm{Xe}_2^+ \to \mathrm{Xe}^{**} + \mathrm{Xe} & \text{recombination} \\
\mathrm{Xe}^{**} + \mathrm{Xe} \to \mathrm{Xe}^* + \mathrm{Xe} & \\
\mathrm{Xe}^* + \mathrm{Xe} + \mathrm{Xe} \to \mathrm{Xe}_2^* + \mathrm{Xe} & \\
\mathrm{Xe}_2^* \to 2\mathrm{Xe} + \gamma & \text{VUV emission}
\end{array}
$$

Here, the double star in the superscript indicates that the atom is in a higher electronic excited state. The final stage of this process is similar to the previous case and therefore the properties of the emitted photon are similar, including its wavelength and decay time. In addition, some infrared radiation is released in this process too but its contribution is negligible. By contrast, the recombination process introduces a considerable time delay, of approximately 45 ns in liquid xenon [192].

The VUV emission occurs in a transition to the ground state from one of the two lowest electronic excited states of the excimer: the singlet $\left({}^1\Sigma_{\rm ex}^+\right)$ or tripled $\left({}^3\Sigma_{\rm ex}^+\right)$ state. The transition to the ground state results in the dissociation of the molecule, and therefore the emitted VUV photon is not reabsorbed in the medium since the probability of finding other Xe_2 molecules around is very low. Also, the decay time constants of these two transitions are very short, specifically 2.2 ns and 27 ns, respectively [109]. By contrast, the triplet lifetime in LAr is long ($\sim$1 μs), and the corresponding singlet lifetime is approximately three orders of magnitude shorter. This feature is exploited by liquid argon dark matter experiments to discriminate between ER and NR events, as mentioned in the previous chapter.

On the other hand, any ionisation electron that is not captured by a positive ion will escape the interaction site as a free electron. Consequently, any newly formed ionisation electron can either escape the interaction site as a free charge, or be captured by a Xe_2^+ ion, which will create an additional Xe_2^* excimer that will result in an extra scintillation photon. As a result, the process of recombination introduces an *anticorrelation* between the scintillation and ionisation signals in liquid xenon [193]. Recombination depends on both the electric field that is applied to the medium and the recoil energy, and it is generally small for low recoil energies and high applied electric fields.

Furthermore, at high energies ($\gtrsim$ MeV) new processes start to emerge that can decrease the number of primary scintillation photons. At these energies the density of excited atoms along the particle track is high enough so that the probability of interaction between two exited atoms becomes significant. In such case, the autoionisation of xenon atoms from two colliding excited atoms becomes possible, a process called “bi-excitonic quenching” [192]:

$$\mathrm{Xe}^* + \mathrm{Xe}^* \rightarrow \mathrm{Xe} + \mathrm{Xe}^+ + e^- \tag{3.21}$$

The consequence of this is that instead of two emitted photons from each of the excited xenon atoms, via exciton luminescence under normal conditions, there will be at most one photon emitted from the recombination of the Xe^+ ion with an electron.

Taking the above into account, we can express the number of emitted VUV photons (n_γ) and extracted electrons (n_e) in a particle interaction in the liquid xenon as

$$\begin{aligned} n_\gamma &= N_{\text{ex}} + rN_{\text{ion}} \\ n_e &= (1-r)N_{\text{ion}} \end{aligned} \tag{3.22}$$

where N_{ex} and N_{ion} are the initial number of excited and ionised atoms prior to recombination, respectively, and r is the recombination probability. Ionised atoms that recombine result in the emission of a single photon, and therefore,

$$N_{\text{ex}} + N_{\text{ion}} = n_e + n_\gamma \,, \tag{3.23}$$

which is independent of recombination.

It has been experimentally verified that electron and nuclear recoils exhibit a different ratio of initial excitons to ions produced at the interaction site. While $N_{\text{ex}}/N_{\text{ion}} \approx 0.06$ for electron recoils, for nuclear recoils $N_{\text{ex}}/N_{\text{ion}} \sim 1$ [194], and this ratio is known to be independent of the recoil energy [195]. Since recombination is expected to be similar for both ER and NR events [195], this difference in the initial number of excited to ionised atoms will result in a different ratio of free charges to primary scintillation photons. It is generally accepted that this is the origin of the different charge-to-light ratio between ER and NR events that dark matter liquid xenon experiment exploit on a regular basis [194]. However, it is important to highlight that the recoil energy and the applied electric field will have an effect on this charge-to-light ratio too, and hence affecting the ability of the experiment to discriminate ER events.

It has been recognised for some years that the energy of an electron recoil can be best estimated from the simultaneous measurement of the primary scintillation photons (n_γ) and the ionisation electrons that escape recombination (n_e),

$$E_R = W(n_e + n_\gamma) \quad \text{(electron recoils)}, \tag{3.24}$$

where W (the "W-value") is the average energy required to produce either an exciton or a ion, and has an approximated value of 13.7 eV in LXe [195]. The advantage of this energy scale is that it is linear with recoil energy and independent of the applied electric field due to the anticorrelation of the two channels [196].

For nuclear recoils, one has to take into account that a considerable fraction of energy is transferred into atomic motion. As a result, a correction factor is applied to the recoil energy formula,

$$E_R = (W/\mathcal{L})\,(n_e + n_\gamma) \quad \text{(nuclear recoils).} \tag{3.25}$$

Here, $\mathcal{L}$ is referred to as the "quenching factor" and it is the fraction of the recoil energy that is transferred to electronic excitation instead of atomic motion. This factor increases monotonically as a function of nuclear recoil energy, from a value of approximately 0.15 at 1 keV to 0.30 at 100 keV [194]. The theoretical basis for the calculation of the quenching factor was originally laid out by Lindhard *et al*. in the 1960s [197], and their theory is still used to analyse modern nuclear recoil data in liquid xenon [194]. Hence, $\mathcal{L}$ is sometimes referred to as the "Lindhard factor" as well. Also, to make this separation between ER and NR energies more explicit, it is common to report the former in $\mathrm{keV_{ee}}$ (electron recoil equivalent energy) and the latter in $\mathrm{keV_{nr}}$ (nuclear recoil equivalent energy).

For a complete review of the detection principles in liquefied noble gases, such as argon or xenon, see for instance Ref. [109].

Scintillation and ionisation yields

Xenon has a good kinematic match to intermediate WIMP masses ($\approx 100\,\mathrm{GeV/c^2}$), but sensitivity to lower WIMP masses is also possible given the high scintillation and ionisation yields of LXe at low energies. Figure 3.3 shows the electron recoil and nuclear recoil scintillation and ionisation yields in this medium, defined respectively as

$$\begin{aligned} Q_\mathrm{y} &= n_e/E_R \\ L_\mathrm{y} &= n_\gamma/E_R \end{aligned} \tag{3.26}$$

Here, n_e is the number of free electrons, n_γ is the number of primary scintillation photons and E_R is the recoil energy. We select some key datasets to motivate the discussion, but it is important to highlight that more measurements of the liquid xenon response at low energies exist [109].

The yields for electron recoils are shown in the upper panel. Data points include measurements from LUX calibrations using tritiated methane (CH_3T) [198] and ^{127}Xe [199] at a drift field of 180 V/cm, and from the PIXeY detector using a ^{37}Ar source and operating at a drift field of 198 V/cm [200], which constrain the ionisation yield down to approximately 0.3 keV. On the other hand, the lower panel of Figure 3.3 shows the scintillation and ionisation yields for nuclear recoils. Measurements from LUX using a deuterium-deuterium (D-D) neutron source are indicated by filled markers, with the lowest data point registered at 0.7 keV in the ionisation yield [201].

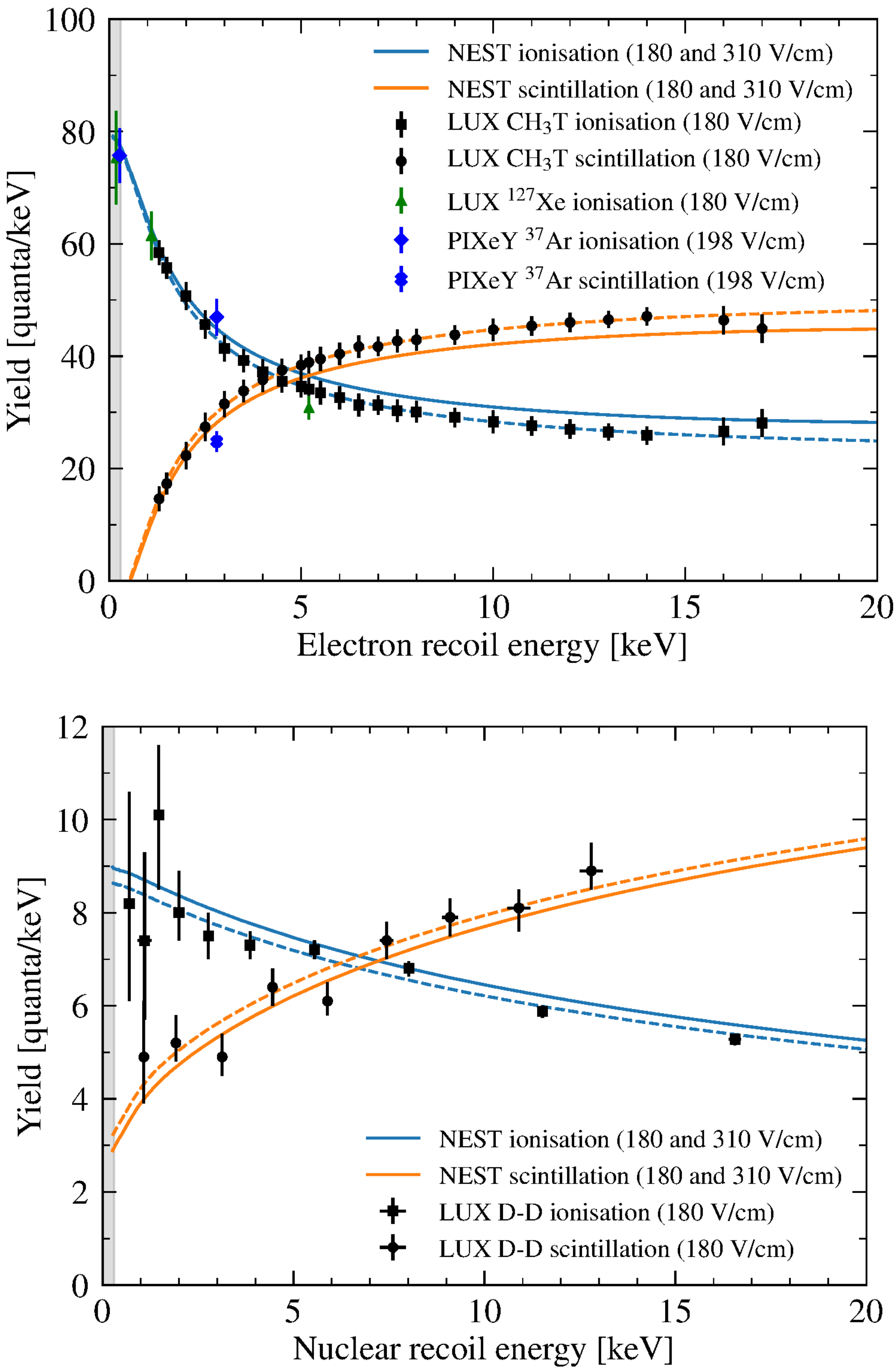

Figure 3.3: Liquid xenon scintillation and ionisation yields for electron recoils (upper panel) and nuclear recoils (lower panel). The orange and blue lines show the NEST prediction of the scintillation and ionisation yield, respectively, at a drift electric field of 180 V/cm (dashed) and 310 V/cm (solid). Measurements from the LUX CH_3T [198] and ^{127}Xe [199] calibrations are overlapped, as well as the PIXeY measurements with a ^{37}Ar source at 198 V/cm drift field [200]. An energy cut at 0.3 keV is adopted, and the region below it is marked in grey. In the lower panel, measurements from the LUX D-D calibration [201] are indicated by filled markers.

As mentioned in the previous section, any ionisation electron can contribute to either the scintillation or ionisation signal, but not both. This results in an anticorrelation between the scintillation and ionisation yields, which is apparent in Figure 3.3. Moreover, the ionisation yield increases for larger electric field across the energy range considered, indicating that recombination decreases as the field increases—as one would expect.

The prediction of the liquid xenon yields from the Noble Element Simulation Technique (NEST) model [95, 202] are also shown, assuming a constant drift electric field of either 180 V/cm (solid lines) or 310 V/cm (dashed lines). The former corresponds to the drift field at which LUX conducted the measurements shown in this figure, while the latter is the nominal LZ field [1]. NEST can be understood as a collection of models that predicts the response of noble gas elements as a function of the electric field, particle type, energy, temperature and pressure. A new version of the NEST software package was released in 2018 (`v2.0.0`) [203], which follows a more data-driven approach to match the extensive collection of global data that exists regarding the response of noble gas elements to particle interactions. The present thesis follows that version of the NEST software. However, at the time of writing a new version became available, NEST `v2.0.1`, which predicts a roll-off of the NR ionisation yield at sub-keV energies, mainly motivated by a very recent measurement from Ref. [204]. We will not consider this update in the present thesis for consistency reasons, but it is important to highlight that the liquid xenon yields at very low recoil energies are still subject to significant uncertainties.

In Figure 3.3 we highlighted in grey the region below 0.3 keV. This energy corresponds roughly to the estimated energy where the first ionisation electron and scintillation photon are expected to appear for NR interactions [205]. The partition between electrons and photons is basically 1:1 at low NR energies [194]. As we will see in the next section, single electrons can be detected with almost a 100% probability in LXe TPCs, while the detection efficiency for a single photon is only of approximately 10%. Hence, 0.3 keV represents the lowest energy point at which a reliable measurement of the NR ionisation yields is feasible, with this limit being higher for the scintillation yield. In fact, the recent measurement of the NR ionisation yield mentioned above from Ref. [204] goes down to 0.3 keV, and the currently lowest measurement of the scintillation yield is from LUX at 1.1 keV [198]. Assuming that the W-value remains constant at these low energies, we infer that photons should be produced below 1.1 keV too, so it is not unreasonable to follow the NEST prediction between those two energies. Hence, a recoil energy cut at 0.3 keV will be adopted henceforth, i.e. we assume no response from interactions below this energy for both ER and NR.

3.2.2 The dual-phase xenon time projection chamber

A liquid-gas xenon time projection chamber (TPC) is a very sensitive detector that can be used to search for dark matter interactions. It exploits the different charge-to-light ratio between electron recoils and nuclear recoils discussed in the previous section on an event-by-event basis. An event in the TPC is characterised by two types of signal: an initial prompt scintillation signal in the liquid phase (S1), and a delayed proportional scintillation signal in the gas phase (S2). The second light signal is created via electroluminescence from ionisation electrons that are drifted through the liquid by an applied electric field, and subsequently extracted to the gas xenon (GXe) region. These two VUV light signals ($\sim$175 nm) are detected by quartz-windowed photomultiplier tubes (PMTs), usually distributed in two arrays at the top and bottom of the TPC.

Figure 3.4 shows an example of a simulated event in the LZ TPC. The S1 and S2 signals are detected with a time difference of approximately 40 µs in this instance, which can be used to determine the z position of an event, as explained below. The amount of light detected by each PMT in the top array is shown on the right. From the photon hit pattern it is possible to reconstruct the position of the interaction in the x-y plane, which in this case corresponds to an event that occurred near the wall of the detector. In addition, the dual-phase TPC technique allows for an accurate identification of multiple scatter events (mainly originated by gamma-rays and neutrons), which are expected to scatter multiple time and therefore produce more than one S2 signal.

The sizes of both S1 and S2 signals are measured in units of "photons detected" (phd). Traditionally, S1 and S2 were described in photoelectrons (phe), obtained by dividing the integrated pulse areas by those obtained from the response to single photoelectrons (SPE) channel by channel. We now understand that, with some non-negligible probability of $\sim$20%, two "photoelectrons" may be emitted in response to a single VUV photon in some photomultiplier models [123, 206]. The phd unit takes this factor into account and thus it is preferred over the older phe unit, which only reflected the total amount of charge detected by the PMTs but is strictly not a good estimator for the number of photons detected.

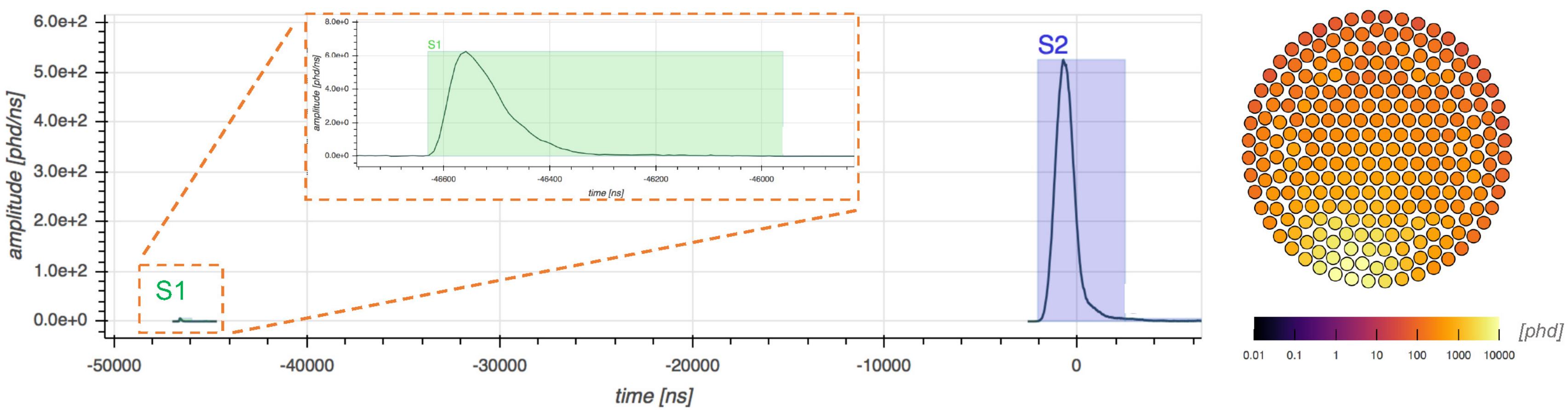

Figure 3.4: An example of a simulated event occurring in the LZ time projection chamber (TPC). The particle interaction generates both photons and electrons in the active region inside the TPC. A prompt scintillation signal is originated in the liquid phase (S1), followed by a delayed proportional scintillation signal in the gas phase (S2). These two VUV light signals ($\sim$175 nm) are detected by two arrays of photomultipliers at the top and bottom of the TPC. The x-y location of the event is reconstructed from the distribution of S2 light measured in the top array, which is shown on the right. The time difference between the two signals is proportional to the event's z position, since electrons travel at constant velocity through the liquid.

Both the position and the energy of an event inside the TPC can be reconstructed from the S1 and S2 signals. Firstly, the x-y position of an interaction inside the TPC can be reconstructed from the distribution of S2 pulse areas in the top photomultiplier array. Electrons are not expected to deviate significantly in their journey through the liquid, and hence the photon hit pattern from the S2 signal is a good estimator of the x-y position of an event in the liquid. In fact, this is achieved down to a resolution of $\sim$5 mm, as demonstrated by previous experimental searches [207, 208]. However, the resolution can rapidly degrade for weaker signals, and therefore a minimum S2 signal size corresponding to a few emitted electrons is usually required in data analysis.

In addition, the vertical position of the event is directly proportional to the time difference (Δt) between the S1 and S2 signal. This is because ionisation electrons move at constant velocity through the liquid. The time difference between these two signals can be measured with much greater precision, allowing for a z-resolution of $\sim$100 µm [1]. Moreover, the resolution in z is not expected to change significantly for low signal sizes as long as a pair of S1 and S2 signals is recorded.

Secondly, the S1 and S2 signals can be used to reconstruct the energy of the event. It is first needed to determine the g_1 and g_2 factors, which are the conversion factors between the number of quanta released at the interaction site and the corresponding S1 or S2 signals, respectively. Namely,

$$\begin{aligned} S1 &= g_1 n_\gamma \\ S2 &= g_2 n_e \end{aligned} \tag{3.27}$$

where g_1 is given in units of phd per emitted photon (phd$/\gamma$) and g_2 in phd per free electron (phd$/e^-$). These two factors are usually estimated during the calibration campaign of the experiment, as explained for instance in Ref. [208].

Therefore, and taking into account Eq. (3.24), the recoil energy for electron recoils can be written as

$$E_R = W\left(\frac{S1}{g_1} + \frac{S2}{g_2}\right). \tag{3.28}$$

For nuclear recoils, the above equation needs to be corrected by the quenching factor $(\mathcal{L})$, as discussed earlier.

3.3 The LUX-ZEPLIN (LZ) experiment

3.3.1 Overview of the detector systems

LZ is a multi-tonne dark matter detector employing a dual-phase (liquid and gas) xenon TPC. As its name indicates, LZ builds upon the expertise of two previous collaborations that successfully built and operated such detectors: LUX and ZEPLIN-III. LZ will operate at the Sanford Underground Research Facility (South Dakota, USA) at 4850 feet underground ($\sim$1.5 km or 4300 m water equivalent [209]). The experiment contains a total of approximately 10 tonnes of liquid xenon. The underground installation of the LZ experiment is underway, and it is due to start taking in 2020.

A schematic diagram and a photo of the LZ TPC are shown in Figure 3.5. The active region of the TPC—defined as the volume between the cathode grid at the bottom and the gate grid at the top—is a cylinder of 1.46 m both in diameter and height containing 7 tonnes of LXe. It contains three electrodes: a cathode grid at the bottom, a gate grid below the LXe surface, and an anode grid just after the liquid surface. The TPC is enclosed laterally by 58 sections of 25 mm of height each composed of titanium rings that are embedded in highly reflective polytetrafluoroethylene (PTFE) panels, and connected by resistor ladders. This defines the "field cage", which provides a vertical field across the entire active region. Any charge created in a particle interaction in the active region will drift upwards through the liquid xenon to the electroluminescence region. The projected electron lifetime is 800 µs, which corresponds to a total drift length of 1.5 m from the cathode at the nominal drift field of 310 V/cm. The exposed titanium in the field cage is covered with additional PTFE pieces on both sides of the TPC to maximise the reflectance of light. It is important to highlight that both the PTFE and Ti are extraordinarily radiopure, and they were selected after an intense R&D campaign [210–212]. The PTFE material employed by the LZ experiment has a reflectivity $\geq$97.3% when immersed in LXe [210].

At the top of the TPC, the electroluminescence region is defined from the surface of the liquid to the anode, measuring 8 mm in length. The gate and anode are 13 mm apart, with the liquid xenon 5 mm above the gate. The electric field in the electroluminescence region is 10 kV/cm (also known as the extraction field). By contrast, the electric field in the active region, established between the cathode and the gate, is 310 V/cm. This is achieved after applying an operating voltage of -50 kV to the cathode (for a design voltage of -100 kV). An additional grid is placed on top of the bottom PMT array, around 14 cm below the cathode, to shield the PMT photocathodes from the high field. This creates a "reverse-field" region (RFR) below the cathode from which no ionisation can be detected; interactions in this region produce S1 light only. The nominal value for the reverse field is 2.9 kV/cm.

A diagram of the detector systems at the core of the experiment is shown in Figure 3.6. Photons emitted inside the TPC are detected by 494 Hamamatsu R11410-22 3-inch diameter PMTs, which were developed to have particularly low levels of radioactivity (~1 mBq in I and Th) [213, 214] and high quantum efficiency at the characteristic LXe scintillation wavelength of 175 nm [206]. These PMTs are assembled in two arrays: one immersed in the LXe region at the bottom viewing up and containing 241 units, and the other in the GXe region at the top viewing down and containing 253 units. The arrangement of PMTs has been optimised to maximise the light collection of S1 signals in the bottom array, and to reconstruct the x-y position of the S2 signal in the top array.

The TPC is contained within a vacuum-insulated cryostat made from ultra-pure titanium [212]. The cryostat is composed of two chambers: the inner cryostat vessel (ICV) and the outer cryostat vessel (OCV), as shown in Figure 3.6. The liquid xenon inside the TPC will be kept at a temperature of 175.8 K, whilst the nominal pressure of the gas is 1.8 bar. The temperature inside the chamber is controlled by several thermosyphon heat pipes, acting as heat sinks, that are connected to the xenon system. These thermosyphons are cooled by a reservoir of liquid nitrogen (LN), which is continuously produced in closed cycle by a cryocooler. In addition, four exterior LN storage tanks of 450 litres of capacity, connected to the laboratory by a vacuum-jacketed (VJ) piping system, provide the initial LN volume to start the cryocooler and serve as a backup for high load periods.

The LZ detector incorporates two important additional features: an instrumented LXe skin layer (referred to as the "Xe Skin" detector), and a liquid scintillator outer detector (OD). These two components operate as an integrated veto system that can effectively reject multi-site background events, providing good veto efficiency for both gamma-rays and neutrons.

Firstly, the Xe Skin detector comprises an instrumented layer of LXe located between the TPC and the ICV, containing approximately 2 tonnes of LXe. This region is monitored by 93 Hamamatsu R8520 1-inch PMTs at the top (barrel region), and 38 Hamamatsu R8778 2-inch PMTs at the bottom (barrel and bottom dome). The main goal of the Xe Skin detector is to identify events with scattering vertices in the skin region, especially those originated by gamma-rays or radiative neutron capture on detector materials.

Secondly, the OD surrounds the LZ cryostat and is composed of a set of acrylic tanks containing 17.3 tonnes of gadolinium-loaded liquid scintillator (GdLS) [215, 216]. Scintillation light produced in the OD is detected by 120 Hamamatsu R5912 8-inch PMTs, which are mounted on ladders approximately 1 m away from the acrylic tanks. The region outside the

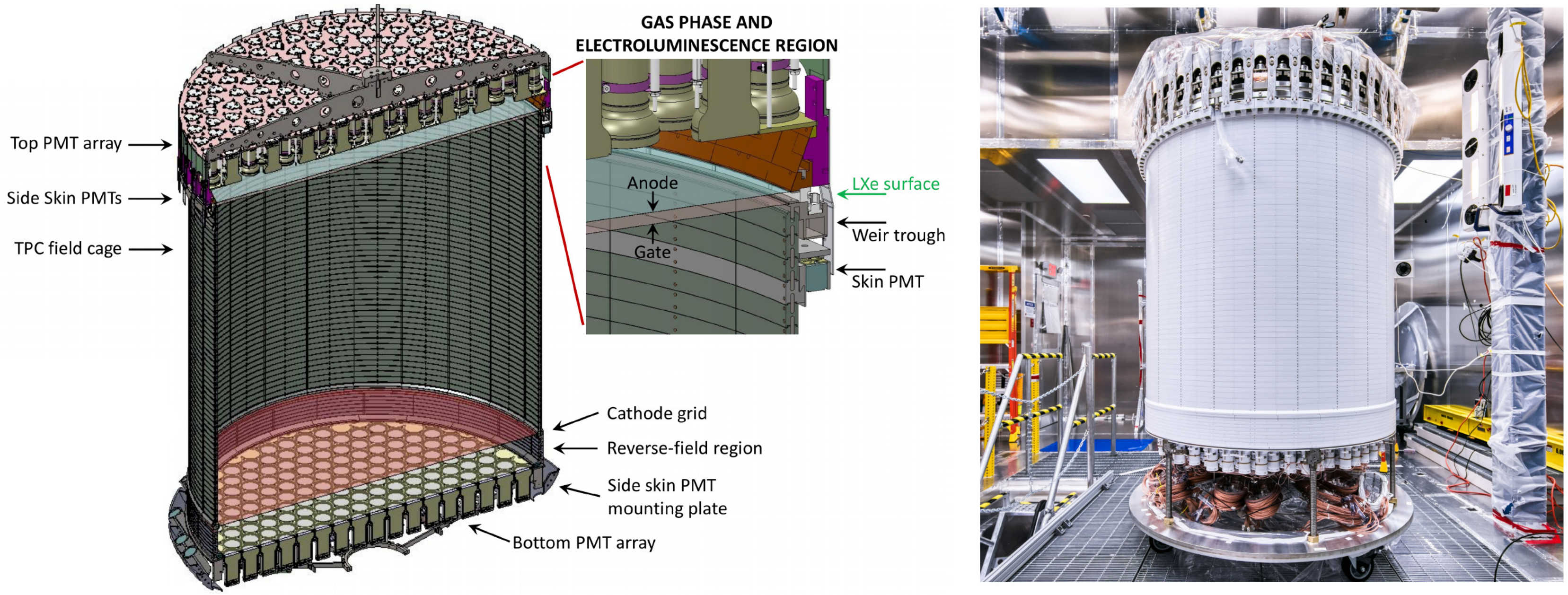

Figure 3.5: Schematic drawing (left) and photo (right) of the LZ Xenon Detector. The cathode and gate electrodes define the 7-tonne active region of the TPC, where both light and charge are emitted after a particle interaction. The field cage is made of successive section of Ti rings embedded in PTFE panels, and it provides a vertical electric field across the active region. S1 and S2 signals are detected by two arrays of photomultipliers (PMT) located at the top and bottom of the TPC. S2 signals are generated in the electroluminescence region between the liquid xenon surface and the anode. The 2-tonne Xe Skin is the region between the outer walls of the TPC and the inner cryostat vessel, and the activity in this region is monitored by an array of side Skin PMTs (depicted), and dome Skin PMT below the bottom PMT array (not depicted). Figure adapted from Ref. [1]. Photo by Matthew Kapust, Sanford Underground Research Facility.

OD tanks is filled with ultra-pure water, which provides extra suppression of backgrounds from radiation of the rock surrounding the cavern. The main goal of the OD is to tag neutrons that emerge from the TPC after having caused a nuclear recoil in the active region. Neutrons are expected to scatter multiple times, but neutron single scatters in the TPC are indistinguishable from a WIMP interaction, posing an important risk to the WIMP search. Any neutron entering the OD will most likely be captured by the gadolinium, releasing approximately 8 MeV in a cascade of gamma rays that will be detected by the PMT in the water tank.

Finally, a comprehensive calibration system has been devised to calibrate the detector with beta, gamma and neutron sources. This is achieved via an automated delivery system of radioactive sources to the vacuum space between the inner and outer vessels, an injection system for dispersible radioisotopes and an external deuterium-deuterium neutron generator.

More information about the different detector systems of the LZ experiment can be found in the Technical Design Report (TDR) [1].

3.3.2 Experimental strategy

Evidence of WIMP dark matter interactions in LZ would come from an excess of single-scatter nuclear recoils occurring inside some analysis-dependent fiducial volume, and with a recoil energy within a predefined region of interest (ROI). For the present work, a fiducial volume with the following characteristics is assumed: 4 cm away from the TPC walls, 2 cm above the cathode and 13 cm below the gate grid, containing a total of 5.6 tonnes of LXe. There is a substantial amount of LXe in the reverse-field region below the cathode, so the cut at the bottom of the TPC can be more aggressive than that below the gate at the top. The lateral cut is motivated by our ability to reconstruct wall events; at 4 cm it is expected that the fraction of interactions occurring at the wall that are misreconstructed into the volume is less than 10^{-6}, ensuring that wall events become a sub-dominant background. In addition, a total science run of 1000 live days will be considered.

A summary of the nominal values that are considered for some key detector parameters of the LZ experiment is provided in Table 3.2. After an interaction occurs in the TPC, the prompt scintillation light is propagated to the PMTs and an S1 signal is recorded. The S1 raw signal is corrected for variations of light collection with the x-y position, turning it into an $S1_c$ signal that matches the S1 response in the centre of the active region. The connection between the S1 signal and the number of photons emitted at the interaction site is provided by the g_1 factor, as we saw in Section 3.2.2. The g_1 factor is formally defined as the photon detection efficiency (PDE) in the liquid times the average quantum efficiency of the PMTs. A nominal value of

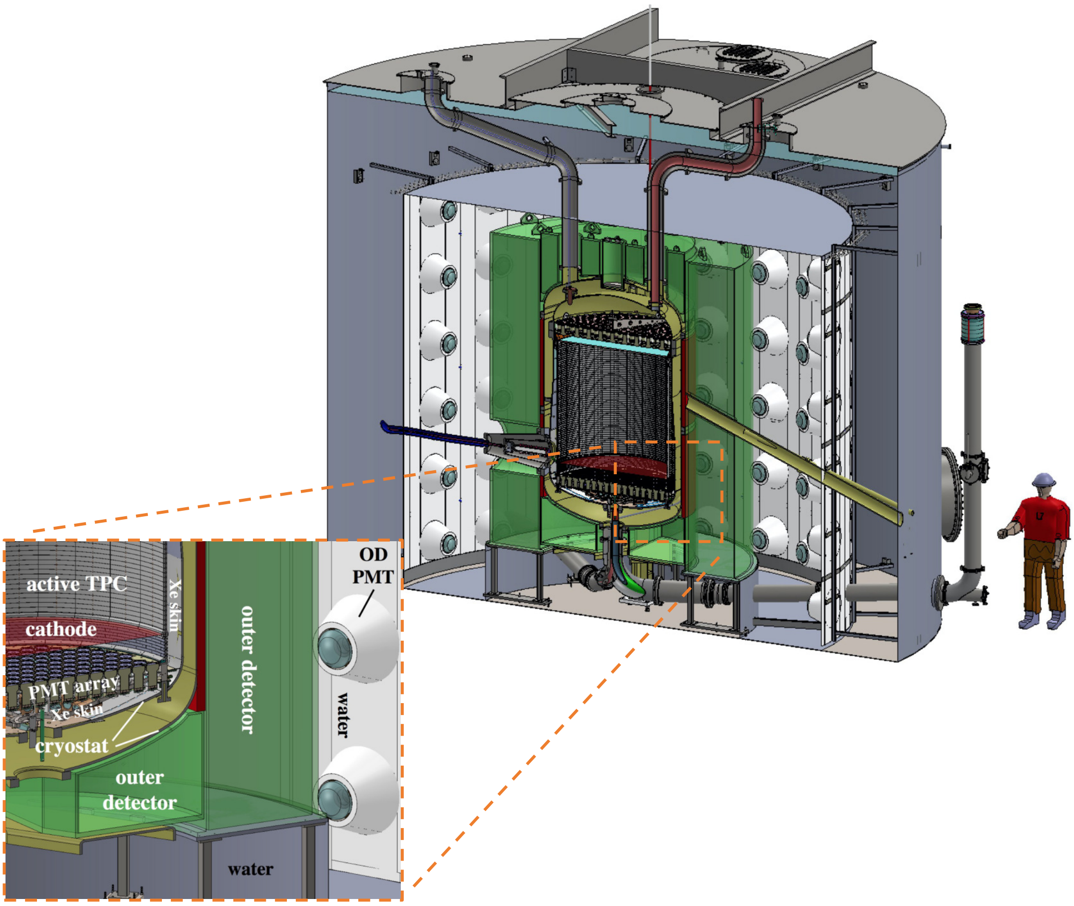

Figure 3.6: Schematic drawing of the LZ detector systems. The LXe TPC is located inside an ultra-pure titanium cryostat. It is surrounded by the outer detector (OD) tanks, in green, and placed in a large water tank, in grey. PMTs are installed inside the water tank to detect light emitted from neutrons captured in the OD. Several conduits penetrate the water tank and the OD: PMT and instrumentation cables (top and bottom), cathode high voltage (middle left) and neutron beam conduit (middle right). *Zoom-in:* Enlarged view of the lower right corner of the detector. The active TPC region is monitored by top and bottom PMT arrays, while an additional collection of PMTs installed around the inner vessel are used to monitor the Xe Skin. Figure adapted from Ref. [2].

Table 3.2: Nominal values of key parameters of the LZ experiment. PDE stands for "photon detection efficiency" and SE for "single electron", while phd refers to units of "photons detected".

Detector parameter	Value
Duration of science run [live days]	1000
Fiducial volume [kg]	5600
Drift electric field [V/cm]	310
Electron lifetime [µs]	850
Electron extraction efficiency	95%
PDE in GXe ($g_{1\text{gas}}$)	0.10
Average SE size [phd]	83
g_1 factor [phd/γ]	0.12
g_2 factor [phd/e^-]	79.2
S1 coincidence level	3-fold
PTFE reflectivity in LXe	97.3%
PTFE reflectivity in GXe	85%

0.12 phd/γ is adopted based on extensive optical simulations and measurements of optical properties of both PMTs and detector components [1].

In addition, a 3-fold S1 coincidence level is considered, meaning that any event that does not trigger the response of at least 3 PMTs will be rejected. Enforcing a 3-fold PMT coincidence level reduces drastically the probability that accidental coincidences between multiple PMT dark counts trigger a fake S1-only signal; less than 0.2 counts are expected in LZ for its total exposure where the fake S1-only signal pairs up with an S2-only signal to create a plausible event. A 2-fold requirement was used in the standard LUX analyses (see for instance, Ref. [185]), since the experiment had smaller and fewer PMTs.

Conversely, the S2 signal is produced from the ionisation electrons that escape recombination and drift vertically through the LXe to the gas phase. A spatial correction to the S2 signal is applied to account for the finite electron lifetime inside the TPC due to the presence of electronegative impurities dissolved in the LXe. Thus, the S2 raw signal is corrected into S2$_c$ to match the S2 response at a central position just below the electron extraction region. The S2 signal is always large, and remarkably enough, this secondary scintillation signal is sensitive to single electrons extracted from the liquid. The projected value for the average size of the single electron (SE) response in LZ is 83 phd; a signal that would certainly be recorded by the top PMT array. The SE size depends mainly on the extraction field, the gas pressure and the photon detection efficiency in the gas, $g_{1\text{gas}}$, with the latter having an estimated value of 0.10.

The conversion between S2 and the number of free electrons is controlled by the g_2 factor, as shown in Eq. (3.27). g_2 is defined as the electron extraction efficiency at the interface between the liquid and gas times the average size of the SE response. A value of 79.2 [phd/e^-] is adopted (for an electron extraction efficiency of 95%).

The majority of detector parameters highlighted above have been estimated using full simulations of particle interactions in the detector volume. This is mainly achieved with the simulations framework `BACCARAT`, which is built on the GEANT4 toolkit [217]. In addition, the NEST package is used to calculate the number of electrons and photons produced in the LXe in response to either ER or NR events. Then, a parametrisation of the detector response, based on the full simulations using `BACCARAT`, is applied to convert the number of emitted photons and electrons into $S1_c$ and $S2_c$ signals (in units of phd). This process allows for fast generation of ($S1_c$,$S2_c$) probability density functions (PDF) for a given set of detector parameters, including the S1 coincidence requirement, g_1 factor, drift field, etc.

The region of interested (ROI) for the WIMP-search analysis is defined by the $S1_c$ window $0 < S1_c < 80$ phd, and assuming a 3-fold S1 coincidence level. Note that the S1 signal can be lower than 3 phd as long as the 3-fold requirement is fulfilled. In addition, the S2 raw signal is required to be over 420 phd ($\sim$5 extracted electrons) to ensure an accurate x-y position reconstruction. The effect of the ROI cuts is summarised in Figure 3.7, where the simulated detection efficiencies for single scatter events in the TPC are shown as a function of electron (left) and nuclear (right) recoil energy. The shape of the lower end of these curves is mainly determined by the 3-fold condition, while the upper cut on $S1_c$ affects the end tail. It should be emphasised that these cuts are preliminary and they might change in future analyses of real data. Also, extending the energy window could lead to a better measurement of some dark matter properties, as noted for instance in Ref. [218].

The NR efficiency goes below 50% at an energy of 4 keV, which is considerably larger than the energy cut of 0.3 keV adopted in the previous section due to the uncertainty on the yields, and highlighted in these plots in grey. Furthermore, these detection efficiencies are slightly different to the ones that were shown in the LZ WIMP sensitivity paper [2], especially the lower end of the ER efficiency curve. The main reason for this difference lies on the different version of the NEST package that was used: the work in this thesis is based on NEST `v2.0.0`, while a previous version of NEST called libNEST `5.0.0` was employed in Ref. [2]. A comparison of the prediction of the LXe yields between these two versions of NEST is shown in Figure 3.8, which shows a noticeable difference in their predictions of the ER scintillation yield at low energies; the light yields from the newer prediction goes faster to zero.

In addition, events in the active region with a time-coincident signal in either the Xe Skin or the Outer Detector are rejected. For the Xe Skin, an event is rejected if a signal of at least 3 phd is detected by the Skin PMTs within an 800 μs coincidence window with the S1 signal

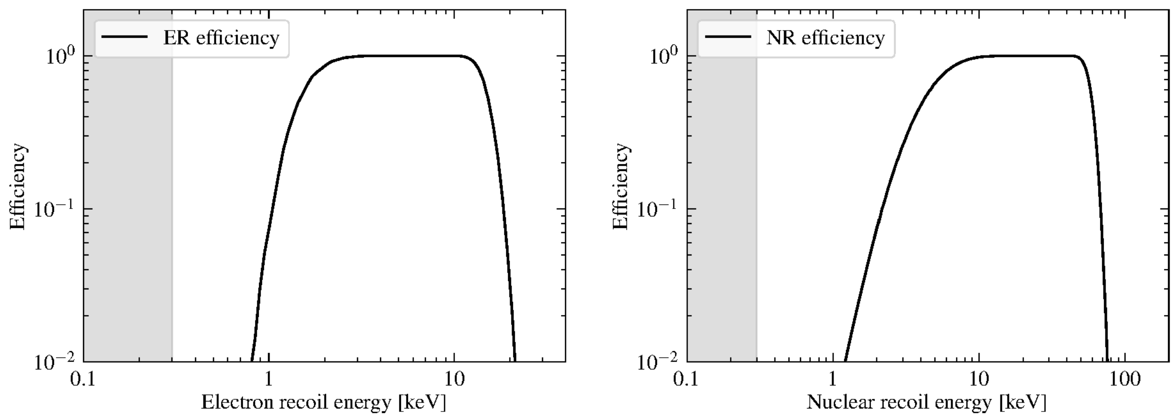

Figure 3.7: Simulated detection efficiency of ER (left) and NR (right) events after region of interest cuts: 3-fold S1 coincidence, $S1_c$ <80 phd and S2 > 420 phd ($\sim$ 5 extracted electrons). In addition, a cut on recoil energy at 0.3 keV is adopted, below which no experimental data are available. This region is highlighted in grey, and it is noticeably distant from the lower end of the two efficiency curves.

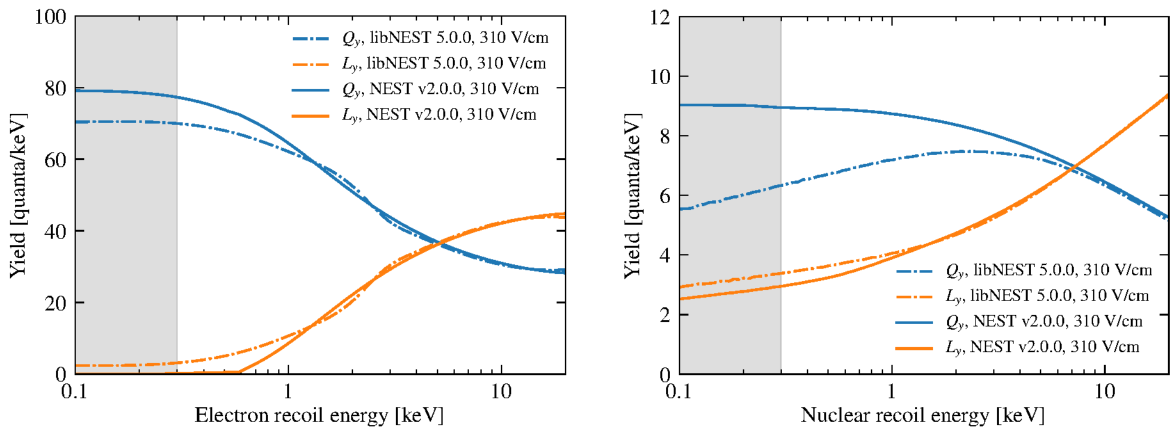

Figure 3.8: Comparison of the prediction of the LXe ER (left) and NR (right) yields between two versions of the NEST package: libNEST `5.0.0` (dot-dashed, older) and NEST `v2.0.0` (solid, newer). The charge and light yields are shown in blue and orange, respectively. The lowest region below which there is no experimental data available is highlighted in grey (see discussion in Section 3.2.1).

in the active region. For the OD, an event depositing an energy greater than 200 keV within 500 μs from a signal in the active region will also be rejected. These time intervals ensure an optimal identification of both scattered gamma-rays and thermal neutron capture.

As previously mentioned, one key aspect for the success of a dual-phase LXe experiment is its ability to discriminate ER events. In order to estimate the ER discrimination level in LZ, we simulate events in the fiducial volume passing the ROI cuts based on two important calibration sources: CH_3T for ER events, and a deuterium-deuterium (D-D) neutron source for NR events (see e.g. Ref. [198, 201] for more information about these calibration sources). The maximum recoil energy produced in liquid xenon by theses sources is approximately 18 keV_{ee} and 74 keV_{nr}, respectively. The top panel of Figure 3.9 shows the corresponding distribution of ER events in the $S1_c$-$\log_{10}(S2_c)$ plane. In addition, the blue and red curves indicate the median, 10% and 90% quantiles of the ER and NR population, respectively. They define the "ER band" and the "NR band", which will be used to calculate the ER discrimination level. In addition, isocontour lines in NR-equivalent (keV_{nr}) and ER-equivalent (keV_{ee}) energy units are shown in light grey. They are calculated using the previously defined energy formula from Eq. (3.28).

We can estimate the ER discrimination level by considering the *leakage* of simulated CH_3T events below the median of the NR band. This is shown in the lower panel in Figure 3.9, where events have been binned in slices of $S1_c$ that are 3 phd wide. The good discrimination observed up to $\sim$20 phd is mainly attributed to a decrease of the electron-ion recombination process at very low energies, as described earlier, which leads to a moderate separation of the bands. The dashed line in this plot shows the weighted average for the ER leakage, with a value of 0.002, or equivalently, 99.8% ER discrimination. This value is in good agreement with the average discrimination level achieved by previous experiments, ranging from 99.5% in XENON10 [219] to 99.99% in ZEPLIN-III [220]. The discrimination achieved by LUX in Run 3 as a function of $S1_c$ is also shown in Figure 3.9, with an average discrimination of 99.8%.

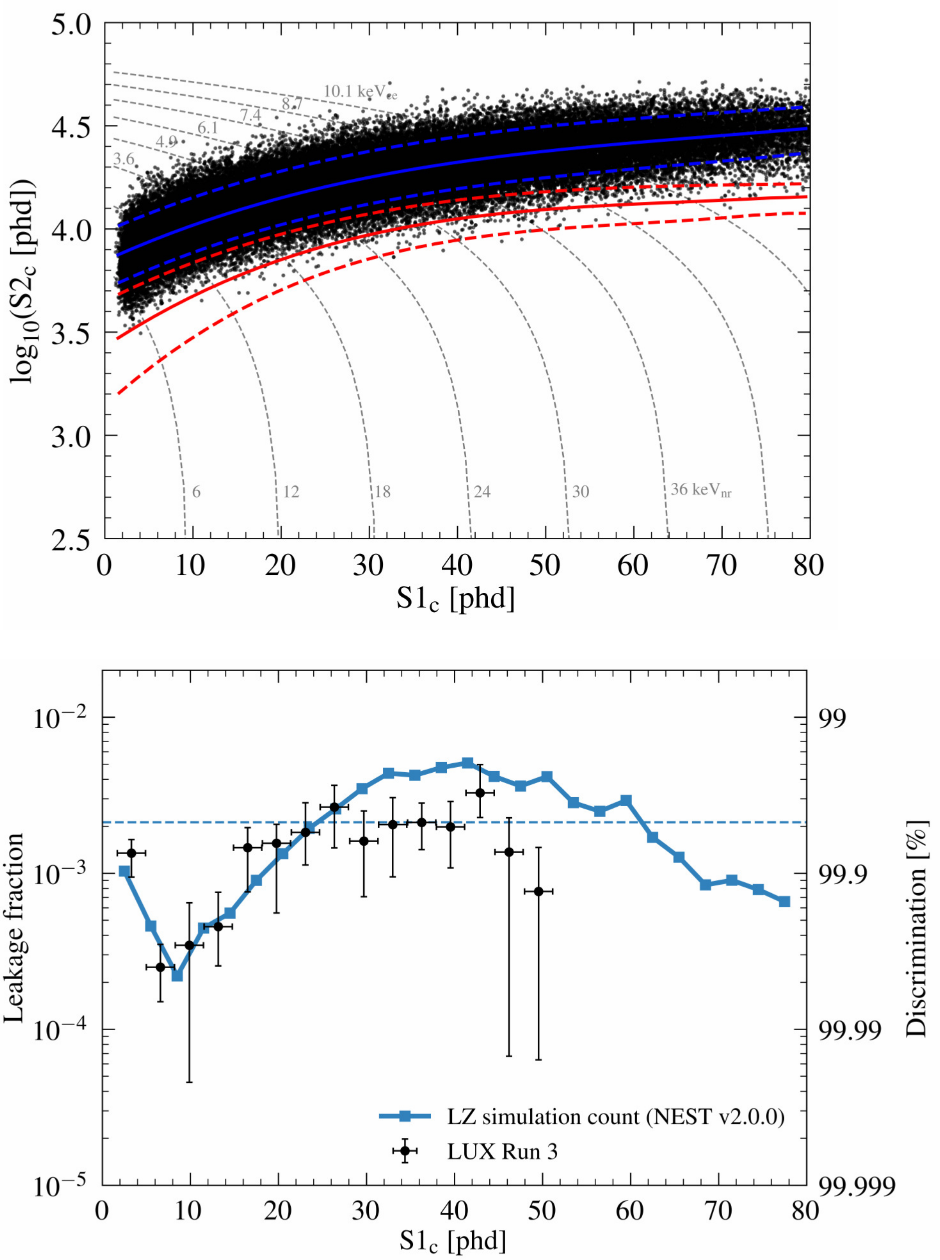

Figure 3.9: *Above:* Simulated ER calibration of the LZ detector response in the fiducial volume. Recoil events from a CH_3T calibration source are generated using a simulation of the detector response based on the parameters listed in Table 3.2 (black dots). The median, 10% and 90% quantiles are shown in solid and dashed blue lines, respectively, which defines the ER band. Only a fraction of the total number of simulated events are shown for clarity. Similarly, the NR band (in red) is obtained with simulated monoenergetic neutrons from a D-D source. The ER leakage is defined as the fraction of ER events below the mean of the NR band. Isocontour energy lines are added (dashed grey), and the energy is expressed in units of both NR-equivalent energy (keV$_{nr}$) and ER-equivalent energy (keV$_{ee}$). *Below:* Leakage fraction (left axis) and ER discrimination (right axis) as a function of S1$_c$. The leakage is calculated in slices of 3 phd in S1$_c$. The dashed line shows the average discrimination, with a value of 99.8%. The ER discrimination from LUX Run 3 data is also shown [208].

3.4 Dominant backgrounds

In this section we outline the main background components in the LZ WIMP search in its expected full exposure of 1000 days and 5.6 tonnes of fiducial mass. The most relevant background components are listed in Table 3.3, along with the expected number of ER and NR counts from each of them. The ROI presented in the previous section will be used in the next chapter when we introduce the Profile Likelihood Ratio (PLR) analysis, which we use to calculate the WIMP sensitivity of the LZ experiment. In this section we consider a more aggressive ROI to calculate the estimated counts that are shown in Table 3.3, for which a cut-and-count analysis is used instead. In particular, the lower and upper bounds of 6 and 30 keV NR energy, respectively, are adopted (equivalent to 1.1 and 6.1 keV ER energy), which correspond to an energy region relevant for a $40\,\mathrm{GeV/c^2}$ WIMP signal. A similar table is presented in the LZ WIMP sensitivity paper [2], and any difference between that table and the one presented here is mainly due to the upgrade of the NEST package from libNEST `5.0.0` to NEST `v2.0.0` [203].

The first entry in the table is *Detector components*. LZ has undertaken a comprehensive screening campaign (>1000 assays over 5 years) to radio-assay all the detector materials. This strict quality control matched with the power of self-shielding provided by LXe is the main reason of why radioactivity from detector materials is not one of the leading backgrounds in Table 3.3. Radioactivity can also arise from *Surface contamination* as a result of the plate-out of ^{222}Rn progeny during the manufacture and assembly of the detector. They lead to neutron production from (α,n) processes, and can create many events near the walls of the detector. These wall events are mostly rejected by the fiducial cut. Furthermore, dust is an intrinsic source of contamination and a source of radon emanation. A rigorous cleanliness programme that includes extensive use of witness coupons, tape-lift sampling and UV inspection has been in place throughout the assembly of the detector to keep the levels of dust to minimum. In addition, the detector is being assembled in better than class 1000 cleanroom conditions at SURF.

Some *Environmental backgrounds* are also important to the WIMP analysis. For instance, the production of radioactive isotopes arising from a prior exposure to cosmic rays, a process known as "cosmogenic activations". In particular, ^{127}Xe ($T_{1/2} = 36.4$ days) from the activation of xenon [221], or ^{46}Sc ($T_{1/2} = 83.8$ days) from the activation of the titanium used for the construction of the detector [2]. The expected counts from these background components are shown in Table 3.3 as "Environmental". Also, the summed energy spectra of the previous three background components (labelled as "Det.+Sur.+Env.") are shown in Figure 3.10 for ER interactions and Figure 3.11 for NR interactions.

A small fraction of *Dispersed radioisotopes* is still expected to be found in the LXe. The most important ones are ^{222}Rn, ^{220}Rn, ^{85}Kr and ^{39}Ar, where the last two are beta emitters that can potentially create ER events at any position in the active region. Regarding the first two, they contribute to the WIMP background via the "naked" beta emission from radon decay products. In the ^{222}Rn sub-chain as it decays to ^{214}Bi, a β particle is emitted from ^{214}Pb. Subsequently, ^{214}Bi also undergoes a beta decay into ^{214}Po, which most commonly will be in an excited state and will release a high energy gamma-ray. This signature of the emission of a beta particle in the LXe followed shortly by a highly energetic gamma-ray in the ^{214}Bi-^{214}Po sequence can be easily identified, even if the gamma-ray leaves the active region, where it will be tagged by the Xe Skin or the OD. However, there is a decay mode wherein the ^{214}Po does not emit a gamma-ray, with a branching ratio of 9.2% [222]. As a result, "naked" beta particles can be generated from this sub-dominant decay channel, creating potentially problematic ER events inside the TPC. A similar process exists in the ^{220}Rn$\rightarrow$^{210}Bi chain. Another dispersed source contained in the LXe is the isotope ^{136}Xe, which as mentioned previously, can decay via two-neutrino double beta decay $(2\nu\beta\beta)$.

An extensive purification program is currently in place to remove ^{85}Kr and ^{39}Ar from the Xe down to the level of 0.015 ppt and 0.45 ppb[2] by gas charcoal chromatography [223]. The krypton requirement is extraordinarily ambitious, and a custom gas chromatography system has been installed at SLAC to tackle this challenge. Conversely, the radon background is controlled by the Xe gas recirculation system coupled with an exhaustive radon emanation screening campaign. The projected specific activity for ^{222}Rn emanation from LZ components is 1.53 µBq/kq [1].

The estimated contribution from all these disperse sources is summarised in Table 3.3. As shown, the ER count is dominated by the dispersed radioisotope ^{222}Rn. It is important to point out that the expected counts from ^{222}Rn and ^{85}Kr are subject to some uncertainty; there is a lack of data for radon emanation as a function of temperature for most materials, and it is difficult to estimate the final krypton content in the Xe system, as air leaks or detector outgassing, although unlikely, might re-introduce some krypton into the xenon.

Some irreducible sources of background come from *Astrophysical neutrinos*. They can produce either NR or ER events via coherent elastic neutrino-nucleus scattering (CEνNS) [125] or elastic neutrino-electron scattering [224], respectively. In the first category, we find neutrinos

[2]ppb stands for parts-per-billion (10^{-9}) and ppt for parts-per-trillion (10^{-12}).

Table 3.3: List of the main background contributions to the WIMP search in LZ for its complete exposure of 1000 live days of a 5.6-tonne fiducial mass. The estimated ER and NR counts of each component are given based on a cut-and-count analysis for a ROI of $6 < E_R < 30$ keV in NR energy, relevant for a 40 GeV/c^2 WIMP signal. Counts from the solar ^{8}B and hep neutrinos (marked with *) are shown as reference and they have been omitted from the total count since their expected NR energy is below 6 keV. Two values for the ER discrimination below the NR median are considered: the nominal value assumed in the LZ TDR and an estimate based on the simulated study presented in this chapter. The differences in this table compared to Ref. [2] are due to the upgrade of the NEST package (from libNEST `5.0.0` to NEST `v2.0.0`).

Background component	**ER**	**NR**
Detector components	9	0.07
Surface contamination	40	0.40
Environmental	5	0.06
Dispersed radioisotopes		
▸ ^{222}Rn	700	0
▸ ^{220}Rn	115	0
▸ ^{136}Xe $2\nu\beta\beta$	83	0
▸ ^{85}Kr	30	0
▸ ^{39}Ar	3	0
Astrophysical neutrinos		
▸ Atmospheric	0	0.52
▸ Diffuse supernova (DSN)	0	0.14
▸ Solar (^{8}B + hep)	0	38*
▸ Solar (pp + ^{7}Be + ^{13}N)	221	0
Total	1206	1.2
Total (99.5% ER discrimination, 50% NR acceptance)	6.0	0.6
Total (99.8% ER discrimination, 50% NR acceptance)	2.4	0.6

produced in muon and pion decay in the atmosphere, or in distant supernovae. Both of them constitute an irreducible background for high mass WIMPs [126].

An even more important source of CEνNS events come from neutrinos originated in the solar processes

$$^{8}\mathrm{B} \to {}^{7}\mathrm{Be}^{*} + e^{+} + \nu_{e} \quad (^{8}\mathrm{B}\ \text{neutrinos}) \tag{3.29}$$

$$^{3}\mathrm{He} + p \to {}^{4}\mathrm{He} + e^{+} + \nu_{e} \quad (\text{hep neutrinos}) \tag{3.30}$$

Figure 3.11 shows the corresponding recoil energy spectra. The ^{8}B and hep rates are only relevant for NR energies below $\sim$ 5 keV. Consequently, these two background components are not important in searches for WIMPs of mass above $\sim$20 GeV/c^2, and their estimated counts have been omitted from the total count in Table 3.3. However, these backgrounds are very important for low mass WIMP searches since ^{8}B scatters can mimic a WIMP signal of a mass around 6 GeV/c^2 [126]. In addition, it constitutes an interesting neutrino signal that LZ will be able to study—and hopefully detect for the first time.

The elastic scattering of solar neutrinos from the *pp* solar chain [225] will constitute an ER background for the WIMP search. Their expected contribution is shown in Table 3.3 under the name of "*pp* + ^{7}Be + ^{13}N". Note that the addition of nuclear binding effects to the calculation of the expected recoil rate [226] has resulted in a small suppression of the estimated count from the value shown in the LZ WIMP sensitivity article [2]. The expected recoil energy spectra for all the neutrinos sources is shown in Figure 3.10 and Figure 3.11.

The total expected count in Table 3.3 in the full LZ exposure is equal to 1206 ER and 1.19 NR events, respectively. Thus, we can give a figure of merit for the total number of background counts that are expected in the region of interested for the search of a 40 GeV/c^2 WIMP signal. Assuming a conservative ER discrimination of 99.5% below the NR median, which is the value that was considered in the LZ TDR, we obtain a total expected count in the region of interest of 6.60 counts. Instead, if a 99.8% ER discrimination level is considered, motivated by the discussion from the previous chapter, a total expected count of 3 is obtained. Both of these numbers are a remarkably low background prediction for an experiment as large as LZ and with such low energy threshold.

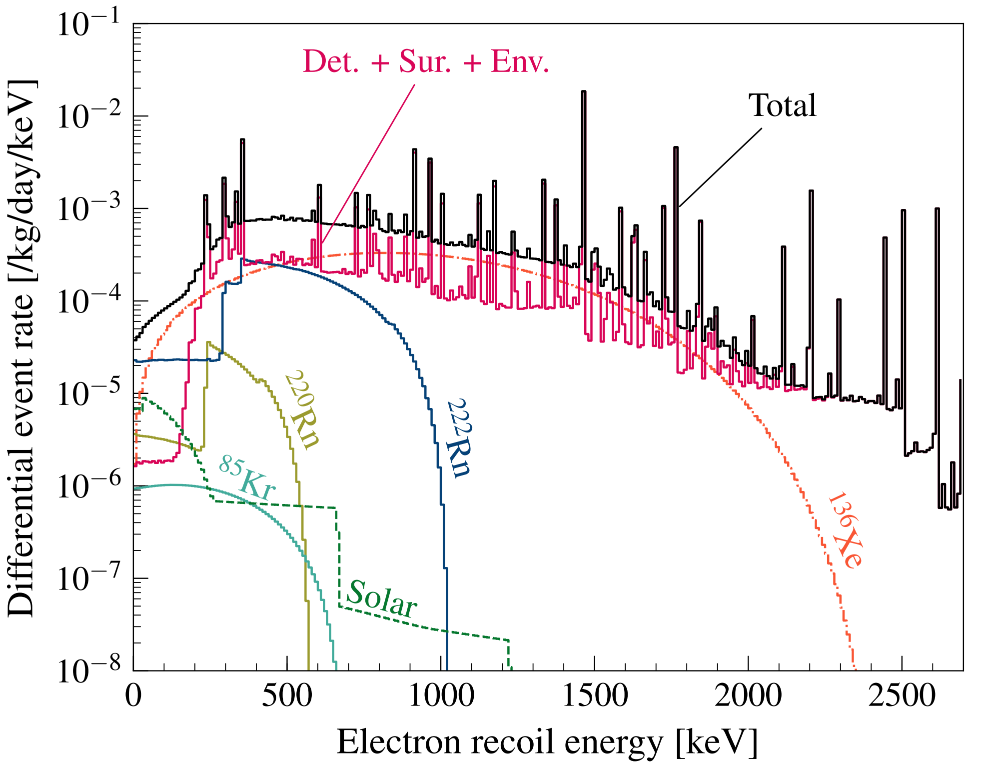

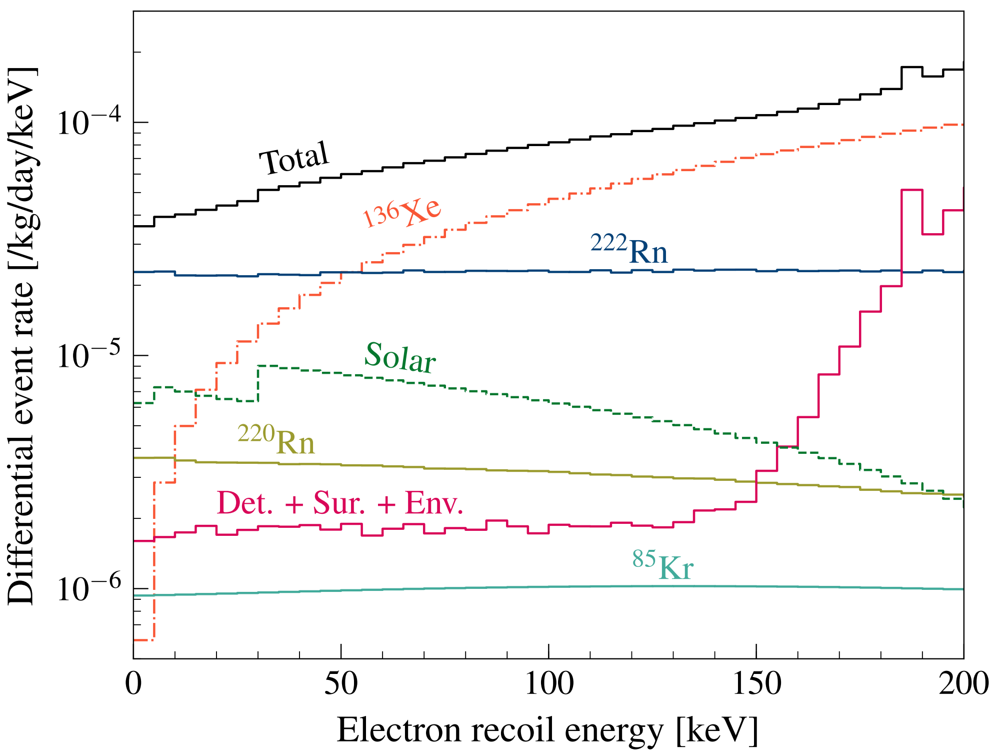

Figure 3.10: *Above:* ER spectra of the most relevant background sources in the 5.6 tonne fiducial volume for single scatter events. Neither the xenon skin nor the OD vetoes are considered, and no ROI cuts are applied. *Below:* Zoomed in version of the above plot for the 0–200 keV region. ER events originated from naked beta emission from radon decay products dominate at low energies (labelled as ^{222}Rn). Figure adapted from Ref. [2].

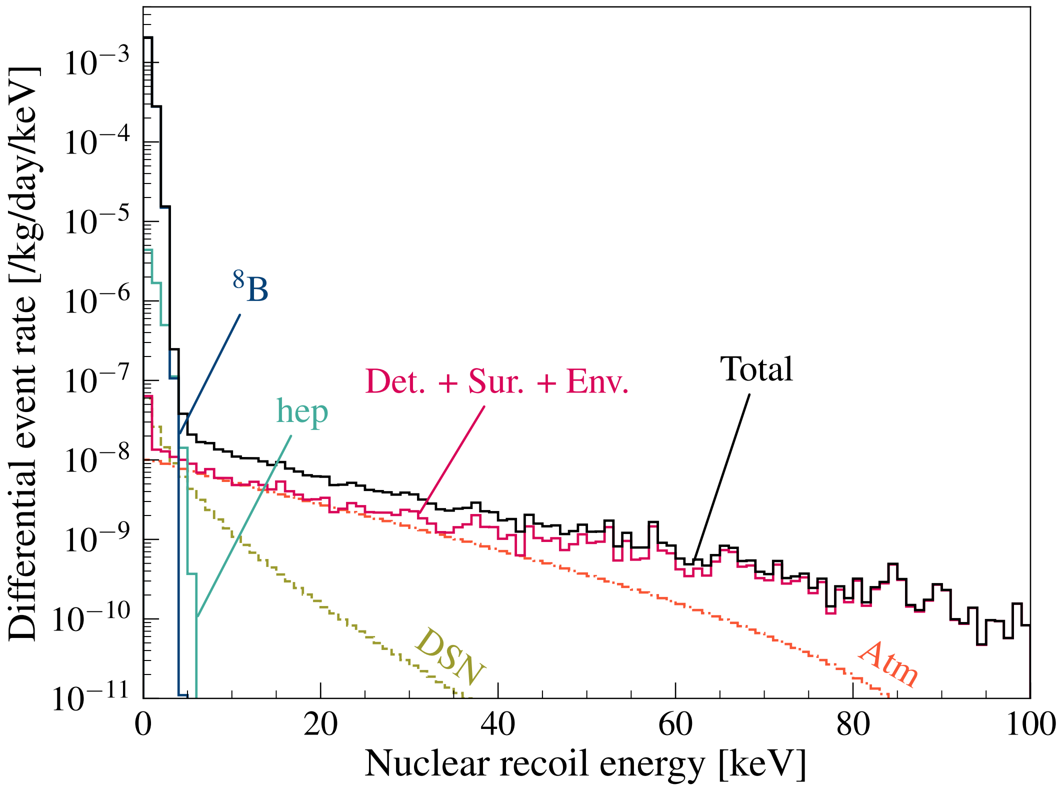

Figure 3.11: NR spectra of the most relevant background sources in the 5.6 tonne fiducial volume for single scatter events. No ROI cuts, or OD and Skin veto cuts, are considered. The ^{8}B neutrino signal dominates at low energies, while atmospheric neutrinos and "Det.+Sur.+Env." dominate at higher energies. Figure adapted from Ref. [2].

Chapter 4

Projected WIMP sensitivity of the LZ experiment

At the time of writing, LZ is on track to start operations in 2020. Extensive work has been conducted during the design and construction phases to understand in detail the response of the LZ experiment to particle interactions, and assess its sensitivity to different types of signals. This chapter focus on the WIMP search, and it describes the statistical methodology that was followed to calculate the sensitivity of the LZ experiment to WIMP dark matter, which was published in Ref. [2].

After introducing some useful terminology, the statistical software package `LZStats` is presented, which is a key contribution of my own to the LZ collaboration. This software package has become a general tool used across the collaboration to standardise statistical analyses, and its main properties will be outlined in this chapter. The LZ projections to the vanilla SI and SD WIMP-nucleon scattering cross sections are presented at the end.

4.1 Statistical terminology

We begin by describing the statistical notation and terminology that will be used throughout this thesis, which is based on the methodology developed in Ref. [227, 228]. Any claim about the discovery of a sought-after signal is primally based on the outcome of an *experiment*. Such an experiment, which may be real or computationally simulated, is a particular realisation of the set of all possible experimental outcomes that constitute the *statistical ensemble*. Certain selection criteria might be applied to the experimental data, which will result in a number of selected *events*. Each of these events will be parametrised with one or several measured quantities, known as the *observables*, $\boldsymbol{x}_e$.[1] For instance, the vector of observables could be the pair $\boldsymbol{x}_e = (\mathrm{S1_c}, \mathrm{S2_c})$, following the definitions of these two quantities from the previous chapter. We will explore this idea further in Section 4.4.

The probability of obtaining a particular event is given by the *event probability model*, which is most generally expressed as a parametric family of probability density functions (PDF),

$$f(\boldsymbol{x}_e|\boldsymbol{\theta}). \tag{4.1}$$

The symbol $\boldsymbol{\theta}$ will be used to refer to the *model parameters*, which are parameters that are intrinsic to the model and can be estimated from data. In general, Greek letters will be used for model parameters, whereas Roman letters will represent observables. The complete set of model parameters is traditionally divided into two categories: firstly, the *parameters of interest* (POI), $\boldsymbol{\alpha}$, which are the parameters that we are interested in measuring because they are part of the physical theory that we are proving; secondly, the *nuisance parameters* (NP), $\boldsymbol{\nu}$, which account for unknown experimental properties or uncertainties of the physical theory that have no intrinsic interest, but are nonetheless needed to build a more accurate model.

The event probability model typically contains a signal component and a handful of background components. Each of them has an associated PDF, $f_j(\boldsymbol{x}_e|\boldsymbol{\theta})$, and an expected mean, $\mu_j(\boldsymbol{\theta})$, with the latter accounting for the specific weight of this component in the total PDF. The dependence on $\boldsymbol{\theta}$ has been made explicit to emphasise that model parameters could affect both the shape of the PDF and its expected mean. Assuming that our total model PDF has N components, and that all the individual means $\mu_j(\boldsymbol{\theta})$ add up to the total mean $\mu(\boldsymbol{\theta})$, then the event probability model can be written as the weigthed sum

$$f(\boldsymbol{x}_e|\boldsymbol{\theta}) = \sum_{j=1}^{N} \left(\frac{\mu_j(\boldsymbol{\theta})}{\mu(\boldsymbol{\theta})}\right) f_j(\boldsymbol{x}_e|\boldsymbol{\theta}). \tag{4.2}$$

Furthermore, and assuming that all events are independent of each other, the PDF for a collection of n_0 events, i.e. the *data set* $\mathscr{D} = \{\boldsymbol{x}_e\}_{e=1}^{n_0}$, will be simply the product of the individual probability distributions of each event. Moreover, and given that most of the experiments in direct dark matter searches have a Poissonian nature, a general Poisson term should be added to account for the fact that the total number of observed events, n_0, is expected to fluctuate around the total Poisson mean, $\mu(\boldsymbol{\theta}) = \sum_{j=1}^{N} \mu_j(\boldsymbol{\theta})$, for multiple realisations of the

[1] Henceforth, boldface will be used to indicate vectors.

experiment. Hence, the *total probability model* for a given data set with n_0 events is given by

$$\begin{aligned} f(\mathscr{D}|\boldsymbol{\theta}) &= \mathrm{Pois}\,(n_0|\mu(\boldsymbol{\theta}))\prod_{e=1}^{n_0} f(\boldsymbol{x}_e|\boldsymbol{\theta}) \\ &= \left(\frac{\mu(\boldsymbol{\theta})^{n_0}}{n_0!}e^{-\mu(\boldsymbol{\theta})}\right)\prod_{e=1}^{n_0} f(\boldsymbol{x}_e|\boldsymbol{\theta}) \end{aligned} \tag{4.3}$$

It is also possible to add constraints to some of the nuisance parameters using the so-called *global observables*, $\boldsymbol{g}_p$. These are observables that come from an auxiliary measurements, and they always keep the same value in the total event probability regardless of the input data set $\mathscr{D}$ (hence the name "global"). The global observables are usually linked to a specific nuisance parameter, ν_p, and they should not be confused with the event observables, $\boldsymbol{x}_e$.

Rather than a detailed probability model for each of the nuisance parameters, one usually has to rely on an approximated guess for its value, and possibly its associated uncertainty too. Following a distinctly frequentist notation, we will add auxiliary probability density functions of the form $f_p(\boldsymbol{g}_p|\nu_p)$ into the total PDF, and use them as *constraining functions* for each nuisance parameter ν_p. Thus, the most general probability model, for a given data set $\mathscr{D}$ with n_0 events and a set of global observables $\mathscr{G}$ for N_c constraining functions, can be expressed as

$$f(\mathscr{D},\mathscr{G}|\boldsymbol{\theta}) = \left[\left(\frac{\mu(\boldsymbol{\theta})^{n_0}}{n_0!}e^{-\mu(\boldsymbol{\theta})}\right)\prod_{e=1}^{n_0} f(\boldsymbol{x}_e|\boldsymbol{\theta})\right]\prod_{p=1}^{N_c} f_p(\boldsymbol{g}_p|\nu_p). \tag{4.4}$$

We conclude this section by introducing the concept of the *likelihood*, $\mathscr{L}(\boldsymbol{\theta})$. The likelihood function is numerically equivalent to the probability model $f(\mathscr{D},\mathscr{G}|\boldsymbol{\theta})$, but has an explicit dependence on the model parameters and it is fixed to a particular observation $\mathscr{D}_{\mathrm{obs}}$, namely,

$$\mathscr{L}(\boldsymbol{\theta}) = f(\mathscr{D}_{\mathrm{obs}},\mathscr{G}|\boldsymbol{\theta}). \tag{4.5}$$

In practice, the likelihood function is used to find the values of the model parameters that maximise the probability of obtaining the observed data set and, therefore, it is a key element in statistical inference. However, it should be noted that the likelihood function is not a probability density function for $\boldsymbol{\theta}$, and generally it does not normalise to unity.

As a summary, Figure 4.1 shows the main elements that are needed for the construction of the total probability model. Note that most of the elements in this diagram have an underlying dependence on the model parameters.

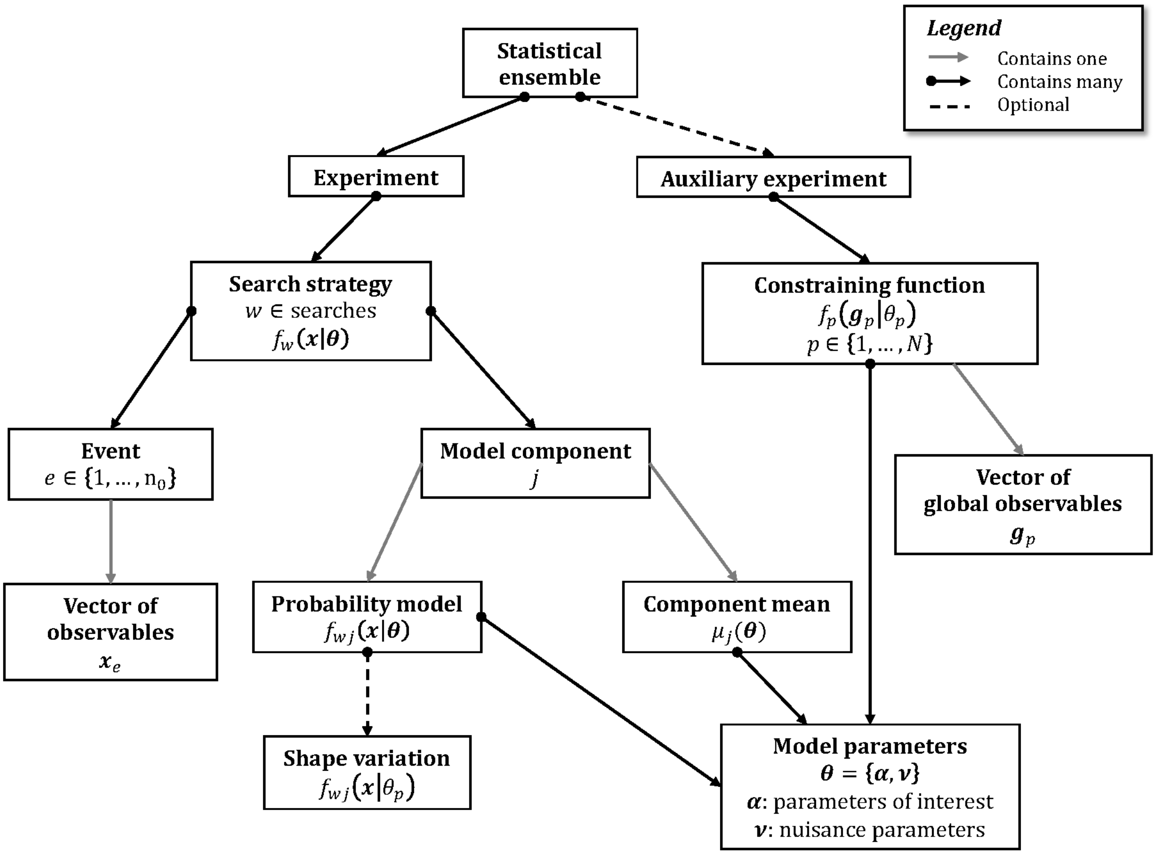

Figure 4.1: Schematic diagram showing all the different elements that are usually contained in the total probability model of a typical direct dark matter analysis. Note how most of the elements in the diagram have a dependence on the model parameters. More information about each part is given in the text.

4.2 Hypothesis testing in direct dark matter searches

Hypothesis testing has traditionally been used in direct dark matter searches either to exclude a specific dark matter model or to determine the discovery significance of a particular observation. In a frequentist hypothesis test, two well-defined hypotheses, referred to as the *null* (H_0) and the *alternative* (H_1) hypotheses, are compared to determine which one is more compatible with a given experimental observation. Generally, the null hypothesis is assumed true until proven otherwise. In practice, one will either *reject* or *fail to reject* the null hypothesis, and it should be emphasised that this method cannot be used to *accept* any of the two hypotheses.

For the purpose of discovering a new signal, one usually defines H_0 as describing only background processes, whereas H_1 includes both background and the desired signal processes. Thus, the two possible outcomes after inspecting the experimental data are either to conclude that there is not enough evidence to exclude the null hypothesis, or to reject H_0 in favour of the alternative hypothesis (signal).

Alternatively, when setting limits on the strength of the signal one usually defines H_0 and H_1 in the opposite way, i.e. the null hypothesis becomes the model with signal plus background. The reason for this choice is that in this case we are interested in finding an upper limit on the parameter of interest, above which any value will be regarded as incompatible with the observed data. Hence, the null hypothesis is tested for increasing values of the parameter of interest until a value is found above which the null hypothesis can be excluded *significantly*.[2]

Once the null and alternative hypotheses have been properly specified, a *test statistic* for the statistical analysis is selected. A test statistic, $t(\mathscr{D})$, is simply a scalar function of the data that reduces the data dimensionality to a single value. Each hypothesis has an associated test statistic distribution, namely $f(t|H_0)$ and $f(t|H_1)$, which may be calculated either analytically or numerically (or both). The latter case is more common, especially for complicated likelihood functions. This is usually achieved by employing Monte Carlo techniques to generate simulated data sets, or *pseudo-experiments*, under the conditions imposed by each hypothesis. Also, one has to evaluate the test statistic on the observed experimental data, and henceforth this will be referred to as t_{obs}.

Once we have all the above ingredients, we can make the hypothesis test more quantifiable. For a pre-defined *size* α of the test, typically 5% or 10%, a *critical region* w is defined such that if t_{obs} falls within this region, the null hypothesis will be rejected with a *confidence level* of

[2] A more quantitative definition for when a hypothesis can be excluded significantly is given at the end of this section.

$CL = (1-\alpha)\%$. Thus, the size of the test is formally defined as

$$P(t \in w|H_0) \leq \alpha, \tag{4.6}$$

where the inequality applies for the case in which the test statistic is a discrete variable. Figure 4.2 shows an example of two arbitrary test statistic distributions, with the boundary of the critical region indicated by the dashed black line. Moreover, and following the notation in that figure, the *power* of the test is $(1-\beta)$, which is defined as the probability of correctly rejecting H_0. In general, the larger the power of a test is, the more separate the two test statistic distributions will be from each other and the more conclusive the test should be.

The null *p-value*, p, is used to assess if enough evidence exists to reject the null hypothesis, and it is defined as

$$\begin{aligned} p &= P(t > t_{\text{obs}}|H_0) \\ &= \int_{t_{\text{obs}}}^{\infty} f(t|H_0)dt \end{aligned} \tag{4.7}$$

In other words, the p-value is the probability of obtaining an experimental result at least as extreme as the observed data if the null hypothesis H_0 were true. Therefore, a low p-value is indicative of a strong disagreement between the observed data and the null hypothesis. It should be emphasised that the p-value is not the same as the size of the test size α, which is a pre-defined quantity. In particular, and as illustrated in Figure 4.2, the two concepts are related in the sense that the null hypothesis H_0 will be rejected with a confidence level $(1-\alpha)\%$ if

$$p \leq \alpha. \tag{4.8}$$

It is common practice in particle physics to report the results of a hypothesis test in terms of the equivalent significance Z. This is defined as the number of standard deviations above the mean of a normal Gaussian distribution such that the upper-tail probability is equal to the p-value.[3] Consequently,

$$Z = \Phi^{-1}(1-p), \tag{4.9}$$

where Φ^{-1} is the inverse of the cumulative distribution of a standard Gaussian. For discovery claims, the convention in the particle physics community—in particular in collider experiments where the "look elsewhere effect" is significant [229]—is that rejecting H_0 with $Z > 3\sigma$ is

[3] Note that some authors have also defined this relation based on a two-sided central interval of a Gaussian distribution. In this case, a 5σ significance corresponds to a p-value of 5.7×10^{-7}, whereas for a single-sided interval the p-value is 2.9×10^{-7}.

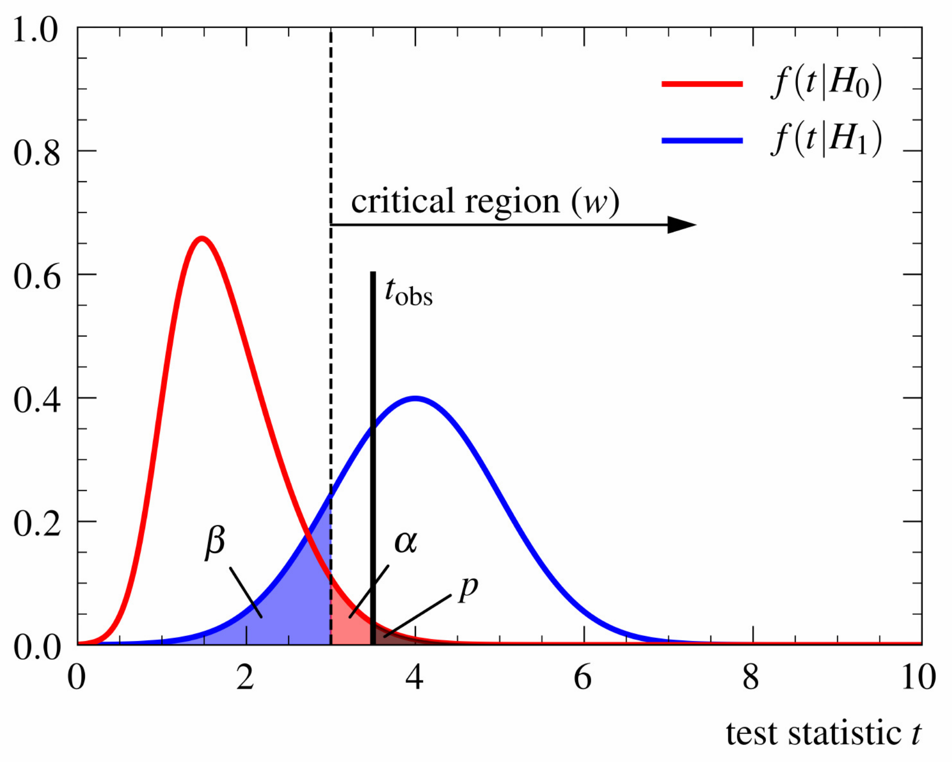

Figure 4.2: Example of two arbitrary test statistic distributions to illustrate the working principle of hypothesis testing. For a given size of the test α, a critical region is defined such that if the observed test statistic falls in this region (i.e. $p < \alpha$), the null hypothesis H_0 will be rejected with a confidence interval $(1-\alpha)\%$. Note that the lower the value of β, the more separated the two distributions will be and hence the test will be more conclusive.

regarded as *evidence*, while $Z > 5\sigma$ constitutes a *discovery*. Alternatively, a 3σ rejection of the null hypothesis would most likely be considered a discovery in direct dark matter searches given the much lower data volume and fewer signal channels compared to collider searches. In addition, exclusion limits are usually reported at a 90% CL in direct dark matter searches, which is equivalent to $Z = 1.28$.

Regarding test statistics, a widely used test statistic is the *profile likelihood ratio* (PLR) [230, 228]. This test statistic not only accounts for the parameters of interest, but for the nuisance parameters too, which are *profiled out* as described below. For a collection of nuisance parameters $\boldsymbol{\nu}$ and a given value of the parameter of interest μ, the profile likelihood ratio is defined as

$$\lambda(\mu) = \frac{\mathscr{L}(\mu, \hat{\hat{\boldsymbol{\nu}}})}{\mathscr{L}(\hat{\mu}, \hat{\boldsymbol{\nu}})} \,. \tag{4.10}$$

The single hat refers to the maximum likelihood estimators (MLE), while the double hat is used to denote the conditional maximum likelihood estimators for a fixed value of μ. Hence, the PLR is the ratio of the conditional likelihood evaluated for a particular test value of μ to the global maximum likelihood. By construction, the parameter $\lambda(\mu)$ is constrained between 0 and 1, and values of λ close to 1 are indicative of a good agreement between the data and the hypothesised value of μ.

Alternatively, one can define

$$t_\mu = -2\log\lambda(\mu), \tag{4.11}$$

which is distributed between 0 and infinity, with larger values of the test statistic corresponding to increasing incompatibility between the data and μ. In the limit of a large data set, $t_\mu = -2\log\lambda(\mu)$ is well-approximated by a chi-square distribution for one degree of freedom, a result known as "Wilks' theorem" [231]. In this *asymptotic limit* of large data samples, the PDF of t_μ under H_0 can be written as

$$f(t_\mu|H_0) = \frac{e^{-t_\mu/2}}{\sqrt{2\pi t_\mu}}\,. \tag{4.12}$$

To quantify the level of disagreement between the observed data and a hypothesised value μ, we use the p-value

$$\begin{aligned} p_\mu &= P(t_\mu \geq t_{\mu,\mathrm{obs}}|\mu) \\ &= \int_{t_{\mathrm{obs}}}^{\infty} f(t_\mu|\mu)dt_\mu \end{aligned} \tag{4.13}$$

where the symbol μ after the vertical bar is used to indicate that the hypothesis that is being tested is that the parameter of interest has a value of μ. It is important to emphasise that when using t_μ as the test statistic, a low p-value may be obtained in two distinct ways: the maximum likelihood estimator for the parameter of interest, $\hat{\mu}$, can be much larger than the test value (i.e. $\hat{\mu} \gg \mu$), or much smaller (i.e. $\hat{\mu} \ll \mu$). In other words, and assuming that μ represents some type of signal strength factor, a particular value of μ is regarded as disfavoured if it predicts a rate that can either be too high or too low to what is observed. Consequently, those values of μ that are rejected because their p-value is found below the size of the test α can be located at either side of the values that are not rejected, resulting in a two-sided confidence interval for μ. For this reason, t_μ is referred to as the *two-sided PLR test statistic*.

For purposes of establishing an upper limit, a value of μ will only be regarded as disfavoured if it predicts a signal rate that is too high compared to what is observed. In this case, one may use instead the test statistic

$$q_\mu = \begin{cases} -2\log\lambda(\mu) & \hat{\mu} \leq \mu \\ 0 & \hat{\mu} > \mu \end{cases} \tag{4.14}$$

where $\lambda(\mu)$ is the profile likelihood ratio defined in (4.10). The caveat to consider here is that one would not use an *overfluctuation* of data to reject a given value of μ, and hence the test statistic is set to 0 when $\hat{\mu} > \mu$. Consequently, a low p-value in this case is only indicative that the test value μ predicts a signal rate that is too high, and therefore only large values of μ will be rejected (i.e. those for which $p_\mu < \alpha$). This test statistic is commonly used to answer the question of how large the parameter of interest can be before it becomes incompatible with the observed data, and it leads to a one-sided interval on μ. It will be labelled henceforth as the *one-sided PLR test statistic for upper limits*.

Similar to the previous case, the test statistic distribution $f(q_\mu|H_0)$ can be approximated by the following asymptotic distribution in the limit of large data sets [228],

$$f(q_\mu|H_0) = \frac{1}{2}\left(\delta(q_\mu) + \frac{e^{-q_\mu/2}}{\sqrt{2\pi q_\mu}}\right), \tag{4.15}$$

which is known as a “half chi-square distribution”.

Alternatively, one may also be interested in testing the value of $\mu = 0$ for the parameter of interest. A rejection of the $\mu = 0$ hypothesis would favour the discovery of a new phenomenon. A test statistic specially designed for this case is

$$q_0 = \begin{cases} -2\log\lambda(0) & \hat{\mu} \geq 0 \\ 0 & \hat{\mu} < 0 \end{cases} \tag{4.16}$$

where $\lambda(0)$ is the profile likelihood ratio evaluated at $\mu = 0$. By using this test statistic, we ensure that a low p-value is only representative of the observation of an excess of events over the expected background (i.e. $p_0 < \alpha$ only if $\hat{\mu} \geq 0$). In such case, we would not regard an *underfluctuation* of data as a sign of incompatibility between the observed data and the background-only model, and hence we set the test statistic to 0 for $\hat{\mu} < 0$. This test statistic will be referred to as the *one-sided PLR test statistic for discovery*.

In the asymptotic limit, the distribution $f(q_0|H_0)$ can also be approximated by a "half chi-square distribution", specifically,

$$f(q_0|H_0) = \frac{1}{2}\left(\delta(q_0) + \frac{e^{-q_0/2}}{\sqrt{2\pi q_0}}\right). \tag{4.17}$$

It is a topic of intense debate within the direct dark matter community which of the one- or two-sided alternatives should be used. On the one hand, one could argue that Eq. (4.16) establishes the appearance of new phenomena in the most decisive manner (at the cost of making virtually no characterisation of the new discovered signal). On the other hand, Eq. (4.14) is the test statistic that best addresses the question of knowing which parameter values are excluded because their predicted rates are too high. This is a desirable feature to have, especially during the "search phase" of an experiment in the absence of a discovery. However, some experiments might have some rather short search phases, and their ability to perform several subsequent analyses might be limited. Consequently, and especially in order to avoid some coverage problems associated with the problem of "flip-flopping"[4] identified by Feldman and Cousins [232], it is recommended that a set of tests are decided prior to looking at the data and that the results from all these tests are reported (including for instance, an upper limit even if enough evidence to claim a discovery exists already).

4.3 LZStats: a statistical software framework for LZ

4.3.1 Description of the code

The LZ collaboration has multiple analysis groups that will be exploring different signal models. It turns out that the methods to calculate a sensitivity projection, or to determine the discovery significance of a given data set, are similar amongst the different groups. In order to standardise the statistical analyses being conducted by these groups, a software framework called `LZStats` has been developed. Such a generic and extensible framework not only facilitates the task of running a statistical analysis, but it also makes each analysis less prone to error.

`LZStats` is written in C++, and it makes strong use of libraries from the ROOT software package [233]. In particular, the `RooFit` toolkit provides classes that facilitate the creation of the likelihood function, and `RooStats` is used to apply multiple statistical methods on the

[4] Flip-flopping is a term used to refer to the fact that the coverage probability of a confidence interval may be different to the nominal value if one decides to carry out either a one- or two-sided test *after* looking at the observed data.

same input model [234]. The code is installed following a prescription dictated by the `LzBuild` configuration system. This is an important step to ensure that the software can run on all the machines that the LZ collaboration relies on. Additionally, the development of new code is done following a strict practice of continuous integration with the Git-repository manager `GitLab`. This ensures that each change in the code that is being uploaded to the official software repository is automatically tested against some benchmark code performance. This makes the development of code more reliable and it avoids compounding problems that are usually more difficult to solve.

The first step in any statistical analysis is to carefully state which question one is trying to answer. In direct dark matter searches, the most relevant questions may be grouped as follows:

- **Projected sensitivity**: given the characteristics of the detector and our best predictions for the background and signal models, how much region of the allowed parameter space can be explored by the experiment (at X% CL)?

- **Exclusion limit**: after an experiment has been conducted, which region of the parameter space is excluded by that observation (at X% CL)?

- **Projected discovery significance**: what is the limit on sensitivity above which one could still claim a discovery with Z-sigma significance?

- **Discovery significance**: how compatible is a given data set with the background-only hypothesis? How statistically significant is this observation?

`LZStats` provides a straightforward procedure to address each of the questions above. The code is run through a submission script that takes the following four arguments:

I. **MASS**: value of the WIMP mass in units of $\mathrm{GeV}/\mathrm{c}^2$, or `-1` if the particle mass is not a relevant parameter.

II. **MODEL**: location of the workspace file[5] with the input model, or `vanilla_wimp` to use the standard WIMP elastic scattering model.

III. **DATA**: location of the input data file, or `sensitivity` to run a sensitivity analysis.

IV. **ANALYSIS TYPE**: 0 = Frequentist (limit-setting), 1 = Frequentist (discovery significance), 2 = Bayesian (either).

[5] RooFit introduces the concept of workspaces via the `RooWorkspace` class, which allows the user to save data and an arbitrarily complicated model to a ROOT file.

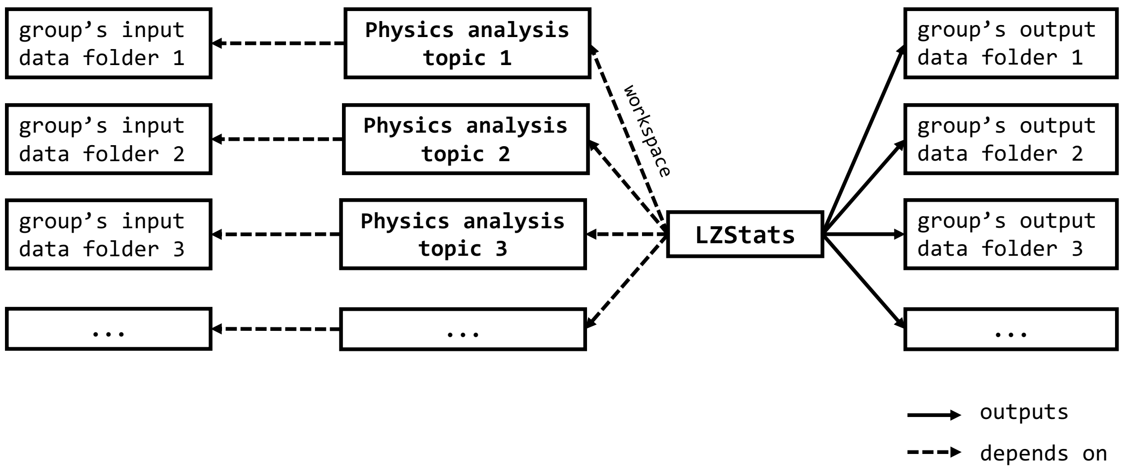

Figure 4.3: A schematic diagram of the data flow when `LZStats` is executed providing a workspace as the second argument in the running script.

The first and second arguments are used in conjunction to completely specify the input model. One possibility is that the user provides the path to a RooWorkspace file in the second argument. This file should be created in advance and it should contain the characteristics of the total probability model that the user is interested in studying. Then, the first argument must be used to specify the mass of the sought-after WIMP particle or be set to `-1` to indicate that the mass of the particle is not a relevant parameter for the analysis.

The general structure for this running mode is illustrated in Figure 4.3. This option offers great versatility since the same type of statistical analysis can be run on any given input model created by each of the LZ Physics Topic groups. Thus, the work of the user is reduced to creating a workspace that contains an accurate description of the background and signal models, and then select the desired settings about the statistical analysis in `LZStats`.

Another possibility is to use the keyword `vanilla_wimp` in the second argument to load a predefined WIMP model that is highly customisable via the `LZStats` configuration file. The creation of the signal and background models is done using functions from a collection of interconnected C++ classes: `ModelTools`, `NestTools`, `StyleTools`, `WimpTools`, and `BackgroundTools`, as shown in Figure 4.4. This diagram shows that the generation of the background PDFs relies on input data from a common repository for each LZ analysis group, which will contain any relevant information about the specific background models.

By contrast, the details for the creation of a signal PDF are adjusted in the configuration file of `LZStats`. In this file the user can specify, amongst others, the astrophysical properties of WIMPs, the properties of the target material, and the type of WIMP-nucleon interaction (e.g. SI

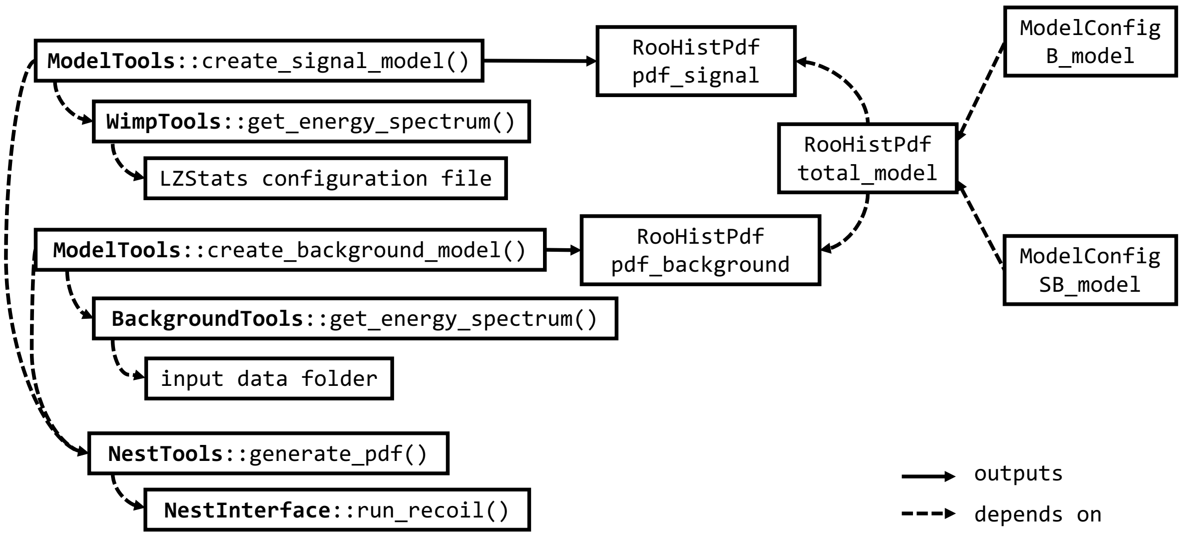

Figure 4.4: Class diagram of the generation of the total probability model when `LZStats` is executed with the keyword `vanilla_wimp` as the second argument in the running script.

or SD). Furthermore, and as shown at the bottom of the diagram, the creation of both signal and background PDFs depends on the class `NestTools`. This contains methods to generate S1 and S2 observables in LZ energy using the NEST software, as described in Section 3.3.2. An additional class called `NestInterface` is used as a handle to configure and run NEST.

4.3.2 Output

In this section we give a short description of the expected output returned by `LZStats` for the different analysis types that are available. Let us consider first running a frequentist *projected sensitivity analysis* considering the vanilla WIMP model. After adjusting the settings in the `LZStats` configuration file, we run the code with the input arguments

```
40 vanilla_wimp sensitivity 0
```

In this case, we are testing increasing values of the parameter of interest for a SI WIMP signal model of mass 40 GeV/c^2. The goal is to find the value of the parameter of interest above which the signal+background hypothesis (`S+B model`) is incompatible with a background-only observation at a 90% confidence level. The signal mean, μ_s, will be considered as the only parameter of interest.

The upper panel of Figure 4.5 shows the corresponding distributions of the one-sided PLR test statistic for upper limits from Eq. (4.14) for 9 values of the parameter of interest signal mean. The hypothesised μ_s goes in increasing values from top left to bottom right. The null distribution (which in this case corresponds to the `S+B model`) is shown in red, while the alternative distribution is in blue. The median of the alternative distribution is taken as a proxy for the observed test statistic (vertical black line), and the asymptotic formula from (4.15) is shown in magenta. A good agreement between the Monte Carlo distributions and the asymptotic formula is observed in this case. It is worth noting that the black vertical line would indicate the position of the observed test statistic, $q_{\mu,\text{obs}}$, if a data file had been provided as the third argument.

The lower panel of Figure 4.5 shows the corresponding p-value, p_μ, for the same 9 hypothesised μ_s values in the plot above. The p-value is calculated using both the Monte Carlo toys (black circles) and the asymptotic formula (magenta diamonds). Moreover, for each value of μ_s that is tested, the null p-value that would be obtained if the median of the alternative distribution were shifted by 1σ or 2σ in either direction is also reported in green and yellow, respectively. These are used as a representative measure of possible statistical fluctuations of the observed upper limit obtained over repeated experiments.

Then, the projected 90% CL upper limit on the parameter of interest, $\mu_s^{90\%}$, is obtained by finding the crossing point between the 10% horizontal p-value line (solid red), and the expected median line (dashed black). In particular, $\mu_s^{90\%}$ is the solution to the equation

$$p(\mu_s^{90\%}) = 10\%, \tag{4.18}$$

and this procedure is usually referred to as "inverting" the hypothesis test.

Alternatively, the keywords `sensitivity` and `1` can be used as the third and fourth argument of the submission script to calculate the *projected discovery significance* of an input signal model. In this case, the null hypothesis becomes the background-only model, and the q_0 test statistic is used. The upper panel of Figure 4.6 shows an example of the corresponding test statistic distributions, with the asymptotic formula from Eq. (4.17) overlapped in magenta. Similarly to the previous example, increasing values of the parameter of interest are considered going from the top left to bottom right. However, in this case the test statistic distribution of the `S+B model` is the one moving towards larger values as the hypothesised POI value increases, implying an increasing disagreement between the toy data (which is generated assuming a signal mean equal to the one that is being considered) and the POI value $\mu_s = 0$ (see definition of the q_0 test statistic in Eq. (4.16)).

The lower panel of Figure 4.6 shows the p-value for the same range of POI values considered in the upper plot. The p-value is calculated as in (4.7) using both the Monte Carlo

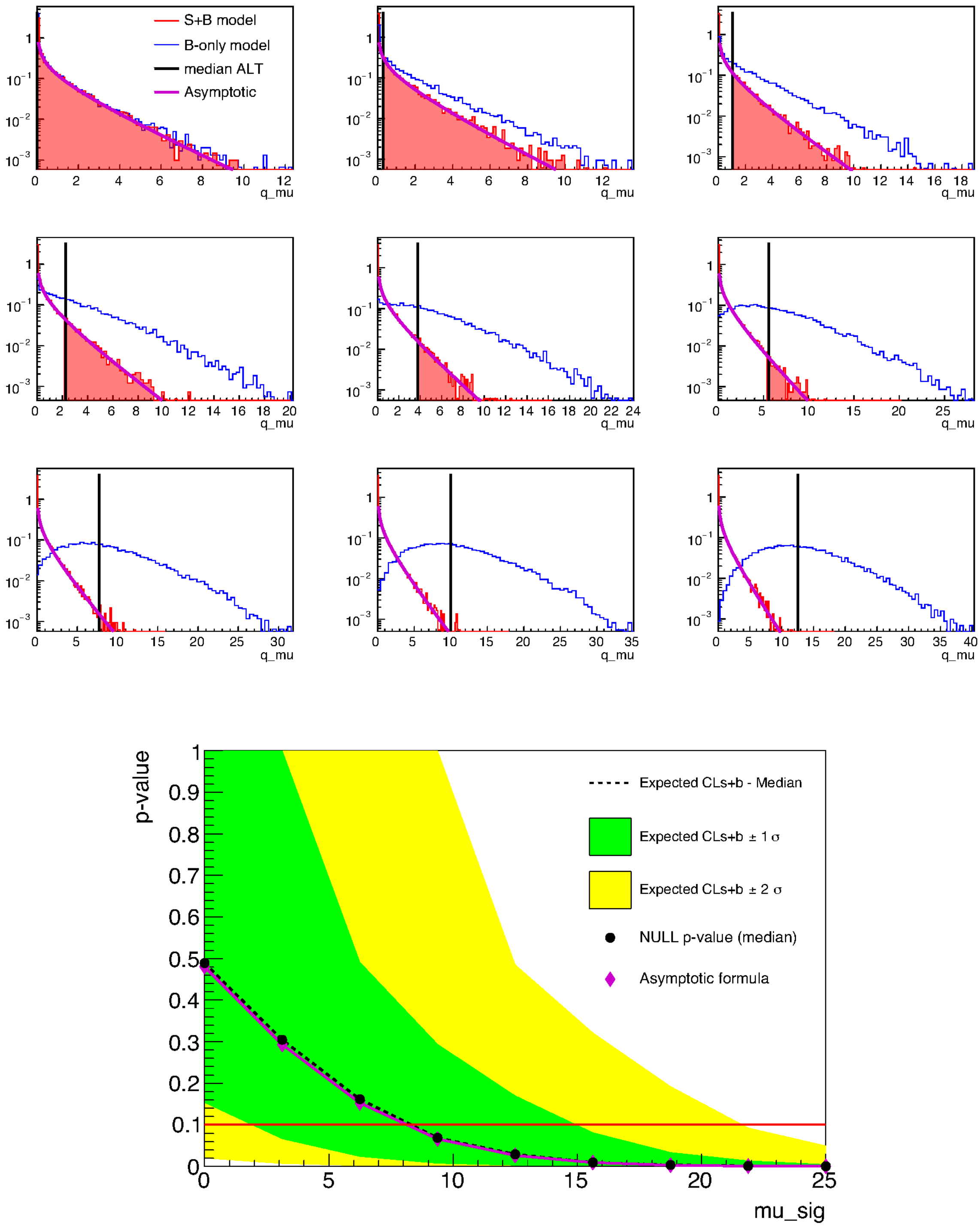

Figure 4.5: `LZStats` output from a projected sensitivity analysis. *Above:* Test statistic distributions under the null (signal plus background, in red) and alternative hypotheses (background-only, in blue). The one-sided PLR test statistic for upper limits is used (Eq. (4.14)). The vertical black line indicates the median of the alternative distribution. A half chi-squared distribution is overlapped (magenta), which approximates well the null distribution. Increasing values of the parameter of interest μ_s are tested from top left to bottom right. *Below:* Null p-value calculated from both Monte Carlo (black dots) and the asymptotic formula (magenta diamonds). The p-value assuming 1σ and 2σ shifts from the median of the alternative distribution for each hypothesised μ_s are also indicated in green and yellow, respectively. The crossing point between the 10% horizontal line (in red) and the median p-value line (dashed black line) determines the projected 90% upper limit on the POI.

distribution (black dots) and the asymptotic formula (magenta diamonds), and generally a good agreement is observed. The projected 3σ discovery limit, $\mu_s^{3\sigma}$, is found at the intersection point

$$\begin{aligned} p(\mu_s^{3\sigma}) &= 1 - \Phi(3) \\ &= 0.14\% \end{aligned} \tag{4.19}$$

where $\Phi(Z)$ is the normal cumulative function.

Furthermore, a *discovery significance* analysis can be run by simply replacing the keyword `sensitivity` in the previous example by the full path to a data file with a distribution of events that are specified using the same vector of observables that are considered by the total probability model. In this case, we are assessing what is the discovery significance of the given experimental observation compared to the background-only hypothesis. As an example, Figure 4.7 shows the distribution of one-sided PLR test statistic of Eq. (4.16) for the background-only hypothesis. In addition, the corresponding asymptotic formula is shown in magenta, and the test statistic evaluated on the input data is indicated by the vertical black line.

The area to the right of the observed test statistic is used as a quantitative measure of the agreement between the observed data and the background-only model (i.e. the null p-value). In this particular example the p-values of 0.016 and 0.018 are obtained from the Monte Carlo distribution and the asymptotic formula, respectively. This corresponds to a discovery significance of 2.2 and 2.1σ, respectively. Indeed, the mock data set that was used in this example contained a handful of WIMP-like events that were artificially added on top of a random background distribution, which explains the approximately 2σ discovery significance that was obtained in this test.

It is also possible to run a *Bayesian analysis* with `LZStats`. This analysis allows for both the calculation of an upper limit and the establishment of a discovery, as explained below. The input arguments to the submission script to run a Bayesian analysis are:

```
40 vanilla_wimp path/to/data/file 2
```

According to Bayes' theorem, the probability distribution for the model parameters $\boldsymbol{\theta}$ given a data set $\mathscr{D}$, known as the *posterior*, is calculated as

$$P(\boldsymbol{\theta}|\mathscr{D}) = \frac{P(\mathscr{D}|\boldsymbol{\theta})P(\boldsymbol{\theta})}{P(\mathscr{D})} \,. \tag{4.20}$$

Here, $P(\mathscr{D}|\boldsymbol{\theta})$ is the *likelihood*, representing the probability that a data set $\mathscr{D}$ is observed given the model parameters $\boldsymbol{\theta}$, and $P(\boldsymbol{\theta})$ is the *prior* probability assigned to each model parameter. In the denominator, $P(\mathscr{D})$ is called the *evidence*, and it is used to normalise the posterior PDF

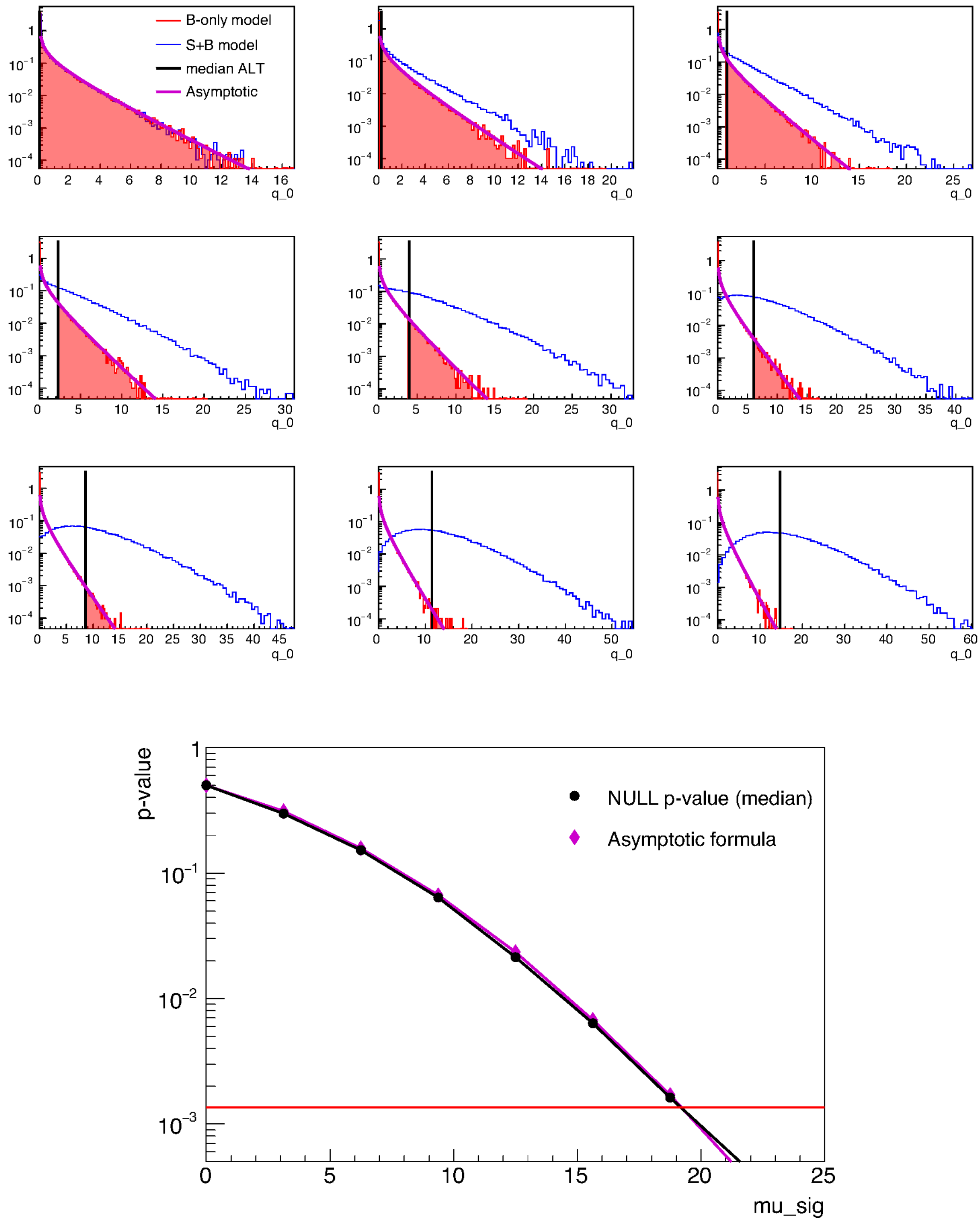

Figure 4.6: `LZStats` output from a projected discovery significance analysis. *Above:* Test statistic distributions under the null (background-only, in red) and alternative hypotheses (signal plus background, in blue). The one-sided PLR test statistic for discovery is used, defined in Eq. (4.16). The median of the alternative distribution is marked with a black line. A half chi-squared distribution is overlapped (magenta), showing a good agreement with the Monte Carlo prediction. Increasing values of μ_s (the POI) are considered from top left to bottom right. *Below:* Null p-value calculated from both the Monte Carlo histograms (black dots) and the asymptotic formula (magenta diamonds) for the same values of μ_s considered in the above plot. The 3σ projected discovery limit ($\mu_s^{3\sigma}$) is found at the crossing point between the 0.14% horizontal line (in red) and the median p-value line (black line).

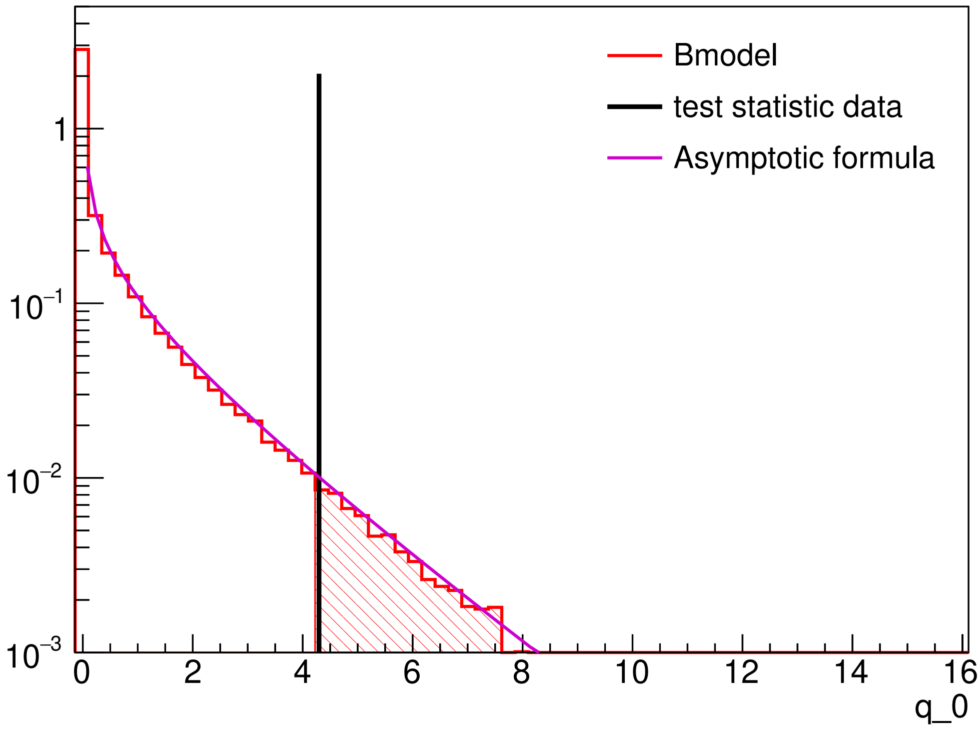

Figure 4.7: `LZStats` output from a discovery significance analysis. The test statistic distribution for the background-only model is indicated in red, the asymptotic formula in magenta and the test statistic evaluated on the input data in black. The null p-value, highlighted in red, is used as a measure of the compatibility between the background-only model and the measured data. A p-value of 0.016 is obtained from the Monte Carlo distribution, which corresponds to a 2.2σ discovery significance.

to unity. Once the posterior has been calculated, a PDF of the parameter(s) of interest can be easily obtained by integrating out the nuisance parameters, a process called *marginalisation*.

Markov Chain Monte Carlo (MCMC) sampling methods are used to estimate the posterior function. As an example, the upper panel in Figure 4.8 shows the estimated posterior distribution of the parameter of interest μ_s obtained using the widespread Metropolis-Hastings algorithm [235, 236]. The vanilla SI WIMP model is used as reference, and a random data set with background-only events was considered. This plot shows our estimation of the probability distribution of the parameter of interest, which has been informed by the input data. In this case, the estimated posterior seems to indicate that the most likely value of μ_s is around 0, and hence there is no ground to claim a discovery. By contrast, if the posterior distribution showed a clear departure from $\mu_s = 0$, this would be used as evidence to claim a discovery. An upper limit on the parameter of interest can be calculated by integrating the posterior distribution to a specific confidence level. In particular, the grey region shows the 90% area of this distribution integrated from the left, and the end point of this area on the right marks the position of the 90% CL upper limit on the parameter of interest, $\mu_s^{90\%}$.

In addition, `LZStats` returns a series of diagnostic plots to assess the convergence of the Markov chain. For instance, a trace plot for each model parameter is returned, in which the value of the parameter is shown at each step of the chain. Ideally, the trace plot of each parameter should be well mixed with each other (i.e. there are no observed correlations), and the variation of each parameter should become stationary around some value [237]. An example of the trace plots of the negative log-likelihood and the parameter of interest μ_s are shown in the lower panel of Figure 4.8. Some initial steps were discarded, indicated in red and known as "burn-in", to ensure optimal mixing of the model parameters.

4.4 Projected sensitivity to vanilla WIMPs

Having summarised the broad capability of the `LZStats` framework, we now present the projected sensitivity of the LZ experiment to WIMP-nucleus scattering interactions for its complete exposure of 1000 live days of a 5.6-tonne fiducial mass. We adopt the "vanilla WIMP model" that was described in Section 3.1, and we follow the profile likelihood ratio (PLR) method that has been introduced in this chapter using an event probability model that depends on the two observables S1 and S2. For a fixed WIMP mass, the experiment's sensitivity is defined as the median 90% confidence level upper limit on the WIMP-nucleon scattering cross section that would be obtained over repeated background-only experiments. The sensitivity projections presented in this thesis build upon previous work presented in both the LZ TDR [1]

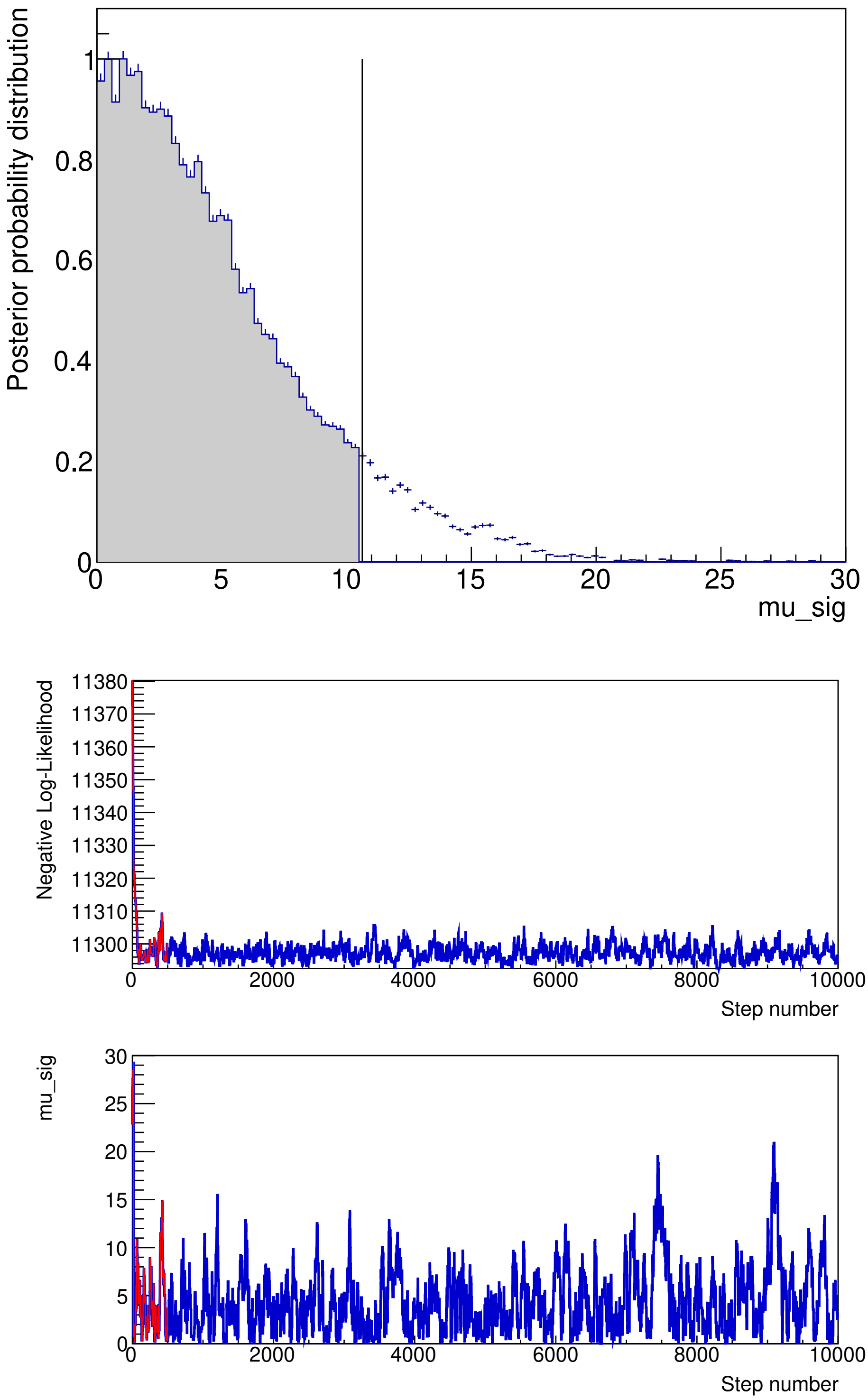

Figure 4.8: `LZStats` output from a Bayesian analysis. *Above:* The estimated posterior probability distribution of the parameter of interest μ_s obtained using the Metropolis-Hastings algorithm. The vanilla SI WIMP model is adopted, and a random data set with only background events was considered. The grey area depicts the 90% probability area integrated from the left, and the black line marks the position of the 90% CL upper limit on the parameter of interest, $\mu_s^{90\%}$. *Below:* Trace plots of both the negative log-likelihood and the parameter of interest μ_s. The burn-in steps are indicated in red.

and the WIMP sensitivity article [2], and the specific changes and improvements with respect to these previous results will be highlighted accordingly.

Firstly, it is important to emphasise the difference between an *exclusion limit* and a *sensitivity projection*. Although the procedure to calculate both is similar, the motivation is different. Whilst an exclusion limit is a property of the observed data and defines a region in the model parameters space that is ruled out, a sensitivity projection is characteristic of the experiment and informs us of the region of the parameter space that the experiment will potentially explore. This section is focused on the latter case, whilst some examples of the former case were given in Section 2.3.1.

The background model is based on the 11 components that are listed Table 4.1, which includes the largest background contributions from Table 3.3 that was presented on page 81. The contribution from "Detector components", "Surface contamination" and "Environmental" are summed together into a single component named "Detector + Surface + Environmental", with both an ER and NR contribution. By contrast, the ^{8}B and hep solar neutrinos are treated separately since they represent an important background for low WIMP masses. The corresponding recoil energy spectrum of each of these backgrounds is displayed in Figure 3.10 for ER sources and Figure 3.11 for NR sources.

Also, Table 4.1 shows the uncertainty that is assigned to each of the background means. The uncertainties on the "Detector + Surface + Environmental" ER and NR components are based on the simulations that were performed to estimate the background counts in Table 3.3, and have been assigned a conservative value of 20% [2]. By contrast, the uncertainty on the neutrino components is mainly due to the neutrino flux uncertainties. Regarding the dispersed sources, the uncertainties on the radon-induced background are assumed to be dominated by the uncertainty in the branching ratios of "naked" beta decays of ^{214}Pb and ^{212}Pb, whereas those on ^{136}Xe $2\nu\beta\beta$ and ^{85}Kr come from their associated energy spectrum uncertainty at low energies.

The signal model is based on the "vanilla WIMP model" introduced in Section 3.1, with $v_0 = 220\,\mathrm{km/s}$, $v_{\mathrm{esc}} = 544\,\mathrm{km/s}$, $v_E = 230\,\mathrm{km/s}$ and $\rho_0 = 0.3\,\mathrm{GeV/c^2}$. The Helm form factor [173] is used in calculation of the SI WIMP-nucleon recoil rate, whereas the nuclear structure functions from [175] are considered for the calculation of the SD WIMP-nucleon recoil rate. Examples of the predicted recoil energy spectrum from SI and SD WIMP-nucleus elastic scattering interactions for different WIMP masses were given in Figure 3.2.

Signal and background probability distributions are generated by taking samples from the corresponding recoil energy spectra and converting them into the corrected (flat-fielded) S1 and S2 signals following the methodology discussed in Section 3.3.2. The projected detector parameter values listed in Table 3.2 are adopted when making this conversion from recoil energies to S1 and S2 observables. No position information is included in the list of observables; the majority of background sources are expected to be distributed uniformly in the active region of the detector, and for those that does not (such as "Detector + Surface + Environmental") they are expected to generate events mainly in the vicinity of the TPC wall, which will be rejected by the fiducial volume cut. However, it is important to highlight that the event's position information will be included in the list of observables in any analysis of real LZ data (i.e. not simulated).

An example of a simulated data set in the $\mathrm{S1_c}$-$\mathrm{S2_c}$ plane as it would be detected by the LZ experiment after its complete exposure is shown in Figure 4.9. This corresponds to a background-only experimental realisation, and the same ER and NR bands that were calculated in Section 3.3.2 are also shown here in blue and red, respectively. Furthermore, the expected 1σ and 2σ contours for a $40\,\mathrm{GeV/c^2}$ WIMP signal and the ^{8}B signal are overlaid.

The largest contribution to the ER background comes from radon daughter events, while ^{8}B neutrino events dominate the NR background, with an expected count of 38 in the full LZ exposure. Additionally, Figure 4.9 shows that there is a good separation in the observable space $(\mathrm{S1_c},\mathrm{S2_c})$ of a $40\,\mathrm{GeV/c^2}$ WIMP signal from the main expected backgrounds for the WIMP search. In fact, the PLR method takes into account the shape of the expected signal and background PDFs and it generally provides a better discrimination at all WIMP masses than a simpler "cut-and-count" method [1].

The full LZ likelihood function for the WIMP search is constructed following the formalism introduced in Section 4.1. The set of observables considered is $\boldsymbol{x}_e = (\mathrm{S1_c}, \log_{10}(\mathrm{S2_c}))$. The event probability model is composed of a signal component with an implicit dependence on the WIMP mass, $f_s(\boldsymbol{x}_e|m_\chi)$, and 11 background components, $f_b(\boldsymbol{x}_e)$, which are listed in Table 4.1. For each of the background PDF $f_b(\boldsymbol{x}_e)$ no implicit dependence on any model parameter is assumed in the present chapter (i.e. no shape-varying nuisance parameters such as g_1 or g_2). This is done to be able to compare with previous results, and to separate the calculation of the WIMP sensitivity from the topic of the impact of systematic uncertainties, which will be addressed in the next chapter.

The parameter of interest is the signal mean μ_s, which is directly proportional to the WIMP-nucleus scattering cross section. We will write the parameter of interest as $\mu_s(\sigma)$ to make this relation explicit. Conversely, the mean of each of the background components will be considered as nuisance parameters that are allowed to vary in the PLR analysis. A Gaussian constraint of the type $\mathcal{N}(\mu_b|a_b,s_b)$ will be assigned to each of the nuisance parameters μ_b to constrain their range of variability. Here, $\mathcal{N}$ is a normal probability distribution, a_b is the

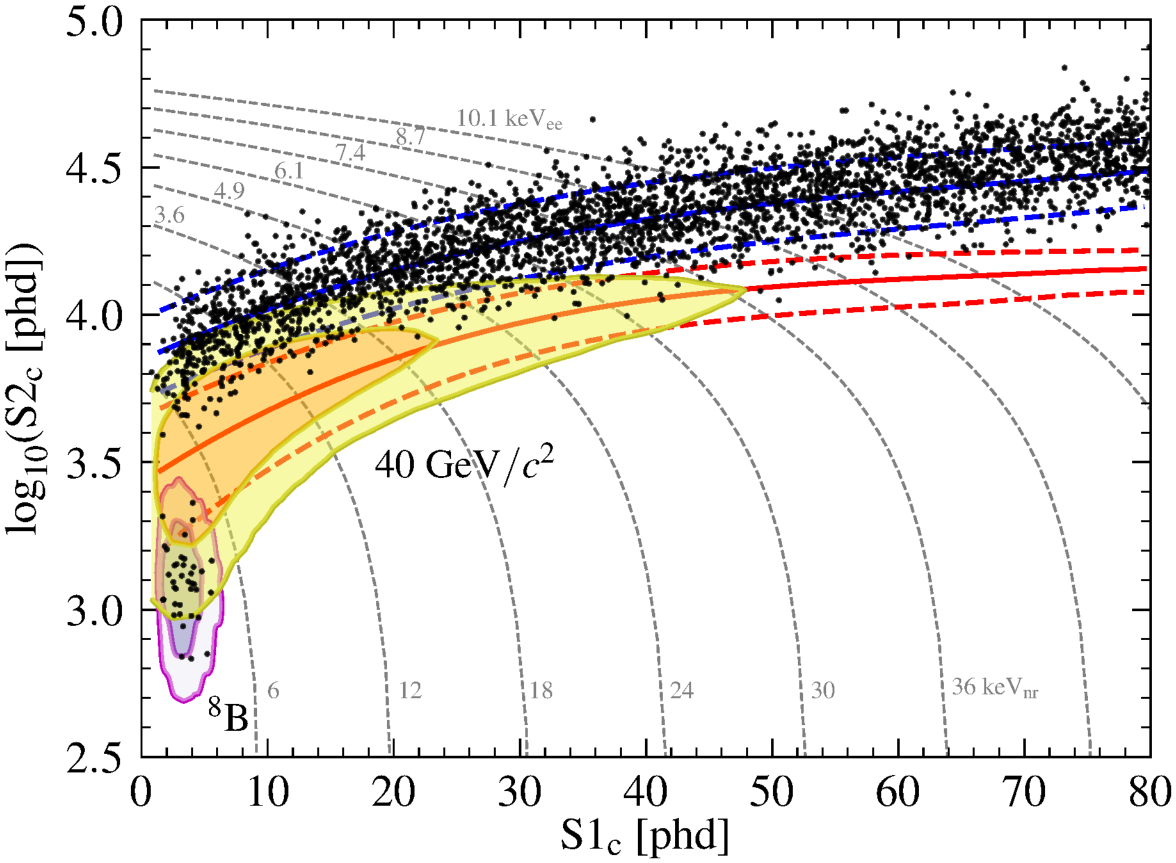

Figure 4.9: Simulated data set for a background-only realisation of the LZ experiment in a exposure of 1000 live days and 5.6 tonnes of fiducial mass. ER and NR simulated bands are indicated in blue and red, respectively, showing the median, 10% and 90% quantiles. The 1σ and 2σ contours for the low energy ^{8}B NR background, and a $40\,\mathrm{GeV}/c^2$ WIMP are also shown as shaded regions. Grey dashed lines indicate energy isocontours in ER and NR energy equivalent units (top and bottom labels, respectively), calculated using Eq. (3.28).

Table 4.1: Associated uncertainty on each of the background means entering the LZ likelihood in the vanilla WIMP analysis. The 11 background sources listed here correspond to the components that were presented in Table 3.3 with the largest contribution.

Background component	Symbol	Uncertainty
Detector + Surface + Environmental (ER)	μ_{DetER}	20% [2]
pp + ^{7}Be + ^{13}N solar neutrinos (ER)	μ_{pp}	2% [238]
^{222}Rn (ER)	$\mu_{\mathrm{Rn\text{-}222}}$	10% [222]
^{220}Rn (ER)	$\mu_{\mathrm{Rn\text{-}220}}$	10% [239]
^{136}Xe $2\nu\beta\beta$ (ER)	$\mu_{\mathrm{Xe\text{-}136}}$	50% [240]
^{85}Kr (ER)	$\mu_{\mathrm{Kr\text{-}85}}$	20% [241]
Detector + Surface + Environmental (NR)	μ_{DetNR}	20% [2]
^{8}B solar neutrinos (NR)	μ_{B8}	4% [242]
hep solar neutrinos (NR)	μ_{hep}	15% [238]
Diffuse supernova neutrinos (NR)	μ_{DSN}	50% [243]
Atmospheric neutrinos (NR)	μ_{atm}	25% [244]

estimated number of counts of that background component in the WIMP search region of interest and s_b is the associated uncertainty. Examples of both a_b and s_b are given in Table 3.3 and Table 4.1.

Taking all of the above into account, the LZ log-likelihood function for the vanilla WIMP analysis is given by

$$
\begin{aligned}
-2\log\mathscr{L}(\mu_s(\sigma),\boldsymbol{\nu}) = 2&\left(\mu_s + \sum_{b=1}^{N}\mu_b\right) \\
&- 2\sum_{e=1}^{n_0}\log\left(\mu_s(\sigma)f_s(\boldsymbol{x}_e|m_\chi) + \sum_{b=1}^{N}\mu_b f_b(\boldsymbol{x}_e)\right) \\
&+ \sum_{b=1}^{N}\frac{(\mu_b - a_b)^2}{s_b^2}
\end{aligned}
\tag{4.21}
$$

where $\boldsymbol{\nu}$ refers to the set of all nuisance parameters, the subscript e runs over each of the n_0 events in the data set considered for the likelihood evaluation and b is the background component index, ranging from 1 to N background components.

4.4.1 SI WIMP-nucleon scattering

The projected sensitivity of the LZ experiment to SI WIMP-nucleon scattering in its complete exposure is shown in the upper panel of Figure 4.10. For one given mass, the null and alternative distributions were generated using 5000 toys each and repeated over 20 test values of the POI (μ_s) equally spaced between 0 and 30. This process is iterated over a range of WIMP masses logarithmically spaced, and Figure 4.10 shows the interpolation between the resulting points.

The one-sided PLR test statistic for upper limits is used (defined in Eq. (4.14)). This is preferred over the two-sided test statistic because the goal of this study is to assess the sensitivity of the experiment; the results from a complementary study that estimates the discovery sensitivity of the LZ experiment are given below. However, note that this separation between calculating an exclusion limit or assessing the discovery significance is not so clearly defined when one is analysing real experimental data. As we concluded in Section 4.2, the recommended procedure in that case would be to decide *prior to looking at the data* a collection of tests (including a two-sided test *and* a one-sided test for upper limits, for instance) and report the results from all of them after the data have been analysed.

The best sensitivity on the SI WIMP-nucleon cross section is achieved at 40 $\mathrm{GeV/c^2}$, with a value of 1.3×10^{-48} $\mathrm{cm^2}$. This represents an improvement that is approximately 30-fold with respect to the currently most stringent limit on SI scattering, set by XENON1T [98], and a 100-fold from LUX [97]. Overall, the LZ experiment is expected to probe a significant fraction of the remaining parameter space above the sensitivity barrier imposed by the "neutrino floor" [108], indicated with the shaded orange region in Figure 4.10. At this region nuclear recoils from coherent elastic neutrino-nucleus scattering will saturate the signal region for all WIMP masses, making this type of search no longer feasible. However, and as mentioned in Chapter 2, the neutrino floor could be possibly overcome if there are improvements to the measurements of the neutrino fluxes, or new technologies with directional sensitivity are developed. Background from coherent elastic neutrino-nucleus scattering will become important in the WIMP search, specially from ^{8}B and hep solar neutrinos at low WIMP masses (i.e. less than $\sim$10 $\mathrm{GeV/c^2}$), and from atmospheric and diffuse supernova neutrinos at higher WIMP masses. Nonetheless, it is important to highlight that CEνNS represents also an interesting signal on its own, and LZ will most likely be able to detect it from ^{8}B solar neutrinos after only a few months of data taking.

A well-known problem when calculating frequentist upper limits is that they may exclude parameter values to which one has essentially no experimental sensitivity. This would happen, for instance, when testing very small cross sections, the predictions of which are almost indistinguishable from the background expectation. In such case, it would be desirable to avoid excluding these points of the model's parameter space where the experimental sensitivity is vanishingly small. The problem might be avoided using the "$\mathrm{CL_s}$ method", where the measure used to test a parameter value is based on a combination of p-values that increases

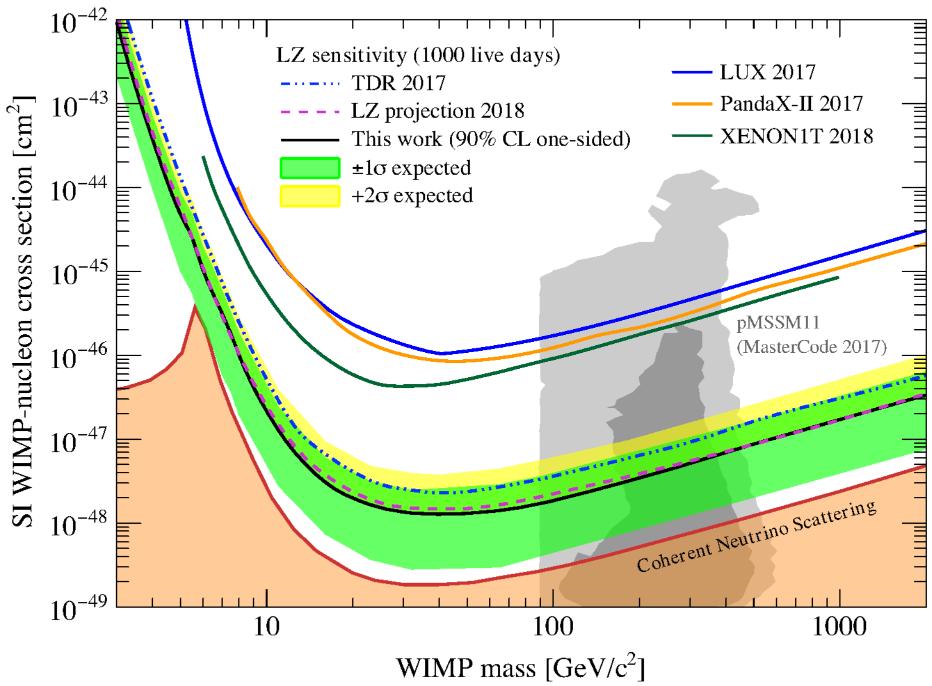

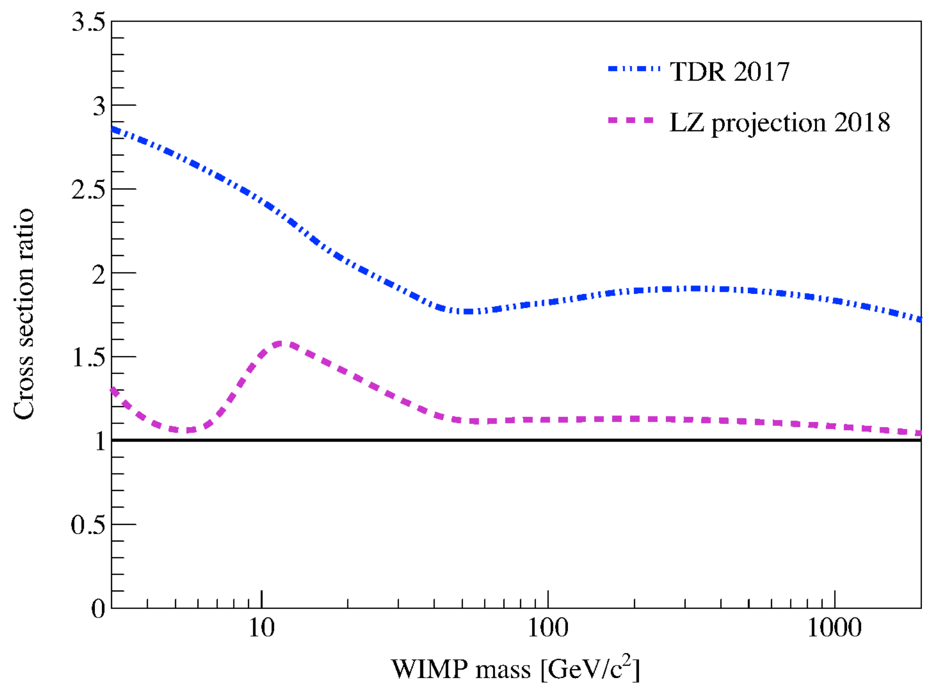

Figure 4.10: *Above:* LZ projected sensitivity to SI WIMP-nucleon elastic scattering for the complete exposure of 1000 live days of a 5.6-tonne fiducial mass. A minimum of 1.3×10^{-48} cm^2 is expected at 40 GeV/c^2. The -2σ expected region is omitted following the power-constrained method (see text). Previous LZ projections from [1] and [2] are shown in dash-dotted blue and dashed magenta, respectively. Exclusion limits from other LXe experiments are also shown [97, 100, 245]. The orange shaded area indicates the sensitivity barrier in which backgrounds from coherent scattering of neutrinos dominate [108], while the grey contours show the 1 and 2σ favoured regions from a recent global fit scan obtained by the MasterCode collaboration [107]. *Below:* Ratio of the previous LZ projections to the newest projection. The largest differences are observed at low WIMP masses.

for decreasing sensitivity [246]. However, the coverage of CL_s limits is usually larger than the nominal value (i.e. they overcover). Alternatively, the method of "power-constrained limits" (PCL), introduces a strict cut on the power of a hypothesis test, below which the parameter value is not regarded as testable [247]. The choice on this minimum power threshold is open, but recommended choices include 50% or 16% (i.e. the median or minus one standard deviation of a normal Gaussian). In this case, an equal coverage compared to the nominal confidence level is achieved for all the parameter values above the power threshold, and the coverage becomes 100% if the sensitivity goes below threshold. By contrast, the CL_s method starts already overcovering at larger parameter values [247].

This topic is of particular interest for LZ, since the experiment will explore regions of the WIMP parameter space that have very low signal expectations. In this thesis we adopt the second method presented above, and Figure 4.10 shows the power-constrained projection at a 16% power threshold. This is equivalent to applying the power constraint if the unconstrained projection fluctuated one standard deviation below its median, which explains why the lower side of the 2σ band is not displayed. The PCL method is more commonly applied to exclusion limits rather than sensitivity projections, but we opted for making this choice explicit in the projections presented in this work to motivate its use in future LZ analyses.

The upper panel in Figure 4.10 also shows past LZ projections from both the baseline scenario presented in the Technical Design Report (TDR) [1] and the WIMP sensitivity article [2]. The ratio of those past projections to the new one presented in this thesis is shown in the lower panel. The TDR projection is 2 to 3 times larger for masses below the minimum point at $40\,\mathrm{GeV/c^2}$, with the ratio staying constant around a factor of 2 for higher masses. By contrast, the projection from Ref. [2] is most different at a mass around $10\,\mathrm{GeV/c^2}$, with a ratio around 1.5, and remains very close to the current projection otherwise.

The change in these projections is due to several factors. Firstly, the nominal value of the light collection efficiency in LXe has changed from 7.5%, in the TDR, to 11.9%. The improvement of this value is mainly motivated by new measurements of the PTFE reflectivity which, as explained in Section 3.3, is known to be $\geq 97.3\%$ when immersed in LXe [210]. Secondly, a different version of the NEST software was used in the current work (`v2.0.0`). By contrast, the previous two projections were based on the older libNEST `5.0.0`. The new version of NEST introduces many improvements with respect to the previous version, including an improved ER model and a more accurate calculation of total quanta based on experimental data. The different prediction of the LXe yields by these two versions of NEST was shown in Figure 3.8. The left plot of this figure shows that NEST `v2.0.0` predicts a larger charge yield at low nuclear recoil energies, which is probably one of the important drivers for the improvement in sensitivity observed at low WIMP masses.

It is highly likely that radon will constitute the largest contribution to the total ER background in LZ,[6] as was shown in Table 3.3. The projected estimate of the specific activity of ^{222}Rn from emanation from detector components and dust is 1.81 μBq/kg [2]. This measurement is subject to some large uncertainties, specially from how the room temperature radon screening measurements translate to the cryogenic conditions at which the experiment will operate. Given the importance of this background component, and the difficulty in constraining it precisely before the start of operation, "high" and "low" radon scenarios have been considered where either pessimistic or optimistic assumptions, respectively, are made from the radon screening measurements. The impact of such changes on the SI sensitivity at 40 GeV/c^2 is shown in Figure 4.11. A gradual increase in the projected sensitivity is observed for increasing considerations of the radon's specific activity. Nevertheless, the sensitivity projection is better than 3×10^{-48} cm^2 for the highest radon estimates, which constitutes the LZ requirement in terms of WIMP sensitivity [1].

Moreover, the lower panel of Figure 4.11 shows the ratio of the average of the maximum likelihood estimators of the Rn-222 background mean ($\hat{\mu}_{\text{Rn-222}}$) from all the Monte Carlo toys to the corresponding global observable ($a_{\text{Rn-222}}$). The proximity to 1 of these measurements confirms that there is no apparent bias in the PLR fits for increasing values of the ^{222}Rn activity.

Finally, projected discovery significance projections at 1, 2 and 3σ are shown in Figure 4.12. The three different curves define the region of parameter space above which the LZ experiment would have the ability to exclude the background-only hypothesis at the indicated significance. This is obtained by testing increasing values of the SI WIMP-nucleon cross section against the null hypothesis $\mu_s = 0$ following the one-sided test statistic q_0, defined in Eq. (4.16). Note that the median of the alternative distribution is taken as the value of the observed test statistic and, therefore, these projections should be interpreted as representative of the median experiment over repeated realisations. A 1, 2 and 3σ median projection of 0.78, 1.86 and 2.98×10^{-48} cm^2 is achieved at 40 GeV/c^2, respectively. It should be highlighted that the projected 3σ discovery limit is below the currently most stringent 90% CL exclusion limit on the SI WIMP-nucleon cross section for all WIMP masses (shown in green) [98], leaving a sizeable region of the parameter space open for the discovery of a SI WIMP signal with the LZ experiment.

[6] We should emphasise that the ER background is not caused by the radon radioisotopes themselves, but from the naked beta emission from radon decay products. See more details in Section 3.4.

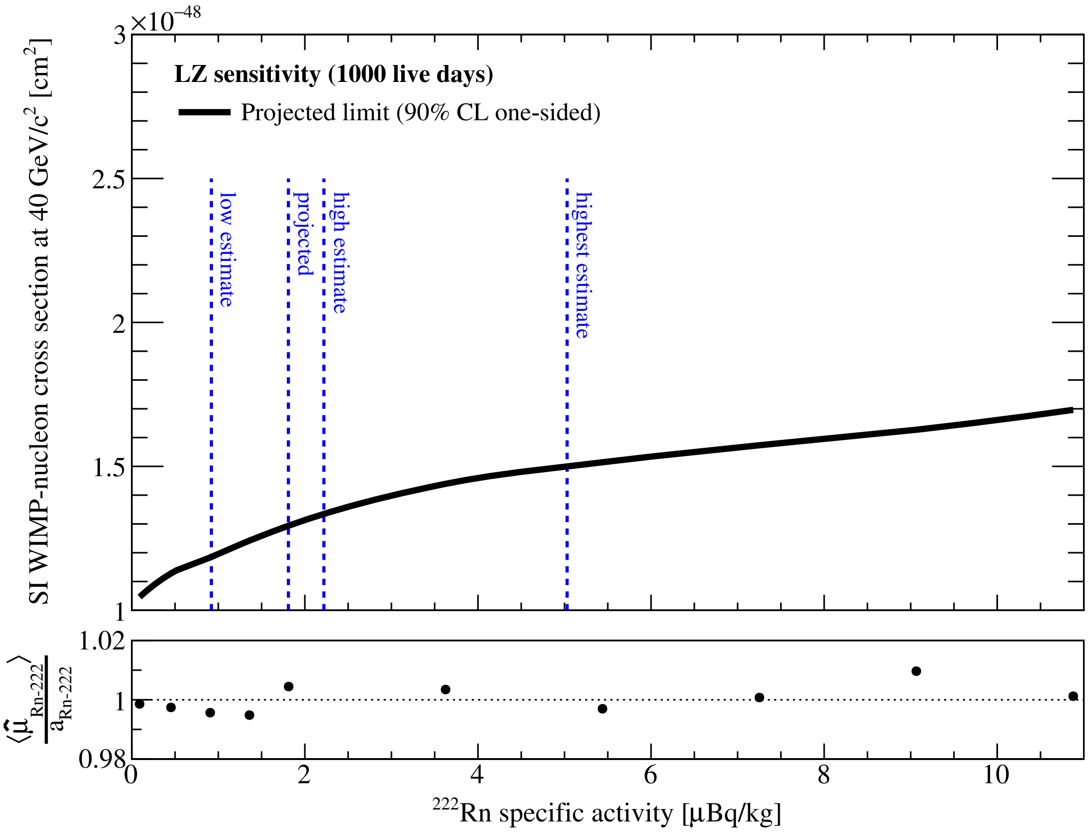

Figure 4.11: Projected SI sensitivity at 40 GeV/c^2 as a function of the ^{222}Rn activity. The projected estimate of the ^{222}Rn specific activity in LZ is 1.81 µBq/kg, marked with a vertical dashed line. Both pessimistic and optimistic scenarios based on the radon screening measurements are also marked. Only a moderate worsening of the projected sensitivity with increasing levels of the radon activity is observed. The lower panel shows the ratio of the average of the best-fit values from the PLR fits of the background mean $\mu_{\text{Rn-222}}$ to its corresponding global observable $a_{\text{Rn-222}}$, confirming that there is no bias in the fits for all the scanned activities.

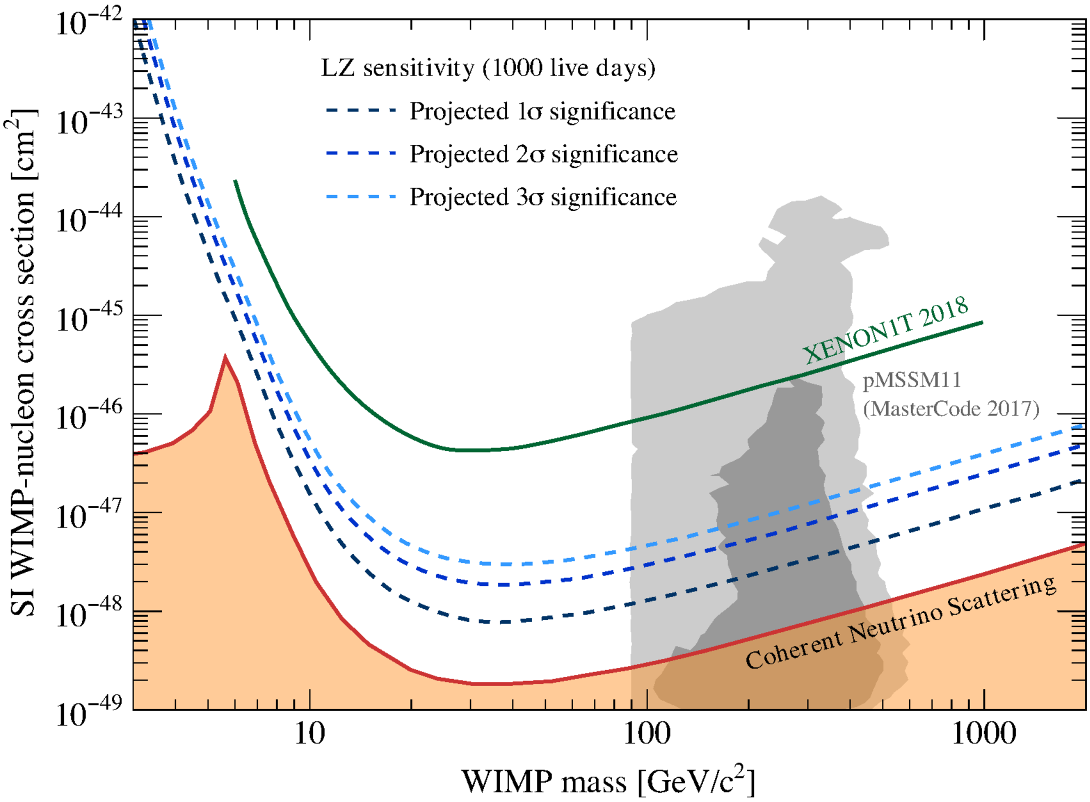

Figure 4.12: Discovery significance projections of LZ to SI WIMP-nucleon scattering. The 1σ, 2σ and 3σ median projections to reject the background-only hypothesis are shown (dashed blue lines, from darkest to lightest), as well the current most constraining 90% CL exclusion limit (solid green line) [98].

4.4.2 SD WIMP-nucleon scattering

As described in Section 3.1.2, a LXe experiment such as LZ is expected to have an excellent sensitivity to spin-dependent WIMP-nucleon scattering too. In particular, higher sensitivity to the WIMP-neutron scattering cross section is expected than to the WIMP-proton one from the two isotopes $^{129}_{54}$Xe and $^{131}_{54}$Xe, which have an unpaired number of neutrons. A non-negligible contribution in the WIMP-proton channel is expected due to 3-body interactions, as shown in Ref. [175]. These two isotopes have a combined natural abundance of 47.6%, which is sufficiently large to make the LZ experiment, with a predicted 5.6-tonne fiducial mass, competitive to these type of searches, and possibly world leading in the proton channel.

The projected SD sensitivity is shown in Figure 4.13, with the neutron channel in the left panel and the proton channel in the right one. A minimum of $2.2 \times 10^{-43}\,\mathrm{cm}^2$ is expected for SD WIMP-neutron scattering, while the minimum for SD WIMP-proton scattering is of $6.3 \times 10^{-42}\,\mathrm{cm}^2$, both at $40\,\mathrm{GeV/c}^2$. LZ is expected to cover a substantial region of the WIMP-neutron and WIMP-proton parameter spaces compared to the exclusion limits set by other experiments, a selection of which are shown in Figure 4.13. Furthermore, it will start probing some theoretically motivated regions of the parameter space, such as the regions shown in grey, which correspond to the 1σ and 2σ contours of a global fit based on supersymmetric extensions to the Standard Model and obtained by the GAMBIT collaboration [248]. One particular example of derived limits from collider searches under the MSMD model, introduced in Section 2.3.3, is shown in the left panel [249, 250]. Note that these are model dependent limits, and the particular choice that is assumed for the mediator coupling to quarks (g_q) and dark matter (g_χ) are indicated in the figure.

Furthermore, previous LZ projections from Ref. [2] are overlapped (dashed magenta), while there are no projections from the TDR in this case. As shown in these figures, there is a very small difference between the older and newer projections across all WIMP masses. The different behaviour compared to the SI case is probably due to the much reduced expected recoil rates for SD scattering (see Figure 3.2 for instance), which makes the sensitivity projection less sensitive to changes in the conversion process from recoil energy to observables.

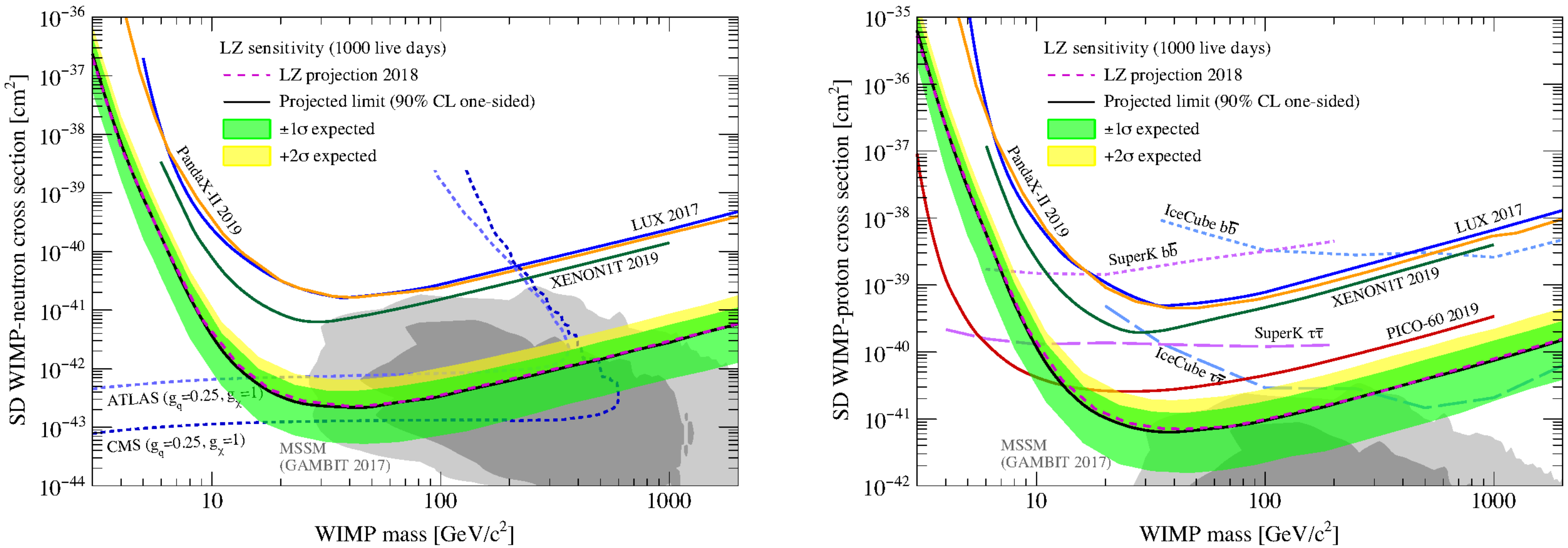

Figure 4.13: LZ projected sensitivity to SD WIMP-neutron (left) and WIMP-proton (right) elastic scattering for an exposure of 1000 live days of a 5.6-tonne fiducial mass. Variations from the median sensitivity are indicated by the green (1σ) and yellow (2σ) bands, with the latter only showing the $+2\sigma$ side because of the power-constraint method [247]. The best sensitivity of $2.2 \times 10^{-43}\ \mathrm{cm}^2$ and $6.3 \times 10^{-42}\ \mathrm{cm}^2$ is obtained for the neutron and proton channel, respectively, both at $40\,\mathrm{GeV}/c^2$. Previous projections from Ref. [2] are shown in dashed magenta for reference. The grey contours show the MSSM 1σ and 2σ favoured regions from a global fit conducted by GAMBIT [248]. Exclusion limits from other experiments are also added, as described below. *Left:* Exclusion limits from direct detection experiments are shown as solid lines [251, 252, 185]. The blue dashed lines indicate one example of derived limits from collider searches under the MSDM model and for the indicated parameter choices of the mediator couplings [249, 250]. *Right:* Exclusion limits from the same LXe experiments as above are shown, as well as the most recent upper limit from PICO-60 [253]. Limits from the leading neutrino observatories, in both the $b\bar{b}$ and $\tau\bar{\tau}$ annihilation channels, are also displayed [148, 254].

Chapter 5

Analysis of systematic uncertainties

The LZ sensitivity projections presented in the last chapter were calculated assuming a predefined collection of both astrophysical and detector parameters (as shown in Section 3.1 and Table 3.2, respectively). Only the background component mean rates were included in the list of nuisance parameters, allowing them to vary within their uncertainties in the PLR fits. Many other sources of uncertainty exist, but when including more one has to be mindful that some can be computationally expensive to profile out.

The goal of this chapter is to identify those model parameters with a significant uncertainty and rank them by their impact on the WIMP sensitivity. Knowing which parameters are the most impactful and in which cases (e.g. for particular WIMP masses) will provide valuable information in preparation for future analyses with real LZ data. The chapter concludes with a discussion on the effect that some of the systematic uncertainties studied here might have on the reconstruction of WIMP properties should we be in a position to claim a discovery.

5.1 Sources of uncertainty

We begin by listing those model parameters that could have, in principle, a significant impact on the WIMP sensitivity if their value were varied as much as their associated uncertainty reasonably allows. We will focus our attention on spin-independent interactions, and take the LZ projection shown in Figure 4.10 as the nominal case. Note that the aim of this study is not to determine the effect that taking extreme values of a given parameter will have on the projected sensitivity. That procedure is usually referred to as a *parameter scan*, and some examples with LZ parameters have already been shown in Section 12.3.3 of the LZ TDR [1].

By contrast, the goal of this study is to identify those model parameters that have the most significant impact on the WIMP sensitivity because of their associated uncertainty and motivate their future inclusion in the LZ likelihood function as nuisance parameters. Eleven nuisance parameters were already considered in the likelihood that was used to calculate the projections shown in Section 4.4, namely, the mean of each background component (μ_b). All these parameters act as normalisation factors on their PDFs, and the PLR method is able to incorporate any number of them with only a moderate increase in computational cost. However, there is another type of parameter that can slow down considerably the performance of the PLR method: the "shape-varying parameters". These are parameters that have an implicit dependence on one or several PDFs inside the likelihood; hence, a regeneration of those PDFs is needed every time that a new parameter value is explored. This process is computationally very costly and therefore the inclusion of any new shape-varying parameter into the list of nuisance parameters has to be studied with great care.

We divide the model parameters that are considered in the present study into two main categories: astrophysical and detector parameters. We review each parameter and motivate its assigned uncertainty in the next two sections.

5.1.1 Astrophysical parameters

As mentioned in Section 3.1.1, the WIMP-induced differential scattering rate is directly proportional to the *local dark matter density* (ρ_0). Therefore, our estimation of the number of expected WIMP-induced nuclear recoils in the LZ experiment will scale accordingly to this parameter. The direct dark matter community has traditionally adopted a value of $\rho_0 = 0.3\,\mathrm{GeV/cm^3}$, which has allowed for an impartial comparison of results between different experiments. However, a large dispersion in the measurement of this parameter has long existed; see, for instance, the comprehensive review on local dark matter density measurements in Ref. [158]. In the present study, we adopt the standard value of $\rho_0 = 0.3\,\mathrm{GeV/cm^3}$ and assign it a relative uncertainty of 30% to account for the large variability of measurements. We note that this uncertainty is likely to decrease in the near future once more data from the Gaia mission is analysed.

Figure 5.1 shows the effect of varying the value of ρ_0 on the SI differential event rate for four different WIMP masses. The nominal differential rate is shown in black, while the expected rate when ρ_0 is increased or decreased by its assigned uncertainty is shown in light and dark blue, respectively. As expected, a constant scaling across all the energy range is observed. The 30% variation on this parameter is apparent in Figure 5.2, where the relative difference with respect to the nominal rate is shown.

As mentioned in Section 3.1.1, the SHM model considers a Maxwell-Boltzmann velocity distribution that depends on two parameters: the *galactic escape velocity* ($v_{\rm esc}$) and the *local circular velocity* (v_0). The value that is traditionally used for $v_{\rm esc}$ is 544 km/s, which is based on a study by the RAVE collaboration that dates back a decade [164]. This value has been subsequently revised, and a recent study using a large sample of velocities of halo stars from the second data release of the Gaia mission finds $v_{\rm esc} = 580 \pm 63$ km/s [255]. Nevertheless, the canonical value of $v_{\rm esc} = 544$ km/s will be assumed in this study to be able to compare results with the sensitivity projections that were presented in Chapter 4. A 10% uncertainty is assigned to $v_{\rm esc}$ based on the typical precision achieved in the measurement of this parameter.

The local circular velocity has a standard value of $v_0 = 220$ km/s, with an uncertainty of approximately 10% [256, 257]. As pointed out in Ref. [258], the uncertainty on this parameter has recently been reduced thanks to a more precise determination of the solar position, favouring a value of $v_0 = 233 \pm 3$ km/s [259]. However, we will adhere to the standard convention in this study.

The effect of varying each of these parameters on the SI WIMP-nucleus differential event rate is shown in Figure 5.1. Note that the event rates for the 1 TeV/c^2 and 10 TeV/c^2 WIMP masses are almost indifferent to changes of these two parameters. This is expected, since $v_{\rm min} = \sqrt{m_A E_R/(2\mu_A^2)}$ loses its dependence on the WIMP mass for very heavy WIMPs (i.e. $\mu_A \approx m_A$ when $m_\chi \gg m_A$). Thus, $v_{\rm min} \propto \sqrt{E_R/m_A}$ and this parameter takes comparatively lower values in the energy range considered than in the case of lighter WIMPs. As a result, any change in the value of v_0 or $v_{\rm esc}$ will not have a significant effect on the fraction of WIMPs that are kinematically-allowed to scatter elastically and produce a detectable nuclear recoil (i.e. those with a velocity between $v_{\rm min}$ and $v_{\rm esc}$).

By contrast, the event rates at 6 and 40 GeV/c^2 are greatly affected, which is expected since in this case $v_{\rm min}$ and $v_{\rm esc}$ become closer to each other. As shown in Figure 5.2 the effect of changing the value of v_0 is larger than changing $v_{\rm esc}$ for a 40 GeV/c^2 WIMP. In the SHM model, v_0 determines both the mean and the dispersion of the WIMP velocity distribution. Hence, increasing v_0 will not only shift all the WIMP velocities to larger values but also make the tails of the distribution wider. This effect is expected to have a larger impact on the differential recoil rate than modifying the cut-off value of the distribution (i.e. $v_{\rm esc}$). However, this is not the case for a 6 GeV/c^2 WIMP, for which $v_{\rm min}$ and $v_{\rm esc}$ are much closer to each other and as a result changing either v_0 or $v_{\rm esc}$ are expected to have similar effects.

With the advent of new astrophysical data from the Gaia mission, new studies have emerged attempting to map the *dark matter distribution in the Milky Way*. In particular, the authors from Refs. [258] and [260] concluded that the new data suggest a significant departure

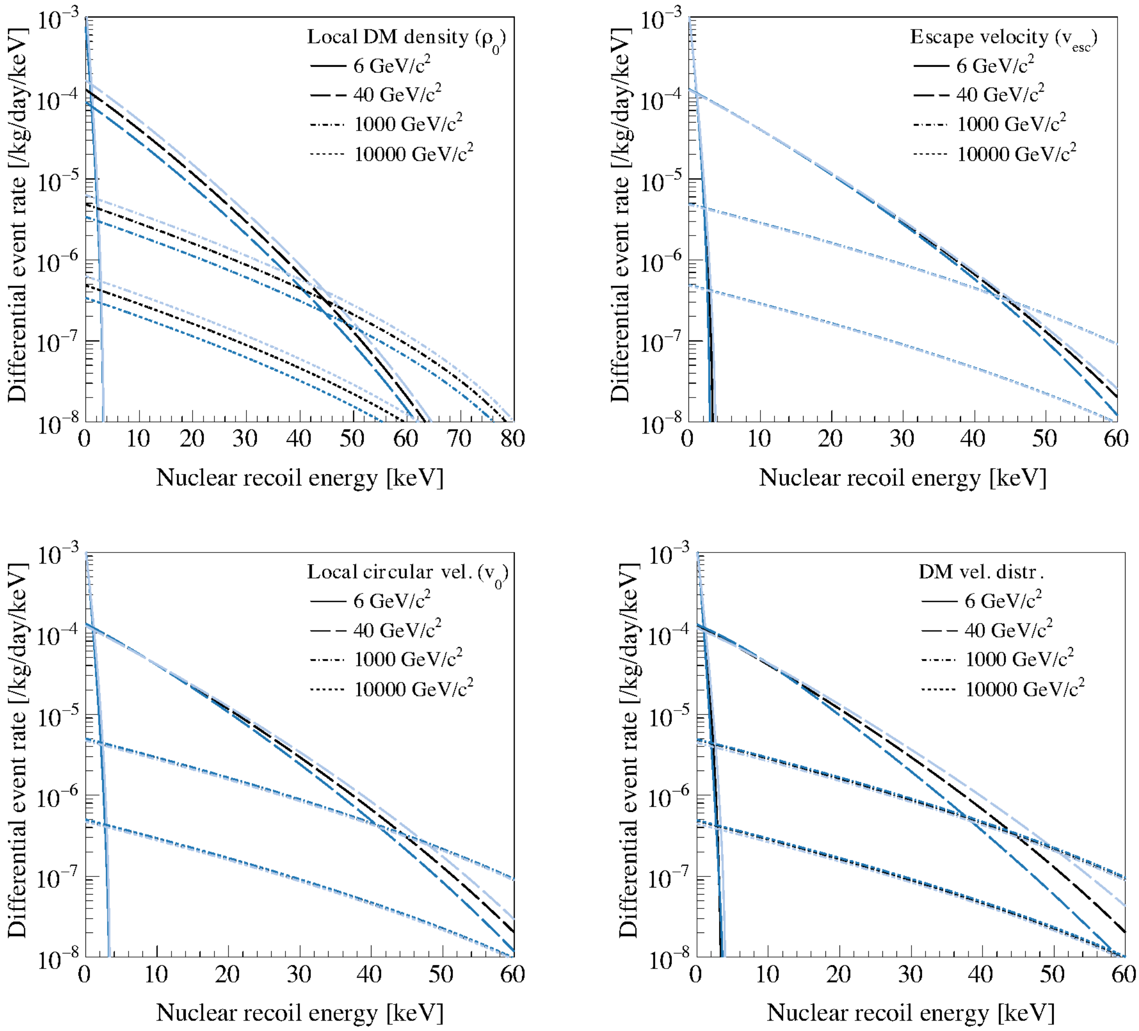

Figure 5.1: Spin-independent WIMP-induced differential event rate for different choices of astrophysical parameters. The nominal case is shown in black, while the lower and higher predictions after varying the corresponding model parameter by its assigned uncertainty are shown in dark and light blue, respectively. From top left to bottom right the model parameters are: the local dark matter density (ρ_0), the galactic escape velocity $(v_{\rm esc})$, the local circular velocity (v_0) and the dark matter velocity distribution $(f(v))$. We show the results for four different values of the WIMP mass, represented by different line styles. The assumed target nuclei is liquid xenon, and a SI WIMP-nucleon cross section of $\sigma_N^{\rm SI}$ =1 zb is considered.

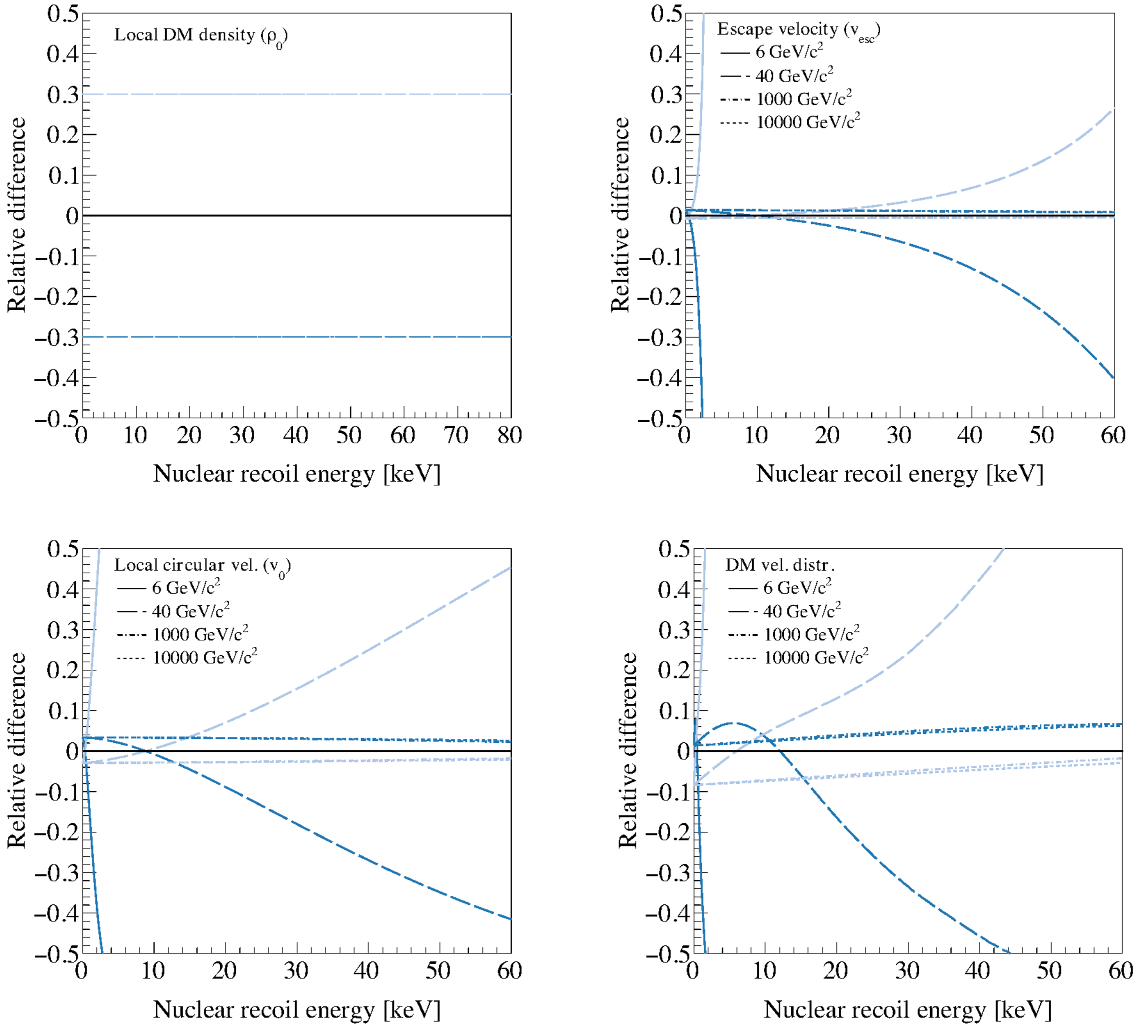

Figure 5.2: The relative difference in the SI WIMP-induced differential event rate due to varying astrophysical parameters. The same astrophysical parameters that are shown in Figure 5.1 are considered here. Four different WIMP masses are shown in each case, represented by different line styles. The same relative difference is observed for all WIMP masses for the local DM density (top left).

from the homogeneous and isotropic model assumed by the SHM. They propose that a new strongly radially anisotropic DM population should be considered in combination with the standard spherical halo, known as the "Gaia sausage" or "Gaia-Enceladus". Although this is a conclusion common to both works mentioned above, their prediction of the dark matter velocity distribution is different. The origin of this discrepancy is in the different methods they used to derive the velocity distribution. An *ad hoc* velocity distribution is given in Ref. [258] that captures the generic features of the two dark matter components described above, while the velocity distribution in Ref. [260] is built on the assumption that metal-poor halo stars are effective tracers of dark matter. A very recent analysis on the Auriga simulations [261] have found some strong discrepancies with some of the claims that were made in the previous two pieces of works, which suggests that further work is needed in this area.

These two velocity distributions, as well as the SHM distribution, are shown on the left panel of Figure 5.3. The predicted velocity distribution from Ref. [260] will be referred to as "Necib *et al.*", whereas the one from Ref. [258] will be labelled "SHM^{++}". The three velocity distributions are plotted in the Earth frame and integrated over the spherical angular coordinates in velocity space (i.e. $f_{\oplus}(v) = v^2 \int f_{\oplus}(\boldsymbol{v}) \sin\theta d\theta d\phi$, where $v = |\boldsymbol{v}|$). $f_{\oplus}(\boldsymbol{v})$ is obtained by boosting the DM velocities in the galactic frame by the Earth's velocity $\boldsymbol{v}_{\mathrm{E}}$, as explained in Section 3.1.1. The Necib *et al.* distribution has a smaller dispersion and is shifted towards lower WIMP velocities, that is, it predicts slower WIMPs on average. By contrast, the SHM^{++} distribution is shifted to higher velocities, and it has a slightly longer tail. However, it is important to mention that these changes are mainly due to the larger values of v_0 and v_{esc} that are assumed in the SHM^{++} model [258].

The WIMP velocity distribution enters in the calculation of the WIMP-induced differential scattering rate via the mean inverse velocity integral, $\zeta(E_R,t)$, as explicitly shown in the scattering rate formulas (3.14) and (3.20). Therefore, we can quantify what the effect of modifying the DM velocity is by directly studying the variation of the function $\zeta(E_R,t)$. The right panel of Figure 5.3 shows the mean inverse velocity function for the three astrophysical models under consideration. Note that the function is averaged over time (i.e. averaging out the annual modulation component). In addition, the function is evaluated in units of v_{min}, instead of E_R, but they are monotonically-related quantities (as shown in Eq. (3.2)). We can see from this figure that the differences between the Necib *et al.* and SHM^{++} models are noteworthy, and they will have a particularly important effect on the recoil rate of low to mid-range WIMP masses, which are mainly sensitive to the tail of this function. The relative difference with respect to the nominal differential scattering rate is shown in Figure 5.2, which confirms that the 6 and 40 $\mathrm{GeV/c^2}$ WIMP rates are the ones with the largest variation.

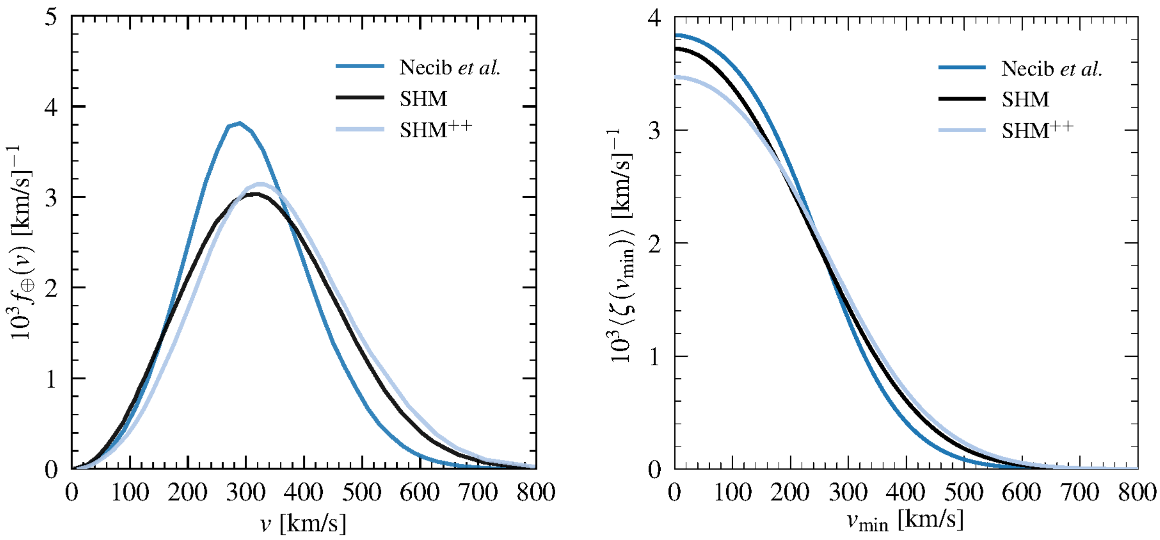

Figure 5.3: *Left:* Dark matter velocity distribution predicted by three different astrophysical models: SHM (black), Necib *et al*. (dark blue) [260] and SHM^{++} (light blue) [258]. The velocity distributions are plotted in the Earth frame, and they are integrated over the spherical angular coordinates. The Necib *et al*. model predicts slower dark matter particles and is more peaked than SHM, whereas SHM^{++} suggests faster particles. *Right:* The mean inverse velocity function $\zeta(v_{\rm min})$ averaged over time for the same models considered in the left panel. Medium to light WIMPs are mostly sensitive to the upper tail of this function, while heavy WIMPs are mostly affected by the lower tail.

Table 5.1: Values of the parametric formula, Eq. (5.1), that best reproduce the three dark matter velocity distributions indicated in the text.

Model	$(\theta_1, \theta_2, \theta_3)$ [km/s]
Necib *et al.*	$(174.6, 246.6, 566.4)$
SHM	$(218.0, 235.5, 617.3)$
SHM^{++}	$(217.9, 262.9, 802.9)$

In order to take into account the uncertainty on the DM velocity distribution, we consider Necib *et al.* and SHM^{++} as two opposing models that define some reasonable boundaries around the canonical SHM model. We derive a parametric formula that smoothly transitions between the three curves shown in the right panel of Figure 5.3. This parametric formula depends implicitly on the three parameters $\boldsymbol{\theta} = \{\theta_1, \theta_2, \theta_3\}$ and takes the form

$$\zeta(x|\boldsymbol{\theta}) = \frac{1}{2\theta_1}\left(\mathrm{erf}\left(\frac{x+\theta_1}{\theta_0}\right) - \mathrm{erf}\left(\frac{x-\theta_1}{\theta_0}\right) - \mathrm{erf}\left(\frac{\theta_1-\theta_2}{\theta_0}\right) - \mathrm{erf}\left(\frac{\theta_1+\theta_2}{\theta_0}\right)\right), \quad (5.1)$$

where $\mathrm{erf}(x)$ is the error function. The combination of values that best reproduces each of the astrophysical models is given in Table 5.1.

A summary of the astrophysical parameters that are considered in the present study is shown in Table 5.2, giving their nominal value and assigned uncertainty.

5.1.2 Detector parameters

Detector parameters can be another important source of uncertainty. Some parameters, such as the electron lifetime or the mass in the fiducial region, will be measured precisely during the commissioning of the experiment. Other parameters might be more difficult to estimate, or they depend on other parameters with an intrinsically large uncertainty; for instance, spatial and temporal variations in the drift field (such as those caused by PTFE charging in LUX [262]). In order to broadly capture the main sources of uncertainty from the point of view of the detection of S1 and S2 signals, and partly motivated by previous work published by the LUX experiment, we focus our attention on three elements that were introduced in Chapter 3: the g_1 and g_2 gain factors for the S1 and S2 channels, respectively, and the scintillation and ionisation liquid xenon yields for nuclear recoils.

Firstly, any uncertainty on the measurement of the quantum efficiency of the PMTs or on the reflectivity of the materials inside the TPC will affect the value of g_1, which translates directly to the detection threshold in a standard S1+S2 analysis. We adopt a nominal value of

0.12 phd per emitted photon in the liquid. The precision achieved by LUX on this parameter was ∼2.5% [208], although it should be noted that an additional systematic uncertainty of ∼10% comes from the absolute calibration of the PMT quantum efficiency as quoted conservatively by the manufacturer. Taking these two points into account, we choose to adopt an uncertainty of 5% on this parameter.

Secondly, the value of g_2 depends, in addition to the former considerations, on the electron extraction efficiency at the liquid-gas interface and the average size of the response to a single electron. A nominal value of 79.2 phd per emitted electron is assumed and an uncertainty of 5% will be assigned to this parameter too. Is is worth mentioning that the NEST package calculates g_2 from the two factors mentioned above instead of taking it as an input parameter. Therefore, we split the 5% uncertainty quadratically between the electron extraction efficiency and the average SE size. We note that the former can only achieve such a small uncertainty if the extraction field is high enough so that the extraction probability is close to saturating near unity (as we assume here).

Thirdly, the *scintillation and ionisation yields* in liquid xenon are not precisely known at very low recoil energies. As mentioned in Section 3.2, the scintillation yield (L_y) is related to the number of photons that are emitted in LXe in a particle interaction, while the number of electrons released is modelled by the ionisation yield (Q_y). Both yields are subject to significant uncertainties at very low energy recoils, where not much data are available. This was shown in Figure 3.3, where a greater dispersion of the data and enlarged error bars are apparent in both the electron and nuclear recoil yields at energies below 2 keV. In order to capture this effect, an uncertainty is assigned to the yields returned by the NEST software (`v2.0.0`) that changes in value from 20% to 5% in the energy range of 0.1–2 keV, and remains constant at 5% for larger recoil energies. The function that models the variation of the uncertainty in the energy range 0.1–2 keV is

$$\sigma_\mathrm{y} = 0.0846 - 0.1154 \log(E_R[\mathrm{keV}]), \tag{5.2}$$

which decreases linearly in $\log(E_R)$ from 20% to 5%. This should be regarded as a reasonable choice based on the data shown in Figure 3.3, and the yield uncertainty bands that have been suggested in a public analysis note released by the NEST collaboration [205]. Naturally, this is not the only method to model the uncertainty of the LXe yields predicted by NEST at low energies.

The scintillation and ionisation yields will be varied in opposite directions:

$$\begin{aligned} &\text{Lower light yield:} \quad \big(L_\mathrm{y}(1-\sigma_\mathrm{y}), Q_\mathrm{y}(1+\sigma_\mathrm{y})\big) \\ &\text{Higher light yield:} \quad \big(L_\mathrm{y}(1+\sigma_\mathrm{y}), Q_\mathrm{y}(1-\sigma_\mathrm{y})\big) \end{aligned} \tag{5.3}$$

Table 5.2: List of parameters considered for the nuisance parameters impact study. Their nominal value as well as the uncertainty assigned to each of them is indicated.

Source of uncertainty	Nominal value	Uncertainty
Local DM density (ρ_0)	$0.3\,\mathrm{GeV/cm^3}$	30%
Escape velocity (v_{esc})	$544\,\mathrm{km/s}$	10%
Local circular velocity (v_0)	$220\,\mathrm{km/s}$	10%
Mean inverse function $(\zeta(v_{\mathrm{min}}\|\theta_1,\theta_2,\theta_3))$	$(218.0, 235.5, 617.3)$	[Necib, SHM^{++}]
g_1 factor	0.12 [phd/γ]	5%
g_2 factor	79.2 [phd/e^-]	5%
NEST yields $(L_{\mathrm{y}}, Q_{\mathrm{y}})$	Figure 3.3	5–20%

with σ_{y} representing the uncertainty on the yields. This is done in this way to preserve the anticorrelation between the two yields, which is assumed for all recoil energies in NEST `v2.0.0` [203]—see energy formula in Eq.(3.24). However, it is important to note that such anticorrelation might not be preserved at very low recoil energies, as has already been suggested by new measurements of the NR ionisation yield of liquid xenon in the sub-keV regime [204]. A very recent model that takes this new charge yield into account has been implemented in NEST `v2.0.1`, but for consistency with the rest of the work presented in this thesis we will use `v2.0.0`.

5.2 Impact of systematics on the WIMP sensitivity

We proceed to calculate the impact of each of the model parameters shown in Table 5.2 on the LZ sensitivity to the SI WIMP-nucleon cross section. For a given WIMP mass, the impact is defined as the relative change in cross section from the SI projection, shown in Figure 4.10, when the model parameter under study is varied by $\pm 1\sigma$ from its nominal value.

The results for the same four WIMP masses considered earlier are summarised in Table 5.3. In each column of this table, the corresponding impact when the model parameter is decreased in value is shown on the left, and the opposite case on the right. Note that a negative impact implies a better sensitivity, while a positive impact means that the resulting projection is worse. Figure 5.4 shows the ranking of these parameters for each WIMP mass based on the combined impact between the positive and the negative variation. The individual impacts when a lower or a higher value of the corresponding model parameter is assumed are shown in dark and light blue, respectively.

Table 5.3: Summary of the impact of different sources of uncertainty on the projected LZ sensitivity to the SI WIMP-nucleon cross section for four different WIMP masses. The relative impact of each source is given for a variation of the corresponding parameter by the amount indicated in Table 5.2. In each column, the number on the left corresponds to the impact when the value of the parameter is decreased and vice versa for the number on the right. A negative impact means a better sensitivity.

Source of uncertainty	**Impact** $= \Delta\sigma/\sigma_0$ (%)			
	$6\,\mathrm{GeV/c^2}$	$40\,\mathrm{GeV/c^2}$	$1\,\mathrm{TeV/c^2}$	$10\,\mathrm{TeV/c^2}$
Local DM density (ρ_0)	34.4 / −26.5	34.6 / −25.9	33.3 / −24.3	33.9 / −24.5
Escape velocity (v_{esc})	26.1 / −20.9	3.0 / −2.6	−1.9 / 1.0	−2.0 / 1.1
Local circular velocity (v_0)	29.5 / −24.8	4.2 / −4.7	−2.1 / 2.4	−2.2 / 2.1
DM velocity distribution $(f(v))$	71.2 / −49.3	6.5 / −5.6	−4.0 / 6.3	−3.9 / 6.4
g_1 factor	7.0 / −6.8	2.4 / −2.2	0.5 / −0.5	0.5 / −0.5
g_2 factor	3.9 / −3.0	2.7 / −2.6	0.7 / −1.1	0.7 / −0.5
LXe yields $(L_{\mathrm{y}}, Q_{\mathrm{y}})$	8.8 / −6.3	2.4 / −2.1	0.9 / −0.7	1.0 / −0.8

The astrophysical parameters dominate the ranking for all WIMP masses, with the local dark matter density and the dark matter velocity distribution always scoring the highest. Also, the largest impacts are found for the $6\,\mathrm{GeV/c^2}$ case, for which combined impacts larger than 50% are observed for all the astrophysical parameters. Naturally, these effects are significantly amplified for even lower masses, which we do not consider here. It is worth noting that the impacts at 6 and $40\,\mathrm{GeV/c^2}$ follow a similar behaviour, whereby we obtain negative impacts for higher parameter predictions and vice versa for lower parameter estimates. Conversely, the DM velocity distribution, local circular velocity, and escape velocity show the opposite behaviour for the 1 and $10\,\mathrm{TeV/c^2}$ WIMP masses. This was expected, since as Figure 5.2 reveals the differential event rate of the heavy WIMPs decreases for a higher value of any of these three parameters and vice versa.

Furthermore, the impacts of the local DM density are asymmetric, even though the same upward and downward variation is considered for this parameter. This can be best understood by looking at the conversion between the projected 90% CL limit on the signal mean (the POI) to the WIMP-nucleon cross section, specifically

$$\sigma_N^{90\%} = \frac{\mu_s^{90\%}}{R_s \varepsilon} \,. \tag{5.4}$$

Here, μ_s is the signal mean, R_s is the integrated signal rate in counts/kg/day and ε is the exposure of the experiment in kg $\times$ day. Any increase of the signal to background ratio will result in a lower projected limit on μ_s, while a larger predicted signal rate will increase the value of the denominator. A variation of 30% of the local DM density (ρ_0) only affects modestly the

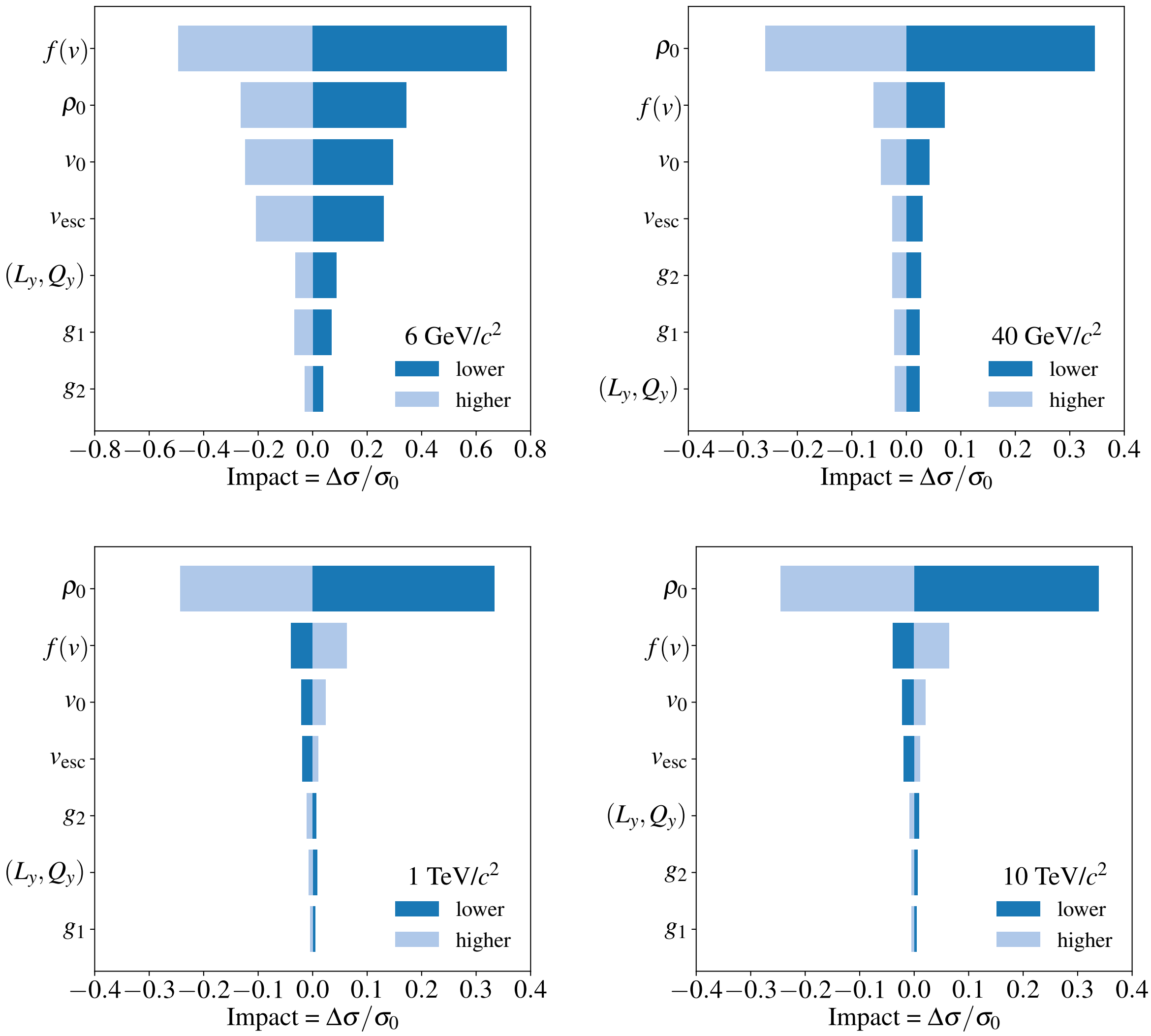

Figure 5.4: Ranking of the impact of different model parameters on the projected LZ sensitivity to SI WIMP-nucleon interactions. The impact of a given parameter when its value is decreased by the uncertainty given in Table 5.2 is plotted in dark blue, while the opposite case is represented in light blue. Astrophysical parameters dominate the ranking for all WIMP masses, and the largest impacts are found for the 6 GeV/c^2 case.

value of the projected limit, $\mu_s^{90\%}$, but it introduces a direct shift of 30% in the integrated rate in the denominator. Consequently, a 30% decrease in the DM density will have a larger impact on $\sigma_N^{90\%}$ than an increase by the same percentage. By contrast, this asymmetry is not expected to happen for relative impacts lower than 5%.

The results from Figure 5.4 show that there are a few model parameters which should be especially considered to be included in the LZ likelihood as nuisance parameters. Firstly, the local dark matter density is ranked first for all the WIMP masses that were considered. This is not surprising, as ρ_0 acts as a scaling factor and it has the largest uncertainty. A new nuisance parameter could be created, θ_ρ, which acts as a scaling factor on the signal mean in the likelihood,

$$\mu_s f_s(\boldsymbol{x}_e|m_\chi) \to (\mu_s\theta_\rho) f_s(\boldsymbol{x}_e|m_\chi). \tag{5.5}$$

Such parameter would have an initial value of 1, and would be constrained by a Gaussian with a relative width of 30%. However, and given the degeneracy between μ_s and ρ_0, it is important to stress that the procedure above would only add an extra uncertainty to μ_s, rather than treating ρ_0 as an independent parameter.

Secondly, the DM velocity distribution $(f(v))$ also scores highly in the raking for all WIMP masses. This is part of the more difficult class of model parameters called "shape-varying" parameters, as mentioned earlier. The standard procedure of generating a new PDF every time that a new parameter value is explored can be prohibitively time-consuming. One possible solution to mitigate this handicap, which is extensively used by LHC experiments [263], is to divide the observable space in equally-spaced bins and for each bin evaluate the PDF under nominal assumptions as well as some extreme cases of the shape-varying parameter. Then, the PLR analysis will rely on the linear interpolation between these points for each bin, instead of having to regenerate the corresponding PDF each time. However, note that this method becomes quickly unfeasible with an increased number of observables (since the number of bins grows as $\mathcal{O}(N^D)$ for D observables with N bins each). Another alternative would be to create a "catalogue" of PDFs for a large collection of model parameters so that the PDF generation step is replaced by a searching task in some large data base.

Also, the circular velocity (v_0) has a moderately high impact and, as shown earlier, it plays a more important role than the escape velocity (v_{esc}) for all WIMP masses except the lowest one, for which the effect is similar. Therefore, this is another shape-varying parameter that should be considered for addition into the list of nuisance parameters.

Should the number of shape-varying parameters be significant (probably more than a couple), then a suitable avenue to tackle the increase of computational time is to conduct a Bayesian analysis (instead of a frequentist PLR analysis). In a Bayesian analysis there is no distinction between the parameters of interest and the nuisance parameters: all of them are treated equally during the construction of the Markov chain. More importantly, only one single evaluation of the likelihood on the input data is required every time that a new point of the multi-dimensional space is explored. By contrast, in a frequentist PLR analysis several evaluations of the likelihood are needed during the two maximisations that are required to calculate the PLR test statistic.[1] If the evaluation of the likelihood is a computationally expensive operation, as in the case for a likelihood including several shape-varying parameters, then a Bayesian analysis might be the only feasible option. Finally, the Markov chain data can also be used to study the correlations between the different model parameters. A correlation matrix of all the model parameters based on the Pearson correlation coefficient is straightforward to obtain from the chain data, and it can provide valuable information as more nuisance parameters are considered.

It is worth noting that the three detector uncertainties that were considered in this study have a relative impact lower than 10% for all WIMP masses. The largest impacts are observed in the case of the $6\,\mathrm{GeV}/\mathrm{c}^2$ WIMP, but even then they score the lowest in the impact ranking since the astrophysical uncertainties also have the largest impacts at this mass. This generally low impact is mainly caused by the fact that an increase in the g_1 or g_2 factors, or the LXe yields, will not only increase the signal expectation but the background too.

In conclusion, we have identified that the astrophysical parameters ρ_0, $f(v)$ and v_0 have the largest impact on the LZ sensitivity to WIMPs—out of the list of parameters we considered which, although not being exhaustive, it is expected to include the leading sources of uncertainty if the experiment performs as designed. The uncertainty in ρ_0 is directly translated into the sensitivity projection, while smaller impacts are observed for the other two parameters for all WIMP masses except for the lightest WIMP, for which the impacts are the most significant. Given the high computational cost of adding shape-varying parameters into the likelihood function for the PLR method, the procedure described in this section becomes an essential tool to guide the effort of accounting for systematic uncertainties.

Next, we explore the effect that some of the most of impactful astrophysical parameters might have on the reconstruction of the parameter of interest in the case of a discovery.

[1] As Eq. (4.10) shows, two independent maximisation of the likelihood are needed for each PLR evaluation: one for the numerator and another one for the denominator.

5.3 Impact of systematics on cross section reconstruction

In essence, the observation of an excess of events after region-of-interest and other analysis cuts have been applied, and in a region where all the background sources are well-characterised, will result in a low p-value of the background-only hypothesis that serves as the basis for further assessments against the signal hypotheses and possibly claim the discovery of a new signal. In such fortunate situation, the LZ experiment will have the ability to reconstruct some key WIMP properties, for instance, the particle mass, the scattering cross section with ordinary matter or the spin nature of the interaction.

However, one must take into consideration that this reconstruction of WIMP parameters is sometimes subject to large systematic uncertainties, and in the case of astrophysical uncertainties this can lead to a significant mischaracterisation of the true WIMP properties (see e.g. Refs. [264, 257]). Indeed, the reconstruction of WIMP properties from nuclear recoil data has been extensively studied in the literature. For instance, Ref. [265] introduced a Bayesian method to infer WIMP properties that includes an explicit model of the dark matter halo. Conversely, Ref. [266] studied the systematic bias in the reconstruction of the WIMP's mass and scattering cross section caused by deviations from the standard Mawellian velocity distribution, while Ref. [264] explored the limitations in this reconstruction introduced by unavoidable statistical fluctuations in the recoil energy distribution.

A different approach is followed in the present work. Instead of assuming a generic dark matter detector with some idealised properties, as it is usually done in the studies mentioned above, we will retain the complexity of the LZ detector system that has been described in the introductory chapters, and explore the influence of some systematic uncertainties on the ability of the LZ experiment to reconstruct the WIMP scattering cross section. We expand the use of the PLR method shown so far, and we demonstrate some of the reconstruction capabilities of this technique.

We will take a few benchmark points from the 3σ discovery significance projection that was shown in Figure 4.12, and treat them as the "true" WIMP properties. These points are high enough compared to the LZ sensitivity projection that is shown in Figure 4.10 so that $\mathcal{O}(10)$ signal-like event are expected to arise in the respective signal regions over repeated experiments. The mass and cross section of the three points considered are listed in Table 5.4, along with the corresponding true signal mean, μ_s^{true}.

An example of a simulated data set of the LZ experiment with some added signal events based on the second benchmark point is shown in Figure 5.5. The same ER and NR bands that were calculated in Chapter 3 are shown in blue and red, respectively. The events at the bottom

Table 5.4: Benchmark points in the SI WIMP parameter space that are considered as the "true" WIMP properties in the reconstruction bias study. They are taken from the 3σ discovery significance projection in Figure 4.12. The corresponding expected signal mean is given in the last column.

WIMP mass (GeV/c^2)	$\sigma_N^{3\sigma}$ (cm^2)	μ_s^{true}
6	2.92×10^{-45}	21.3
40	2.98×10^{-48}	11.0
1000	3.93×10^{-47}	13.9

left correspond most probably to ^{8}B neutrino scatters, while most of the events along the blue band are a particular realisation of the ER background components that were listed in Table 3.3. In that table an estimation of the number of counts was given for the main background sources based on a cut-and-count analysis; we concluded that approximately 3 background events are expected below the median of the NR band (assuming a 99.8% ER discrimination). In this realisation, 8 events are observed below the NR median at nuclear recoil energies between 6 and 30 keV, which are the bounds considered in Table 3.3. Approximately, this entails $8-3=5$ signal counts below the median, or 10 counts for full acceptance, which is close to the true mean of 11.0.

Naively, and for a Poisson process with no added systematic uncertainty, the p-value of such observation would be

$$\begin{aligned} p_0 &= \sum_{n=8}^{\infty} \text{Pois}(n|b=3) \\ &= 1 - \sum_{n=0}^{8} \text{Pois}(n|b=3) \\ &= 3.8 \times 10^{-3} \end{aligned} \tag{5.6}$$

which corresponds to a 2.6σ discovery significance. Although this is tantalisingly close to 3σ, it is not large enough to be able to claim an *observation*. Alternatively, we can use the PLR method to make a more accurate characterisation of the data shown in Figure 5.5, using the shape information of each of the PDF components instead of relying on a crude cut-and-count estimation. The top panel of Figure 5.6 shows the result of a hypothesis test that uses the q_0 test statistic, defined in Eq. (4.16), to assess the compatibility of the observed data with the $\mu_s = 0$ hypothesis. The null p-value according to this test is 8.15×10^{-4} from the Monte Carlo distribution (in red) and 8.20×10^{-4} from the asymptotic formula (in magenta). These two p-values correspond to a discovery significance of 3.2σ, indicating that an *observation* can indeed be claimed from this data set.

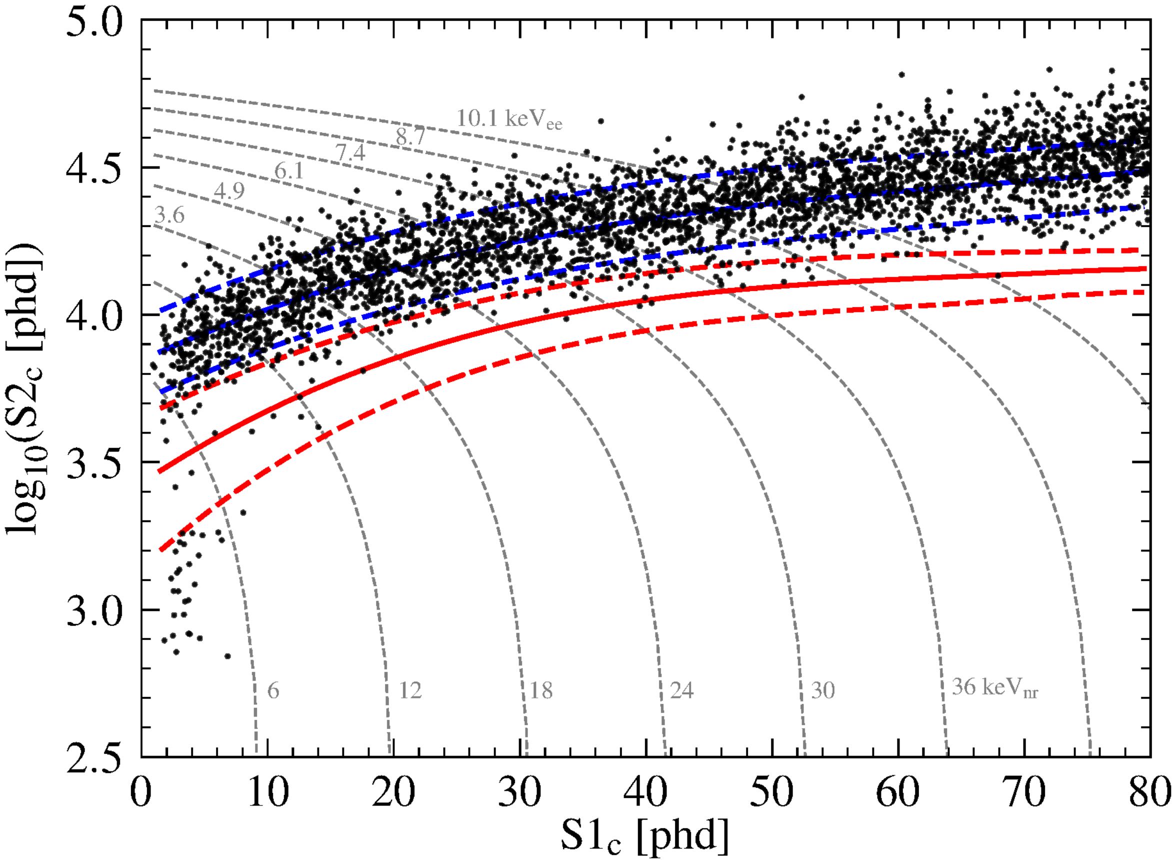

Figure 5.5: Simulated data set for a possible realisation of the LZ experiment in which both background and signal events have been added. The complete exposure of 1000 live days of a 5.6-tonne fiducial mass is assumed. The number of signal events is generated following a Poisson process with mean given by the second benchmark point in Table 5.4. The ER and NR bands that were calculated in Section 3.3.2 are shown in blue and red, respectively. The events at the bottom left most likely correspond to ^{8}B neutrino scatters.

Once a discovery is established, we might be interested in knowing which WIMP parameter values are mostly favoured by the experimental observation. As an example, let us fix the WIMP mass to the value of 40 GeV/c^2 and discuss how we would constrain the scattering cross section. The lower panel of Figure 5.6 shows the p-value plot returned by `LZStats` from another frequentist analysis on the same data set, this time using a two-sided PLR test statistic (t_μ), defined in Eq. (4.11). The first test values of the parameter of interest, μ_s, are much smaller than the global maximum likelihood estimator on data, $\hat{\mu}_s$, which would be close to the number of WIMP-like events that were added to the data set. Consequently, the value of the observed test statistic, $t_{\mu,\mathrm{obs}}$, will be large, and the corresponding null p-value low, as we can see at the beginning of this plot. As the hypothesised value of μ_s approaches the best-fit value $\hat{\mu}_s$, the numerator and denominator in (4.10) become similar and $t_{\mu,\mathrm{obs}}$ gets closer to 0, resulting in a large p-value. Then, as larger values of μ_s are tested, $t_{\mu,\mathrm{obs}}$ increases again and the observed p-value decreases gradually. This explains the shape of the solid line in Figure 5.6, which peaks near 12. The red line indicates the p-value equivalent to a 68.3% CL (1σ), and the points where it crosses the solid black line determine the bounds of the corresponding two-sided confidence interval. In this case, we obtain

$$\mu_s \in [8.3, 18.4] \quad (68.3\%\ \mathrm{CL}). \tag{5.7}$$

Equivalently, the confidence interval on the SI WIMP-nucleon scattering cross section applying the conversion factor shown in Eq. (5.4) is

$$\sigma_N^{\mathrm{SI}} \in [2.2, 5.0] \times 10^{-48}\ \mathrm{cm}^2 \quad (68.3\%\ \mathrm{CL}), \tag{5.8}$$

which covers the true value given in Table 5.4.

Next, we study the effect that the most impactful parameters that were identified in the previous section have on the reconstruction procedure described above. For a given benchmark point, we generate several mock data sets assuming the nominal conditions summarised in Table 5.2. We apply the above procedure to derive a confidence interval on the signal mean (μ_s) for each simulated data set. As we are mainly interested in identifying the putative bias introduced by the systematic uncertainty, we will take the central point of the confidence interval as a representative measure and study variations on this parameter.

Then, we analyse the same mock data sets but fixing one of the model parameters to a pessimistic assumption. 400 pseudo-experiments are considered each time and the results are shown in Figure 5.7. Each row corresponds to one of the WIMP masses in Table 5.4, for which two astrophysical parameters are considered. The dark matter velocity distribution

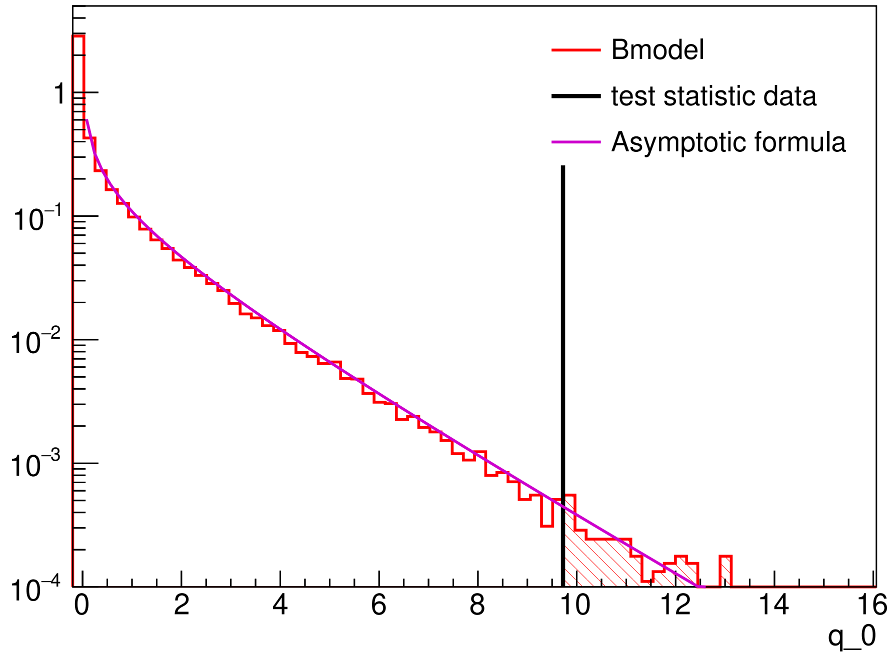

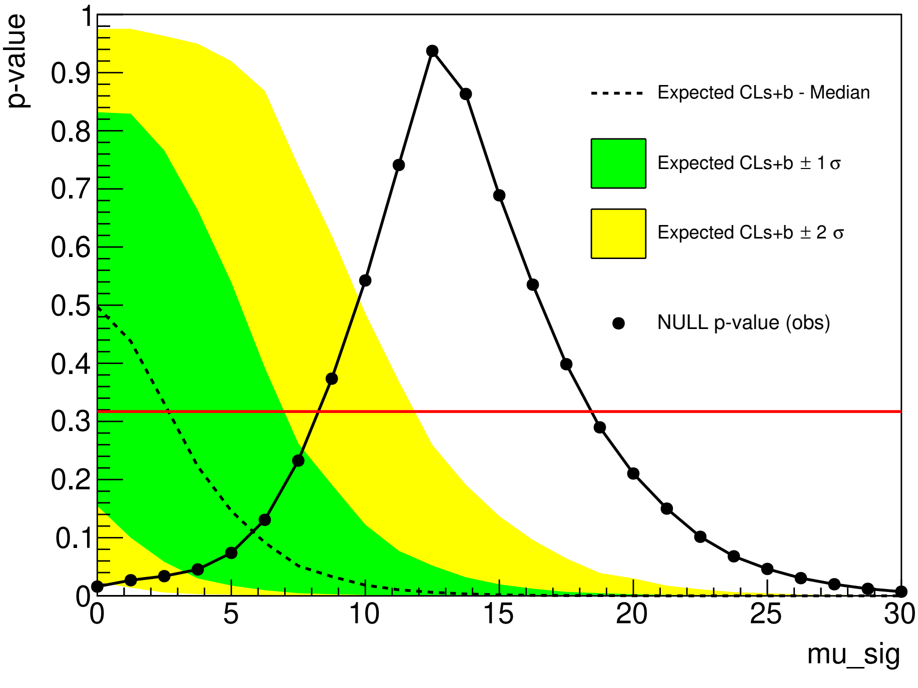

Figure 5.6: Results from two frequentist hypothesis tests on the mock data set shown in Figure 5.5. *Above:* Discovery test using the q_0 statistic to test the observed data against the background only hypothesis ($\mu_s = 0$). This result corresponds to a 3.2σ discovery significance. *Below:* Frequentist hypothesis test using a two-sided PLR test statistic (t_μ). The expected null p-value (dashed line) decreases with increasing values of the hypothesised signal mean, while the observed p-value (solid line) increases until the test POI value (μ_s) is similar to the global best-fit value ($\hat{\mu}_s$), and then decreases back to zero. The crossings between the horizontal red line and the solid black line determines the boundaries of the confidence interval on the parameter of interest at 68.3% CL (1σ).

is chosen for all three masses, and the escape velocity is explored for the lightest WIMP, while the local circular velocity is explored for the other two WIMP masses. The Necib *et al.* model is considered the pessimistic scenario for the dark matter velocity distribution, while the lower values of 490 km/s and 198 km/s are assumed for the escape and local circular velocity, respectively, which corresponds to a 10% decrease from their nominal values. We omit the local dark matter density from this study since it is expected to play a negligible effect on the PLR fits.

The reconstructed values for the nominal case are shown in the filled grey histogram, while the distribution of values with the more pessimistic model is shown by an empty blue histogram. The median of each of the distributions is shown with a black or blue dashed line, respectively. We observe that the difference between the two median lines is very small in all cases, indicating that the two distributions are statistically equivalent. However, this does not necessarily imply that there is no bias in this reconstruction procedure, but rather that the systematic uncertainty is sub-dominant with respect to the statistical uncertainty (for the assumed bechmark points). A root mean square (RMS) of 8.8, 12.3 and 10.5 counts is obtained for the nominal distributions of the 6, 40 and 1000 $\mathrm{GeV/c^2}$ WIMP masses, respectively. This corresponds to a relative uncertainty with respect to the median of these distributions of 41%, 115% and 77%, respectively, which would dominate over any of the systematic uncertainties that we studied in this chapter.

To conclude, we note that the effect of the highest-ranked astrophysical uncertainties should also be studied on the joined reconstruction of WIMP mass and cross section, since the systematic uncertainty might play a more important role in that case. However, such calculation needs to be undertaken with care, since it was observed that already using two observables (S1 and S2) and two parameters of insterest (m_χ and σ_N) makes the standard PLR analysis prohibitively slow. Some possible solutions to tackle this problem have been discussed in Section 5.2, and there is an ongoing effort inside the LZ collaboration to find the most suitable solution.

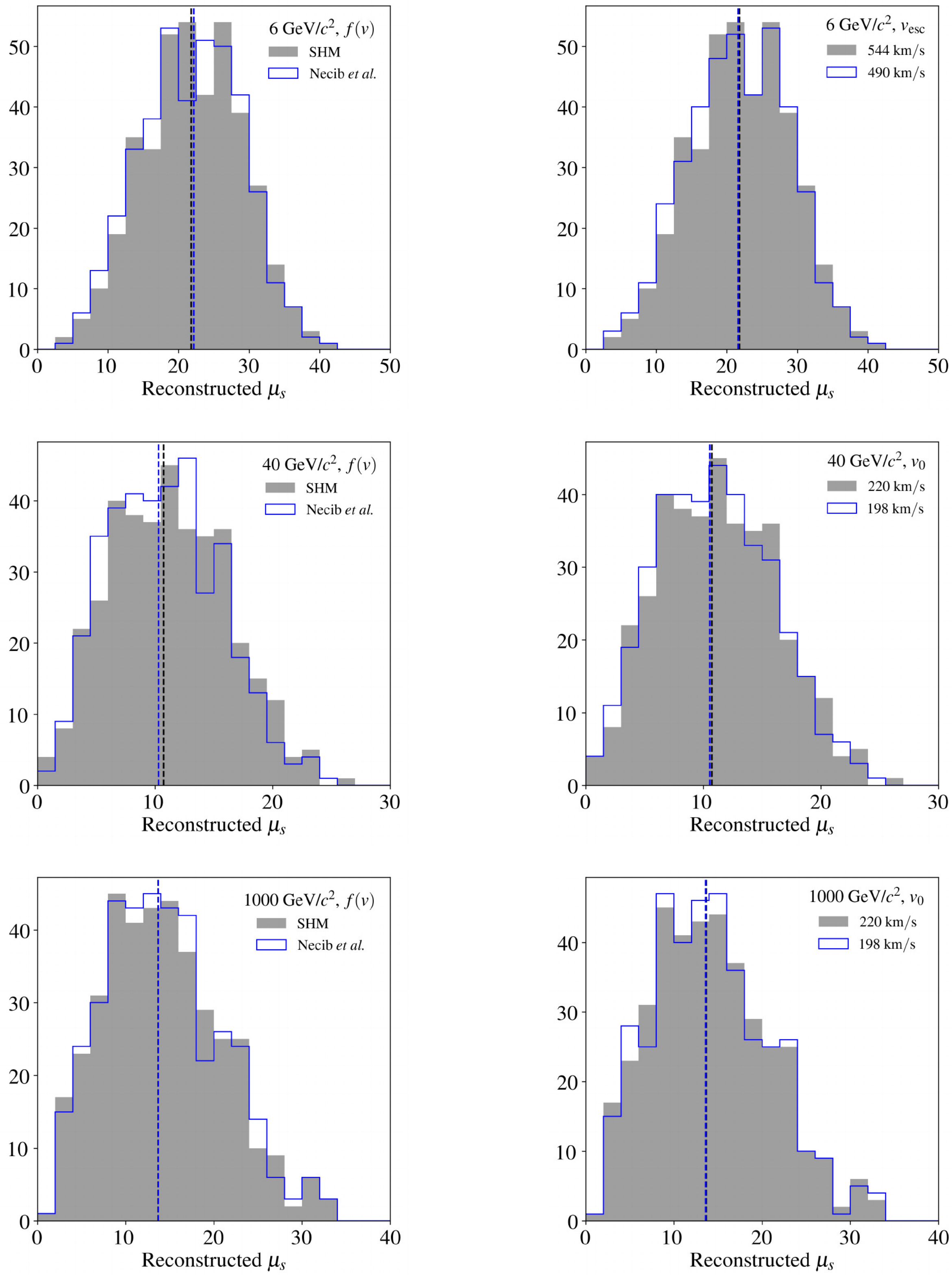

Figure 5.7: Distribution of reconstructed values of the parameter of interest (μ_s) over repeated experiments under two different model assumptions: nominal (filled black), and pessimistic prediction (blue contour). The same mock data sets are used in both cases, which are always generated under the nominal settings. The black and blue dashed lines indicate the median of each distribution, respectively. No statistically significant difference is observed with respect to the nominal case, indicating that the systematic uncertainty is sub-dominant.

Chapter 6

Conclusions

Despite the strong evidence favouring the hypothesis that most of the mass in the universe is composed of dark matter, the nature of this elusive substance remains unknown. A particle interpretation is favoured, but the Standard Model of particle physics does not contain any suitable particle that could account for it. Many particle candidates from theories beyond the Standard Model have been proposed, and in Chapter 2 we discussed three that have received a great deal of attention: WIMPs, axions and sterile neutrinos. WIMP is a class of particle that is particularly attractive, as any new particle with interactions at the weak scale would be thermally produced with the right relic abundance.

The work presented in this thesis focuses on LUX-ZEPLIN (LZ), a liquid xenon experiment now in the final stages of construction which is planned to start operating in 2020, and whose main characteristics were described in Chapter 3. The sensitivity of LZ to WIMP elastic scattering depends on a large number of experimental, astrophysical and other parameters, and its results will require careful data analysis. Eventually, a statistical analysis applied to the highest level data quantities must determine if the experimental observation is compatible with the background-only hypothesis or if, more excitingly, they support a discovery claim. The statistical framework developed for this purpose is the main topic of this thesis, and we described its use to assess the sensitivity of the experiment for limit-setting and discovery significance in Chapter 4.

We showed that LZ will be able to achieve a 3σ discovery for a spin-independent cross section above $3.0 \times 10^{-48}\,\mathrm{cm}^2$ at $40\,\mathrm{GeV/c}^2$ or exclude a cross section of $1.3 \times 10^{-48}\,\mathrm{cm}^2$ (at 90% CL) in the absence of signal. Sensitivity projections for spin-dependent WIMP-proton and WIMP-neutron scattering were also given. We compared these to previous projections shown in both the LZ TDR [1] and the LZ WIMP sensitivity paper [2], and we identified that the observed differences are mainly due to the improved estimated value of the PTFE reflectivity, based on the new measurements from Ref. [210], and to the upgrade of the NEST software (from libNEST `5.0.0` to NEST `v2.0.0`).

As LZ will be exploring increasingly lower cross sections, two different methods to prevent the exclusion of a parameter point to which one has little experimental sensitivity were discussed: the $\mathrm{CL_s}$ method and power-constrained limits. It was concluded that power-constrained limits are preferred for their superior coverage properties. Nevertheless, this is a topic of intense debate within the direct detection community at the moment and this, as well as other topics such as which is the best test statistic to use for limit-setting (see the main choices in Section 4.2), will hopefully be commonly agreed on soon. An important step forward in this direction was taken in the PHYSTAT Dark Matter workshop at Stockholm in the summer of 2019, which triggered the creation of a white paper on recommended statistical procedures for direct detection experiments (currently in preparation). The work presented in this thesis contributes to that discussion.

In Chapter 5 we reviewed some key systematic uncertainties and studied both their impact on WIMP sensitivity and their effect on the reconstruction of the WIMP cross section. We concluded that the local dark matter density (ρ_0), the local circular velocity (v_0) and the dark matter velocity distribution $(f(v))$ have the largest impact on WIMP sensitivity, while the experimental parameters g_1 and g_2, and the LXe yields are less impactful for their assumed uncertainties. The impact of the uncertainties in the nuclear parameters, such as form factors or spin structure functions, was not included in this study due to time constraints but it should be emphasised that their effect could also be significant. This point should be addressed in future studies of a similar type.

Including ρ_0 in the list of nuisance parameters would be trivial, but all the others are shape-varying parameters and accounting for their uncertainty can be computationally expensive. There are methods to reduce the computational cost, such as having a linear interpolation of the model available bin per bin or creating a catalogue of PDFs for different parameter values, and all these different options are currently being explored by the LZ collaboration. Alternatively, switching to a Bayesian analysis might be wise—and indeed the only viable option— if more than a handful shape-varying parameters are considered. This is because of the lower number of likelihood evaluations required to generate the Markov chain (compared to the PLR method), and the vast resources that currently exist in terms of algorithms and scientific libraries to explore the multi-dimensional parameter space efficiently. Also, a Bayesian analysis can more easily provide information about any existing correlations between the different model parameters.

Furthermore, it was found that the systematic uncertainty of the highest-ranked astrophysical parameters is sub-dominant in the reconstruction of the WIMP scattering cross section. This study should be extended to the joint reconstruction of both mass and cross section to assess if the statistical uncertainty is dominant in this case as well. Although we focused our discussion on the S1 and S2 observables in this thesis, it should be emphasised that the inclusion of other observables is needed in order to characterise the experimental data fully. The spatial variables (x,y,z) or (r,z)—that is, radius and depth—are prime choices, but other non-standard observables such as the S1 and S2 pulse shapes should be taken into consideration too.

With the LZ experiment almost at the end of its construction phase, and with the opening up of parameter space with radically different technologies, there is a tangible possibility that a WIMP detection could be made in the coming years. These *are* exciting times.

Bibliography

[1] **LZ** Collaboration, B. J. Mount *et al.*, "LUX-ZEPLIN (LZ) Technical Design Report," arXiv:1703.09144 [physics.ins-det].

[2] **LZ** Collaboration, D. S. Akerib *et al.*, "Projected WIMP Sensitivity of the LUX-ZEPLIN (LZ) Dark Matter Experiment," arXiv:1802.06039 [astro-ph.IM].

[3] F. Zwicky, "Die Rotverschiebung von extragalaktischen Nebeln," *Helv. Phys. Acta* **6** (1933) 110–127.

[4] G. Bertone and D. Hooper, "History of dark matter," *Rev. Mod. Phys.* **90** no. 4, (2018) 045002, arXiv:1605.04909 [astro-ph.CO].

[5] S. Smith, "The Mass of the Virgo Cluster," *Astrophys. J.* **83** (1936) 23–30.

[6] E. Holmberg, "On the Clustering Tendencies among the Nebulae," *Astrophys. J.* **92** (1940) 200.

[7] J. Einasto, *Dark Matter and Cosmic Web Story*. World Scientific Publishing Co, 2014.

[8] H. I. Ewen and E. M. Purcell, "Observation of a Line in the Galactic Radio Spectrum: Radiation from Galactic Hydrogen at 1,420 Mc./sec," *Nature* **168** (1951) 356.

[9] V. C. Rubin and W. K. Ford, Jr., "Rotation of the Andromeda Nebula from a Spectroscopic Survey of Emission Regions," *Astrophys. J.* **159** (1970) 379.

[10] A. Bosma, *The distribution and kinematics of neutral hydrogen in spiral galaxies of various morphological types*. PhD thesis, Groningen Univ., 1978.

[11] V. C. Rubin, W. K. Ford, Jr., and N. Thonnard, "Extended rotation curves of high-luminosity spiral galaxies. IV - Systematic dynamical properties, SA through SC," *Astrophys. J. L.* **225** (1978) L107–L111.

[12] S. T. Gottesman and R. D. Davies, "Neutral hydrogen in M31 - II. The dynamics and kinematics of M31," *Mon. Not. R. Astron. Soc.* **149** (1970) 263–290.

[13] M. S. Roberts and R. N. Whitehurst, "The rotation curve and geometry of M31 at large galactocentric distances," *Astrophys. J.* **201** (1975) 327–346.

[14] M. Milgrom, "A modification of the Newtonian dynamics as a possible alternative to the hidden mass hypothesis," *Astrophys. J.* **270** (1983) 365–370.

[15] M. Milgrom, “A modification of the Newtonian dynamics - Implications for galaxies,” *Astrophys. J.* **270** (1983) 371–389.

[16] J. D. Bekenstein, “Relativistic gravitation theory for the MOND paradigm,” *Phys. Rev. D* **70** (2004) 083509, `arXiv:astro-ph/0403694 [astro-ph]`. [Erratum: Phys. Rev.D71,069901(2005)].

[17] H. Hoekstra *et al.*, “Masses of galaxy clusters from gravitational lensing,” *Space Sci. Rev.* **177** (2013) 75–118, `arXiv:1303.3274 [astro-ph.CO]`.

[18] D. Clowe *et al.*, “A direct empirical proof of the existence of dark matter,” *Astrophys. J.* **648** (2006) L109–L113, `arXiv:astro-ph/0608407 [astro-ph]`.

[19] **LIGO and Virgo** Collaboration, B. P. Abbott *et al.*, “GW170817: Observation of Gravitational Waves from a Binary Neutron Star Inspiral,” *Phys. Rev. Lett.* **119** (2017) 161101.

[20] M. Ajello *et al.*, “Fermi-LAT observations of LIGO/virgo event GW170817,” *Astrophys. J.* **861** no. 2, (2018) 85.

[21] H. Wang *et al.*, “The GW170817/GRB 170817A/AT 2017gfo Association: Some Implications for Physics and Astrophysics,” *Astrophys. J.* **851** no. 1, (2017) L18.

[22] J. Sakstein and B. Jain, “Implications of the Neutron Star Merger GW170817 for Cosmological Scalar-Tensor Theories,” *Phys. Rev. Lett.* **119** (2017) 251303.

[23] R. H. Dicke, P. J. E. Peebles, P. G. Roll, and D. T. Wilkinson, “Cosmic Black-Body Radiation.,” *Astrophys. J.* **142** (1965) 414–419.

[24] A. A. Penzias and R. W. Wilson, “A Measurement of Excess Antenna Temperature at 4080 Mc/s.,” *Astrophys. J.* **142** (1965) 419–421.

[25] D. J. Fixsen *et al.*, “The Cosmic Microwave Background spectrum from the full COBE FIRAS data set,” *Astrophys. J.* **473** (1996) 576, `arXiv:astro-ph/9605054 [astro-ph]`.

[26] G. Hinshaw *et al.*, “Nine-year Wilkinson Microwave Anisotropy Probe (WMAP) Observations: Cosmological Parameter Results,” *Astrophys. J. S. S.* **208** no. 2, (2013) 19, `arXiv:1212.5226 [astro-ph.CO]`.

[27] **Planck** Collaboration, Y. Akrami *et al.*, “Planck 2018 results: I. Overview and the cosmological legacy of Planck,” `arXiv:1807.06205 [astro-ph.CO]`.

[28] **Planck** Collaboration, N. Aghanim *et al.*, “Planck 2018 results: VI. Cosmological parameters,” `arXiv:1807.06209 [astro-ph.CO]`.

[29] D. H. Weinberg, M. J. Mortonson, D. J. Eisenstein, C. Hirata, A. G. Riess, and E. Rozo, “Observational probes of cosmic acceleration,” *Phys. Rep.* **530** no. 2, (2013) 87–255.

[30] **Particle Data Group** Collaboration, C. Patrignani *et al.*, “Review of Particle Physics,” *Chin. Phys. C* **40** no. 10, (2016) 100001.

[31] S. Burles, K. M. Nollett, and M. S. Turner, "Big bang nucleosynthesis predictions for precision cosmology," *Astrophys. J.* **552** (2001) L1–L6, arXiv:astro-ph/0010171 [astro-ph].

[32] R. J. Cooke, M. Pettini, and C. C. Steidel, "One Percent Determination of the Primordial Deuterium Abundance," *Astrophys. J.* **855** no. 2, (2018) 102, arXiv:1710.11129 [astro-ph.CO].

[33] M. Davis, J. Huchra, D. W. Latham, and J. Tonry, "A survey of galaxy redshifts. II - The large scale space distribution," *Astrophys. J.* **253** (1982) 423–445.

[34] M. Davis, G. Efstathiou, C. S. Frenk, and S. D. M. White, "The evolution of large-scale structure in a universe dominated by cold dark matter," *Astrophys. J.* **292** (1985) 371–394.

[35] J. F. Navarro, C. S. Frenk, and S. D. M. White, "The Structure of cold dark matter halos," *Astrophys. J.* **462** (1996) 563–575, arXiv:astro-ph/9508025 [astro-ph].

[36] V. Springel *et al.*, "Simulations of the formation, evolution and clustering of galaxies and quasars," *Nature* **435** (2005) 629–636, astro-ph/0504097.

[37] M. Vogelsberger *et al.*, "Introducing the Illustris Project: simulating the coevolution of dark and visible matter in the Universe," *Mon. Not. R. Astron. Soc.* **444** no. 2, (2014) 1518–1547.

[38] P. Tisserand *et al.*, "Limits on the Macho Content of the Galactic Halo from the EROS-2 Survey of the Magellanic Clouds," *Astronom. & Astrophys.* **469** (2007) 387–404, arXiv:astro-ph/0607207 [astro-ph].

[39] B. J. Carr and S. W. Hawking, "Black Holes in the Early Universe," *Mon. Not. R. Astron. Soc.* **168** no. 2, (1974) 399–415.

[40] B. Carr, F. Kuhnel, and M. Sandstad, "Primordial Black Holes as Dark Matter," *Phys. Rev. D* **94** no. 8, (2016) 083504, arXiv:1607.06077 [astro-ph.CO].

[41] B. W. Lee and S. Weinberg, "Cosmological lower bound on heavy-neutrino masses," *Phys. Rev. Lett.* **39** (1977) 165–168.

[42] J. E. Gunn, B. W. Lee, I. Lerche, D. N. Schramm, and G. Steigman, "Some astrophysical consequences of the existence of a heavy stable neutral lepton," *Astrophys. J.* **223** (1978) 1015–1031.

[43] Ya. B. Zeldovich, A. A. Klypin, M. Yu. Khlopov, and V. M. Chechetkin, "Astrophysical constraints on the mass of heavy stable neutral leptons," *Sov. J. Nucl. Phys.* **31** (1980) 664–669.

[44] S. D. M. White, C. S. Frenk, and M. Davis, "Clustering in a neutrino-dominated universe," *Astrophys. J. L.* **274** (1983) L1–L5.

[45] G. Steigman and M. S. Turner, "Cosmological constraints on the properties of weakly interacting massive particles," *Nucl. Phys. B* **253** (1985) 375–386.

[46] G. Jungman, M. Kamionkowski, and K. Griest, "Supersymmetric dark matter," *Phys. Rept.* **267** (1996) 195–373, arXiv:hep-ph/9506380 [hep-ph].

[47] K. Petraki and R. R. Volkas, "Review of asymmetric dark matter," *Int. J. Mod. Phys. A* **28** (2013) 1330028, arXiv:1305.4939 [hep-ph].

[48] K. M. Zurek, "Asymmetric Dark Matter: Theories, Signatures, and Constraints," *Phys. Rep.* **537** (2014) 91–121, arXiv:1308.0338 [hep-ph].

[49] **ATLAS** Collaboration, G. Aad *et al.*, "Observation of a new particle in the search for the Standard Model Higgs boson with the ATLAS detector at the LHC," *Phys. Lett. B* **716** (2012) 1–29, arXiv:1207.7214 [hep-ex].

[50] **CMS** Collaboration, S. Chatrchyan *et al.*, "Observation of a New Boson at a Mass of 125 GeV with the CMS Experiment at the LHC," *Phys. Lett. B* **716** (2012) 30–61, arXiv:1207.7235 [hep-ex].

[51] P. Athron *et al.*, "Global fits of gut-scale susy models with gambit," *Eur. Phys. J. C* **77** no. 12, (2017) 824.

[52] J. C. Costa *et al.*, "Likelihood Analysis of the Sub-GUT MSSM in Light of LHC 13-TeV Data," *Eur. Phys. J. C* **78** no. 2, (2018) 158, arXiv:1711.00458 [hep-ph].

[53] G. G. Ross, K. Schmidt-Hoberg, and F. Staub, "Revisiting fine-tuning in the MSSM," *JHEP* **03** no. 3, (2017) 21.

[54] T. Flacke, D. W. Kang, K. Kong, G. Mohlabeng, and S. C. Park, "Electroweak Kaluza-Klein dark matter," *JHEP* **2017** no. 4, (2017) 41.

[55] E. W. Kolb, D. J. H. Chung, and A. Riotto, "WIMPZILLAS!," *AIP Conference Proceedings* **484** no. 1, (1999) 91–105.

[56] C. A. Baker *et al.*, "Improved experimental limit on the electric dipole moment of the neutron," *Phys. Rev. Lett.* **97** (2006) 131801.

[57] H.-Y. Cheng, "The strong CP problem revisited," *Phys. Rep.* **158** (1988) 1–89.

[58] R. D. Peccei and H. R. Quinn, ""CP conservation in the presence of pseudoparticles"," *Phys. Rev. Lett.* **38** (1977) 1440–1443.

[59] R. D. Peccei and H. R. Quinn, ""constraints imposed by CP conservation in the presence of pseudoparticles"," *Phys. Rev. D* **16** (1977) 1791–1797.

[60] F. Wilczek, ""problem of strong p and t invariance in the presence of instantons"," *Phys. Rev. Lett.* **40** (1978) 279–282.

[61] S. Weinberg, "A New Light Boson?," *Phys. Rev. Lett.* **40** (1978) 223–226.

[62] F. Wilczek. http://www.garfield.library.upenn.edu/classics1991/A1991FE76900001.pdf.

[63] J. Preskill, M. B. Wise, and F. Wilczek, "Cosmology of the invisible axion," *Phys. Lett. B* **120** no. 1, (1983) 127–132.

[64] M. Archidiacono, S. Hannestad, A. Mirizzi, G. Raffelt, and Y. Y. Y. Wong, "Axion hot dark matter bounds after Planck," *J. Cosmol. Astropart. Phys.* **1310** (2013) 020, arXiv:1307.0615 [astro-ph.CO].

[65] M. Dine and W. Fischler, "The Not So Harmless Axion," *Phys. Lett. B* **120** (1983) 137–141.

[66] L. Abbott and P. Sikivie, "A cosmological bound on the invisible axion," *Phys. Rev. B* **120** no. 1, (1983) 133–136.

[67] M. Tanabashi *et al.*, "Review of Particle Physics," *Phys. Rev. D* **98** no. 3, (2018) 030001.

[68] L. J. Rosenberg and K. A. van Bibber, "Searches for invisible axions," *Phys. Rep.* **325** (2000) 1–39.

[69] **ADMX** Collaboration, N. Du *et al.*, "A Search for Invisible Axion Dark Matter with the Axion Dark Matter Experiment," *Phys. Rev. Lett.* **120** no. 15, (2018) 151301, arXiv:1804.05750 [hep-ex].

[70] **CAST** Collaboration, V. Anastassopoulos *et al.*, "New CAST Limit on the Axion-Photon Interaction," *Nature Phys.* **13** (2017) 584–590, arXiv:1705.02290 [hep-ex].

[71] **OSQAR** Collaboration, R. Ballou *et al.*, "New exclusion limits on scalar and pseudoscalar axionlike particles from light shining through a wall," *Phys. Rev. D* **92** (2015) 092002.

[72] **ALPS** Collaboration, K. Ehret *et al.*, "New alps results on hidden-sector lightweights," *Phys. Lett. B* **689** no. 4, (2010) 149–155.

[73] **LUX** Collaboration, D. S. Akerib *et al.*, "First Searches for Axions and Axionlike Particles with the LUX Experiment," *Phys. Rev. Lett.* **118** no. 26, (2017) 261301, arXiv:1704.02297 [astro-ph.CO].

[74] N. Vinyoles *et al.*, "New axion and hidden photon constraints from a solar data global fit," *J. Cosmol. Astropart. Phys.* **1510** no. 10, (2015) 015, arXiv:1501.01639 [astro-ph.SR].

[75] A. Ayala, I. Domínguez, M. Giannotti, A. Mirizzi, and O. Straniero, "Revisiting the bound on axion-photon coupling from Globular Clusters," *Phys. Rev. Lett.* **113** no. 19, (2014) 191302, arXiv:1406.6053 [astro-ph.SR].

[76] N. Viaux *et al.*, "Neutrino and axion bounds from the globular cluster M5 (NGC 5904)," *Phys. Rev. Lett.* **111** (2013) 231301, arXiv:1311.1669 [astro-ph.SR].

[77] M. M. Miller Bertolami, B. E. Melendez, L. G. Althaus, and J. Isern, "Revisiting the axion bounds from the Galactic white dwarf luminosity function," *J. Cosmol. Astropart. Phys.* **1410** no. 10, (2014) 069, arXiv:1406.7712 [hep-ph].

[78] T. Fischer *et al.*, "Probing axions with the neutrino signal from the next galactic supernova," *Phys. Rev. D* **94** no. 8, (2016) 085012, arXiv:1605.08780 [astro-ph.HE].

[79] **H.E.S.S.** Collaboration, A. Abramowski *et al.*, "Constraints on axionlike particles with H.E.S.S. from the irregularity of the PKS 2155-304 energy spectrum," *Phys. Rev. D* **88** no. 10, (2013) 102003, arXiv:1311.3148 [astro-ph.HE].

[80] **Fermi-LAT** Collaboration, M. Ajello *et al.*, "Search for Spectral Irregularities due to Photon–Axionlike-Particle Oscillations with the Fermi Large Area Telescope," *Phys. Rev. Lett.* **116** no. 16, (2016) 161101, arXiv:1603.06978 [astro-ph.HE].

[81] S. Dodelson and L. M. Widrow, "Sterile-neutrinos as dark matter," *Phys. Rev. Lett.* **72** (1994) 17–20, arXiv:hep-ph/9303287 [hep-ph].

[82] R. Adhikari *et al.*, "A White Paper on keV sterile neutrino Dark Matter," *J. Cosmol. Astropart. Phys.* **2017** no. 01, (2017) 025–025.

[83] E. Bulbul, M. Markevitch, A. Foster, R. K. Smith, M. Loewenstein, and S. W. Randall, "Detection of an unidentified emission line in the stacked X-ray spectrum of galaxy clusters," *Astrophys. J.* **789** no. 1, (2014) 13.

[84] M. E. Anderson, E. Churazov, and J. N. Bregman, "Non-Detection of X-Ray Emission From Sterile Neutrinos in Stacked Galaxy Spectra," *Mon. Not. R. Astron. Soc.* **452** no. 4, (2015) 3905–3923, arXiv:1408.4115 [astro-ph.HE].

[85] E. Carlson, T. Jeltema, and S. Profumo, "Where do the 3.5 keV photons come from? A morphological study of the Galactic Center and of Perseus," *J. Cosmol. Astropart. Phys.* **1502** no. 02, (2015) 009, arXiv:1411.1758 [astro-ph.HE].

[86] M. Battaglieri *et al.*, "US Cosmic Visions: New Ideas in Dark Matter 2017: Community Report," in *U.S. Cosmic Visions: New Ideas in Dark Matter College Park, MD, USA, March 23-25, 2017*. 2017. arXiv:1707.04591 [hep-ph].

[87] S. Arrenberg *et al.*, "Working Group Report: Dark Matter Complementarity," in *Proceedings, 2013 Community Summer Study on the Future of U.S. Particle Physics: Snowmass on the Mississippi (CSS2013)*. arXiv:1310.8621 [hep-ph].

[88] J. R. Ellis, R. A. Flores, and J. D. Lewin, "Rates for Inelastic Nuclear Excitation by Dark Matter Particles," *Phys. Lett.* **B212** (1988) 375–380.

[89] L. Baudis, G. Kessler, P. Klos, R. F. Lang, J. Menéndez, S. Reichard, and A. Schwenk, "Signatures of Dark Matter Scattering Inelastically Off Nuclei," *Phys. Rev. D* **88** no. 11, (2013) 115014, arXiv:1309.0825 [astro-ph.CO].

[90] D. Tucker-Smith and N. Weiner, "The Status of inelastic dark matter," *Phys. Rev. D* **72** (2005) 063509, arXiv:hep-ph/0402065 [hep-ph].

[91] M. Lisanti and J. G. Wacker, "Parity Violation in Composite Inelastic Dark Matter Models," *Phys. Rev. D* **82** (2010) 055023, arXiv:0911.4483 [hep-ph].

[92] P. W. Graham, R. Harnik, S. Rajendran, and P. Saraswat, "Exothermic Dark Matter," *Phys. Rev. D* **82** (2010) 063512, arXiv:1004.0937 [hep-ph].

[93] J. D. Lewin and P. F. Smith, "Review of mathematics, numerical factors, and corrections for dark matter experiments based on elastic nuclear recoil," *Astropart. Phys.* **6** (1996) 87–112.

[94] L. Baudis, "Direct dark matter detection: the next decade," *Phys. Dark Univ.* **1** (2012) 94–108, arXiv:1211.7222 [astro-ph.IM].

[95] M. Szydagis *et al.*, "NEST: A Comprehensive Model for Scintillation Yield in Liquid Xenon," *JINST* **6** (2011) P10002, arXiv:arXiv:1106.1613 [physics.ins-det].

[96] P. Cushman *et al.*, "Snowmass CF1 Summary: WIMP Dark Matter Direct Detection," arXiv:1310.8327.

[97] **LUX** Collaboration, D. S. Akerib *et al.*, "Results from a search for dark matter in the complete LUX exposure," *Phys. Rev. Lett.* **118** no. 2, (2017) 021303, arXiv:1608.07648 [astro-ph.CO].

[98] **XENON** Collaboration, E. Aprile *et al.*, "Dark Matter Search Results from a One Ton-Year Exposure of XENON1T," *Phys. Rev. Lett.* **121** no. 11, (2018) 111302, arXiv:1805.12562 [astro-ph.CO].

[99] **XENON** Collaboration, E. Aprile *et al.*, "Physics reach of the XENON1T dark matter experiment," *J. Cosmol. Astropart. Phys.* **1604** no. 04, (2016) 027, arXiv:1512.07501 [physics.ins-det].

[100] **PandaX-II** Collaboration, X. Cui *et al.*, "Dark Matter Results From 54-Ton-Day Exposure of PandaX-II Experiment," *Phys. Rev. Lett.* **119** no. 18, (2017) 181302, arXiv:1708.06917 [astro-ph.CO].

[101] **SuperCDMS** Collaboration, R. Agnese *et al.*, "New Results from the Search for Low-Mass Weakly Interacting Massive Particles with the CDMS Low Ionization Threshold Experiment," *Phys. Rev. Lett.* **116** (2016) 071301.

[102] **SuperCDMS** Collaboration, R. Agnese *et al.*, "Results from the Super Cryogenic Dark Matter Search Experiment at Soudan," *Phys. Rev. Lett.* **120** (2018) 061802.

[103] **DarkSide** Collaboration, P. Agnes *et al.*, "Low-mass dark matter search with the darkside-50 experiment," *Phys. Rev. Lett.* **121** (2018) 081307.

[104] **LUX** Collaboration, D. S. Akerib *et al.*, "Extending light WIMP searches to single scintillation photons in LUX," arXiv:1907.06272 [astro-ph.CO].

[105] **DarkSide** Collaboration, P. Agnes *et al.*, "DarkSide-50 532-day Dark Matter Search with Low-Radioactivity Argon," *Phys. Rev. D* **98** no. 10, (2018) 102006, arXiv:1802.07198 [astro-ph.CO].

[106] **DEAP** Collaboration, R. Ajaj *et al.*, "Search for dark matter with a 231-day exposure of liquid argon using DEAP-3600 at SNOLAB," *Phys. Rev. D* **100** no. 2, (2019) 022004, arXiv:1902.04048 [astro-ph.CO].

[107] E. Bagnaschi *et al.*, "Likelihood Analysis of the pMSSM11 in Light of LHC 13-TeV Data," arXiv:1710.11091 [hep-ph].

[108] F. Ruppin, J. Billard, E. Figueroa-Feliciano, and L. Strigari, "Complementarity of dark matter detectors in light of the neutrino background," *Phys. Rev. D* **90** no. 8, (2014) 083510, arXiv:1408.3581 [hep-ph].

[109] V. Chepel and H. Araújo, "Liquid noble gas detectors for low energy particle physics," *JINST* **8** no. 04, (2013) R04001–R04001.

[110] D. Acosta-Kane *et al.*, "Discovery of underground argon with low level of radioactive ^{39}Ar and possible applications to WIMP dark matter detectors," *Nucl. Instrum. Meth. A* **587** no. 1, (2008) 46–51.

[111] **ArDM** Collaboration, J. Calvo *et al.*, "Commissioning of the ArDM experiment at the Canfranc underground laboratory: first steps towards a tonne-scale liquid argon time projection chamber for Dark Matter searches," *J. Cosmol. Astropart. Phys.* **1703** no. 03, (2017) 003, arXiv:1612.06375 [physics.ins-det].

[112] C. E. Aalseth *et al.*, "DarkSide-20k: A 20 tonne two-phase LAr TPC for direct dark matter detection at LNGS," *Eur. Phys. J. Plus* **133** no. 3, (2018) 131.

[113] **EDELWEISS** Collaboration, E. Armengaud *et al.*, "Searching for low-mass dark matter particles with a massive Ge bolometer operated above-ground," *Phys. Rev. D* **99** no. 8, (2019) 082003, arXiv:1901.03588 [astro-ph.GA].

[114] **CRESST** Collaboration, A. H. Abdelhameed *et al.*, "First results from the CRESST-III low-mass dark matter program," arXiv:1904.00498 [astro-ph.CO].

[115] A. K. Drukier, K. Freese, and D. N. Spergel, "Detecting cold dark-matter candidates," *Phys. Rev. D* **33** (1986) 3495–3508.

[116] R. Bernabei *et al.*, "Searching for WIMPs by the annual modulation signature," *Phys. Lett. B* **424** no. 1, (1998) 195–201.

[117] **DAMA** Collaboration, R. Bernabei *et al.*, "First results from DAMA/LIBRA and the combined results with DAMA/NaI," *Eur. Phys. J. C* **56** (2008) 333–355, arXiv:0804.2741 [astro-ph].

[118] **DAMA/LIBRA** Collaboration, R. Bernabei *et al.*, "New results from DAMA/LIBRA," *Eur. Phys. J. C* **67** (2010) 39–49, arXiv:1002.1028 [astro-ph.GA].

[119] **DAMA/LIBRA** Collaboration, R. Bernabei *et al.*, "First model independent results from DAMA/LIBRA-phase2," *Nucl. Phys. At. Energy* **19** (2018) 307–325.

[120] **COSINE-100** Collaboration, G. Adhikari *et al.*, "Search for a Dark Matter-Induced Annual Modulation Signal in NaI(Tl) with the COSINE-100 Experiment," *Phys. Rev. Lett.* **123** no. 3, (2019) 031302, arXiv:1903.10098 [astro-ph.IM].

[121] **SABRE** Collaboration, M. Antonello *et al.*, "The SABRE project and the SABRE Proof-of-Principle," *Eur. Phys. J. C* **79** no. 4, (2019) 363, arXiv:1806.09340 [physics.ins-det].

[122] **XENON** Collaboration, E. Aprile *et al.*, "Low-mass dark matter search using ionization signals in xenon100," *Phys. Rev. D* **94** (2016) 092001.

[123] C. H. Faham *et al.*, "Measurements of wavelength-dependent double photoelectron emission from single photons in VUV-sensitive photomultiplier tubes," *JINST* **10** no. 09, (2015) P09010, arXiv:1506.08748 [physics.ins-det].

[124] S. A. Hertel, A. Biekert, J. Lin, V. Velan, and D. N. McKinsey, "A Path to the Direct Detection of sub-GeV Dark Matter Using Calorimetric Readout of a Superfluid ^{4}He Target," arXiv:1810.06283 [physics.ins-det].

[125] **COHERENT** Collaboration, D. Akimov *et al.*, "Observation of Coherent Elastic Neutrino-Nucleus Scattering," *Science* **357** no. 6356, (2017) 1123–1126, arXiv:1708.01294 [nucl-ex].

[126] J. Billard, L. Strigari, and E. Figueroa-Feliciano, "Implication of neutrino backgrounds on the reach of next generation dark matter direct detection experiments," *Phys. Rev. D* **89** no. 2, (2014) 023524, arXiv:1307.5458 [hep-ph].

[127] C. A. J. O'Hare *et al.*, "Readout strategies for directional dark matter detection beyond the neutrino background," *Phys. Rev. D* **92** (2015) 063518.

[128] L. Bergstrom, "Dark Matter Evidence, Particle Physics Candidates and Detection Methods," *Annalen Phys.* **524** (2012) 479–496, arXiv:1205.4882 [astro-ph.HE].

[129] A. Morselli, "Indirect dark-matter searches with gamma-rays: experiments status and future plans from keV to TeV," *Nuclear and Particle Physics Proceedings* **291-293** (2017) 20–24.

[130] D. Hooper and L. Goodenough, "Dark Matter Annihilation in The Galactic Center As Seen by the Fermi Gamma Ray Space Telescope," *Phys. Lett. B* **697** (2011) 412–428, arXiv:1010.2752 [hep-ph].

[131] K. N. Abazajian, N. Canac, S. Horiuchi, and M. Kaplinghat, "Astrophysical and dark matter interpretations of extended gamma-ray emission from the galactic center," *Phys. Rev. D* **90** (2014) 023526.

[132] P. Agrawal, B. Batell, P. J. Fox, and R. Harnik, "WIMPs at the Galactic Center," *J. Cosmol. Astropart. Phys.* **1505** (2015) 011, arXiv:1411.2592 [hep-ph].

[133] R. Bartels, S. Krishnamurthy, and C. Weniger, "Strong support for the millisecond pulsar origin of the Galactic center GeV excess," *Phys. Rev. Lett.* **116** no. 5, (2016) 051102, arXiv:1506.05104 [astro-ph.HE].

[134] S. K. Lee *et al.*, "Evidence for Unresolved γ-Ray Point Sources in the Inner Galaxy," *Phys. Rev. Lett.* **116** no. 5, (2016) 051103, arXiv:1506.05124 [astro-ph.HE].

[135] **SKA** Collaboration, D. J. Bacon *et al.*, "Cosmology with Phase 1 of the Square Kilometre Array: Red Book 2018: Technical specifications and performance forecasts," *Submitted to: Publ. Astron. Soc. Austral.* (2018) , arXiv:1811.02743 [astro-ph.CO].

[136] **CTA** Collaboration, B. S. Acharya *et al.*, *Science with the Cherenkov Telescope Array*. World Scientific, 2018. arXiv:1709.07997 [astro-ph.IM].

[137] **Fermi-LAT** Collaboration, M. Ackermann *et al.*, "Searching for Dark Matter Annihilation from Milky Way Dwarf Spheroidal Galaxies with Six Years of Fermi Large Area Telescope Data," *Phys. Rev. Lett.* **115** no. 23, (2015) 231301, arXiv:1503.02641 [astro-ph.HE].

[138] **PAMELA** Collaboration, O. Adriani *et al.*, "An anomalous positron abundance in cosmic rays with energies 1.5-100 GeV," *Nature* **458** (2009) 607–609, arXiv:0810.4995 [astro-ph].

[139] **Fermi-LAT** Collaboration, A. A. Abdo *et al.*, "Measurement of the Cosmic Ray e+ plus e- spectrum from 20 GeV to 1 TeV with the Fermi Large Area Telescope," *Phys. Rev. Lett.* **102** (2009) 181101, arXiv:0905.0025 [astro-ph.HE].

[140] **AMS** Collaboration, L. Accardo *et al.*, "High Statistics Measurement of the Positron Fraction in Primary Cosmic Rays of 0.5–500 GeV with the Alpha Magnetic Spectrometer on the International Space Station," *Phys. Rev. Lett.* **113** (2014) 121101.

[141] **Fermi-LAT** Collaboration, A. A. Abdo *et al.*, "Constraints on Cosmological Dark Matter Annihilation from the Fermi-LAT Isotropic Diffuse Gamma-Ray Measurement," *J. Cosmol. Astropart. Phys.* **1004** (2010) 014, arXiv:1002.4415 [astro-ph.CO].

[142] P. D. Serpico, "Astrophysical models for the origin of the positron "excess"," *Astropart. Phys.* **39-40** (2012) 2–11. Cosmic Rays Topical Issue.

[143] T. Gaisser and F. Halzen, "Icecube," *Annu. Rev. Nuc. Par. Sci.* **64** no. 1, (2014) 101–123.

[144] S. Adrián-Martínez *et al.*, "Letter of intent for KM3NeT 2.0," *J. Phys. G: Nuc. Phys.* **43** no. 8, (2016) 084001.

[145] **ANTARES** Collaboration, C. Tönnis, "Indirect searches for dark matter with the ANTARES neutrino telescope," *Proc. of Sci.* **ICRC2017** (2018) 913.

[146] F. Halzen and D. Hooper, "The indirect search for dark matter with IceCube," *New Journal of Physics* **11** no. 10, (2009) 105019.

[147] **ANTARES** Collaboration, J. de Dios Zornoza, "Dark matter search with the ANTARES neutrino telescope," *Nucl. Instrum. Meth. A* **692** (2012) 123–126, arXiv:1204.5066 [astro-ph.HE].

[148] **IceCube** Collaboration, M. G. Aartsen *et al.*, "Search for annihilating dark matter in the Sun with 3 years of IceCube data," *Eur. Phys. J. C* **77** no. 3, (2017) 146, arXiv:1612.05949 [astro-ph.HE].

[149] **LIGO and Virgo** Collaboration, B. P. Abbott *et al.*, "Observation of Gravitational Waves from a Binary Black Hole Merger," *Phys. Rev. Lett.* **116** no. 6, (2016) 061102, arXiv:1602.03837 [gr-qc].

[150] M. Aartsen *et al.*, "Multimessenger observations of a flaring blazar coincident with high-energy neutrino IceCube-170922A," *Science* **361** no. 6398, (2018) .

[151] V. Gammaldi, "Multimessenger Multi-TeV Dark Matter," *Frontiers in Astronomy and Space Sciences* **6** (2019) 19.

[152] A. Boveia and C. Doglioni, "Dark matter searches at colliders," *Annu. Rev. Nuc. Par. Sci.* **68** no. 1, (2018) 429–459.

[153] O. Buchmueller, M. J. Dolan, S. A. Malik, and C. McCabe, "Characterising dark matter searches at colliders and direct detection experiments: Vector mediators," *JHEP* **01** (2015) 037, arXiv:1407.8257 [hep-ph].

[154] D. Abercrombie *et al.*, "Dark Matter Benchmark Models for Early LHC Run-2 Searches: Report of the ATLAS/CMS Dark Matter Forum," arXiv:1507.00966 [hep-ex].

[155] S. A. Malik *et al.*, "Interplay and Characterization of Dark Matter Searches at Colliders and in Direct Detection Experiments," *Phys. Dark Univ.* **9-10** (2015) 51–58, arXiv:1409.4075 [hep-ex].

[156] M. W. Goodman and E. Witten, "Detectability of certain dark-matter candidates," *Phys. Rev. D* **31** (1985) 3059–3063.

[157] D. G. Cerdeño and A. M. Green, "Direct detection of WIMPs," *Chapter 17 of "Particle Dark Matter: Observations, Models and Searches" ed. G. Bertone, 2010, Cambridge University Press* (2010) , arXiv:1002.1912 [astro-ph.CO].

[158] J. I. Read, "The Local Dark Matter Density," *J. Phys. G: Nuc. Phys.* **41** (2014) 063101, arXiv:1404.1938 [astro-ph.GA].

[159] A. G. A. Brown *et al.*, "Gaia Data Release 2. Summary of the contents and survey properties," *Astronom. & Astrophys.* **616** (2018) A1, arXiv:1804.09365.

[160] J. H. J. Hagen and A. Helmi, "The vertical force in the solar neighbourhood using red clump stars in TGAS and RAVE. Constraints on the local dark matter density," *Astronom. & Astrophys.* **615** (2018) A99, arXiv:1802.09291 [astro-ph.GA].

[161] S. Sivertsson, H. Silverwood, J. I. Read, G. Bertone, and P. Steger, "The local dark matter density from SDSS-SEGUE G-dwarfs," *Mon. Not. R. Astron. Soc.* **478** no. 2, (2018) 1677–1693, arXiv:1708.07836 [astro-ph.GA].

[162] A. Peter, *Particle dark matter in the solar system*. PhD thesis, Princeton U., 2008.

[163] F. J. Kerr and D. Lynden-Bell, "Review of galactic constants," *Mon. Not. R. Astron. Soc.* **221** no. 4, (1986) 1023–1038.

[164] M. C. Smith *et al.*, "The RAVE Survey: Constraining the Local Galactic Escape Speed," *Mon. Not. R. Astron. Soc.* **379** (2007) 755–772, arXiv:astro-ph/0611671 [astro-ph].

[165] B. Coşkunoğlu *et al.*, "Local stellar kinematics from RAVE data - I. Local standard of rest," *Mon. Not. R. Astron. Soc.* **412** (2011) 1237–1245, arXiv:1011.1188.

[166] G. Gelmini and P. Gondolo, "WIMP annual modulation with opposite phase in Late-Infall halo models," *Phys. Rev. D* **64** (2001) 023504, arXiv:hep-ph/0012315 [hep-ph].

[167] C. Savage, K. Freese, and P. Gondolo, "Annual Modulation of Dark Matter in the Presence of Streams," *Phys. Rev. D* **74** (2006) 043531, arXiv:astro-ph/0607121 [astro-ph].

[168] A. L. Fitzpatrick, W. Haxton, E. Katz, N. Lubbers, and Y. Xu, "The Effective Field Theory of Dark Matter Direct Detection," *J. Cosmol. Astropart. Phys.* **1302** (2013) 004, arXiv:1203.3542 [hep-ph].

[169] N. Anand, A. L. Fitzpatrick, and W. C. Haxton, "Weakly interacting massive particle-nucleus elastic scattering response," *Phys. Rev. C* **89** no. 6, (2014) 065501, arXiv:1308.6288 [hep-ph].

[170] R. Machleidt and D. Entem, "Chiral effective field theory and nuclear forces," *Phys. Rep.* **503** no. 1, (2011) 1–75.

[171] **XENON** Collaboration, E. Aprile *et al.*, "First results on the scalar WIMP-pion coupling, using the XENON1T experiment," *Phys. Rev. Lett.* **122** no. 7, (2019) 071301, arXiv:1811.12482 [hep-ph].

[172] A. H. G. Peter *et al.*, "WIMP physics with ensembles of direct-detection experiments," *Phys. Dark Univ.* **5-6** (2014) 45–74.

[173] R. H. Helm, "Inelastic and Elastic Scattering of 187-Mev Electrons from Selected Even-Even Nuclei," *Phys. Rev.* **104** (1956) 1466–1475.

[174] C. McCabe, "The Astrophysical Uncertainties Of Dark Matter Direct Detection Experiments," *Phys. Rev. D* **82** (2010) 023530, arXiv:arXiv:1005.0579 [hep-ph].

[175] P. Klos, J. Menéndez, D. Gazit, and A. Schwenk, "Large-scale nuclear structure calculations for spin-dependent WIMP scattering with chiral effective field theory currents," *Phys. Rev. D* **88** no. 8, (2013) 083516, arXiv:1304.7684v4 [nucl-th]. [Erratum: Phys. Rev.D89,no.2,029901(2014)].

[176] A. Bailey, *Dark matter searches and study of electrode design in LUX and LZ.* PhD thesis, Imperial College London, 2016.

[177] **XENON** Collaboration, E. Aprile *et al.*, "Observation of two-neutrino double electron capture in ^{124}Xe with XENON1T," *Nature* **568** no. 7753, (2019) 532–535, arXiv:1904.11002 [nucl-ex].

[178] E. Majorana, "Teoria simmetrica dell'elettrone e del positrone," *Il Nuovo Cimento (1924-1942)* **14** no. 4, 171.

[179] **EXO-200** Collaboration, N. Ackerman *et al.*, "Observation of Two-Neutrino Double-Beta Decay in ^{136}Xe with EXO-200," *Phys. Rev. Lett.* **107** (2011) 212501, arXiv:1108.4193 [nucl-ex].

[180] **KamLAND-Zen** Collaboration, A. Gando *et al.*, "Measurement of the double-β decay half-life of ^{136}Xe with the KamLAND-Zen experiment," *Phys. Rev. C* **85** (2012) 045504.

[181] **EXO-200** Collaboration, J. B. Albert *et al.*, "Search for Neutrinoless Double-Beta Decay with the Upgraded EXO-200 Detector," *Phys. Rev. Lett.* **120** (2018) 072701.

[182] **KamLAND-Zen** Collaboration, A. Gando *et al.*, "Search for Majorana Neutrinos Near the Inverted Mass Hierarchy Region with KamLAND-Zen," *Phys. Rev. Lett.* **117** (2016) 082503.

[183] **NEXT** Collaboration, J. Martín-Albo *et al.*, "Sensitivity of NEXT-100 to neutrinoless double beta decay," *JHEP* **2016** no. 5, (2016) 159.

[184] J. Meija *et al.*, "Atomic weights of the elements 2013 (IUPAC Technical Report)," *Pure and Applied Chemistry* **88** (2016) 265–291.

[185] **LUX** Collaboration, D. S. Akerib *et al.*, "Limits on spin-dependent WIMP-nucleon cross section obtained from the complete LUX exposure," *Phys. Rev. Lett.* **118** no. 25, (2017) 251302, `arXiv:1705.03380 [astro-ph.CO]`.

[186] **XENON100** Collaboration, E. Aprile *et al.*, "XENON100 Dark Matter Results from a Combination of 477 Live Days," *Phys. Rev. D* **94** no. 12, (2016) 122001, `arXiv:1609.06154 [astro-ph.CO]`.

[187] A. Shukla, P. Raina, and P. K. Rath, "Study of two neutrino beta(+)beta(+)/beta(+) ec/ecec decay of xe-124,xe-126 and ba-130,ba-132 for 0(+) -> 0(+) transition in phfb model," *J. Phys. G: Nuc. Phys.* **34** (2007) 549–563.

[188] N. Barros, J. Thurn, and K. Zuber, "Double beta decay searches of ^{134}Xe, ^{126}Xe and ^{124}Xe with large scale Xe detectors," *J. Phys. G: Nuc. Phys.* **G41** no. 11, (2014) 115105, `arXiv:1409.8308 [nucl-ex]`.

[189] **EXO-200** Collaboration, J. B. Albert *et al.*, "Improved measurement of the $2\nu\beta\beta$ half-life of ^{136}Xe with the EXO-200 detector," *Phys. Rev. C* **89** no. 1, (2014) 015502, `arXiv:1306.6106 [nucl-ex]`.

[190] L. Baudis, A. Kish, F. Piastra, and M. Schumann, "Cosmogenic activation of xenon and copper," *Eur. Phys. J. C* **75** no. 10, (2015) 485, `arXiv:1507.03792 [astro-ph.IM]`.

[191] "High-accuracy measurement of the emission spectrum of liquid xenon in the vacuum ultraviolet region," *Nucl. Instrum. Meth. A* **795** (2015) 293–297.

[192] A. Hitachi *et al.*, "Effect of ionization density on the time dependence of luminescence from liquid argon and xenon," *Phys. Rev. B* **27** (1983) 5279–5285.

[193] E. Conti *et al.*, "Correlated fluctuations between luminescence and ionization in liquid xenon," *Phys. Rev. B* **68** (2003) 054201.

[194] P. Sorensen and C. E. Dahl, "Nuclear recoil energy scale in liquid xenon with application to the direct detection of dark matter," *Phys. Rev. D* **83** (2011) 063501, `arXiv:1101.6080 [astro-ph.IM]`.

[195] C. E. Dahl, *The physics of background discrimination in liquid xenon, and first results from Xenon10 in the hunt for WIMP dark matter*. PhD thesis, Princeton University, 2009.

[196] T. Shutt, C. Dahl, J. Kwong, A. Bolozdynya, and P. Brusov, "Performance and fundamental processes at low energy in a two-phase liquid xenon dark matter detector," *Nucl. Instrum. Meth. A* **579** no. 1, (2007) 451–453.

[197] J. Lindhard, M. Scharff, and H. Schioett, "Range concepts and heavy ion ranges," *Kgl. Danske Videnskab. Selskab. Mat. Fys. Medd.* **33** no. 14, (1963) .

[198] **LUX** Collaboration, D. S. Akerib *et al.*, "Tritium calibration of the LUX dark matter experiment," *Phys. Rev. D* **93** no. 7, (2016) 072009, arXiv:1512.03133 [physics.ins-det].

[199] **LUX** Collaboration, D. S. Akerib *et al.*, "Ultralow energy calibration of LUX detector using ^{127}Xe electron capture," *Phys. Rev. D* **96** no. 11, (2017) 112011, arXiv:1709.00800 [physics.ins-det].

[200] E. M. Boulton *et al.*, "Calibration of a two-phase xenon time projection chamber with a ^{37}Ar source," *JINST* **12** no. 08, (2017) P08004, arXiv:1705.08958 [physics.ins-det].

[201] **LUX** Collaboration, D. S. Akerib *et al.*, "Low-energy (0.7-74 keV) nuclear recoil calibration of the LUX dark matter experiment using D-D neutron scattering kinematics," arXiv:1608.05381 [physics.ins-det].

[202] M. Szydagis, A. Fyhrie, D. Thorngren, and M. Tripathi, "Enhancement of NEST Capabilities for Simulating Low-Energy Recoils in Liquid Xenon," *JINST* **8** (2013) C10003, arXiv:1307.6601 [physics.ins-det].

[203] J. Brodsky *et al.*, "Noble Element Simulation Technique (code),". https://github.com/NESTCollaboration/nest.

[204] B. Lenardo *et al.*, "Measurement of the ionization yield from nuclear recoils in liquid xenon between 0.3–6 keV with single-ionization-electron sensitivity," arXiv:1908.00518 [physics.ins-det].

[205] M. Szydagis and G. Rischbieter, "Noble Element Simulation Technique (public note),". https://drive.google.com/file/d/1urVT3htFjIC1pQKyaCcFonvWLt74Kgvn/view.

[206] B. López Paredes *et al.*, "Response of photomultiplier tubes to xenon scintillation light," *Astropart. Phys.* **102** (2018) 56–66, arXiv:1801.01597 [physics.ins-det].

[207] V. N. Solovov *et al.*, "Position Reconstruction in a Dual Phase Xenon Scintillation Detector," *IEEE* **59** no. 6, (2012) 3286–3293, arXiv:1112.1481.

[208] **LUX** Collaboration, D. S. Akerib *et al.*, "Calibration, event reconstruction, data analysis, and limit calculation for the LUX dark matter experiment," *Phys. Rev. D* **97** no. 10, (2018) 102008, arXiv:1712.05696 [physics.ins-det].

[209] J. Heise, "The Sanford Underground Research Facility at Homestake," *J. Phys. Conf. Ser.* **606** no. 1, (2015) 012015, arXiv:1503.01112 [physics.ins-det].

[210] F. Neves *et al.*, "Measurement of the absolute reflectance of polytetrafluoroethylene (PTFE) immersed in liquid xenon," *JINST* **12** no. 01, (2017) P01017, arXiv:1612.07965 [physics.ins-det].

[211] J. Haefner *et al.*, "Reflectance dependence of polytetrafluoroethylene on thickness for xenon scintillation light," *Nucl. Instrum. Meth.* **A856** (2017) 86–91, arXiv:1608.01717 [physics.ins-det].

[212] **LZ** Collaboration, D. S. Akerib *et al.*, "Identification of Radiopure Titanium for the LZ Dark Matter Experiment and Future Rare Event Searches," *Astropart. Phys.* **96** (2017) 1–10, arXiv:1702.02646 [physics.ins-det].

[213] D. S. Akerib *et al.*, "An Ultra-Low Background PMT for Liquid Xenon Detectors," *Nucl. Instrum. Meth. A* **703** (2013) 1–6, arXiv:1205.2272 [physics.ins-det].

[214] **XENON** Collaboration, E. Aprile *et al.*, "Lowering the radioactivity of the photomultiplier tubes for the XENON1T dark matter experiment," *Eur. Phys. J. C* **75** no. 11, (2015) 546, arXiv:1503.07698 [astro-ph.IM].

[215] M. Yeh, A. Garnov, and R. Hahn, "Gadolinium-loaded liquid scintillator for high-precision measurements of antineutrino oscillations and the mixing angle, $\theta 13$," *Nucl. Instrum. Meth. A* **578** no. 1, (2007) 329–339.

[216] Y. Ding *et al.*, "A new gadolinium-loaded liquid scintillator for reactor neutrino detection," *Nucl. Instrum. Meth. A* **584** no. 1, (2008) 238–243.

[217] **GEANT4** Collaboration, S. Agostinelli *et al.*, "GEANT4: A Simulation toolkit," *Nucl. Instrum. Meth. A* **506** (2003) 250–303.

[218] N. Bozorgnia *et al.*, "Opening the energy window on direct dark matter detection," *J. Cosmol. Astropart. Phys.* **1812** no. 12, (2018) 013, arXiv:1810.05576 [hep-ph].

[219] E. Aprile *et al.*, "Design and performance of the XENON10 dark matter experiment," *Astropart. Phys.* **34** no. 9, (2011) 679–698, arXiv:1001.2834 [astro-ph.IM].

[220] V. N. Lebedenko *et al.*, "Result from the First Science Run of the ZEPLIN-III Dark Matter Search Experiment," *Phys. Rev. D* **80** (2009) 052010, arXiv:0812.1150 [astro-ph].

[221] D. S. Akerib *et al.*, "Radiogenic and Muon-Induced Backgrounds in the LUX Dark Matter Detector," *Astropart. Phys.* **62** (2015) 33–46, arXiv:1403.1299 [astro-ph.IM].

[222] "Table de Radioncléides (LNHB),". http://www.nucleide.org/DDEP_WG/Nuclides/Pb-214_tables.pdf.

[223] **LUX** Collaboration, D. S. Akerib *et al.*, "Chromatographic separation of radioactive noble gases from xenon," *Astropart. Phys.* **97** (2018) 80–87, arXiv:1605.03844 [physics.ins-det].

[224] **Gargamelle** Collaboration, F. Hasert *et al.*, "Observation of neutrino-like interactions without muon or electron in the Gargamelle neutrino experiment," *Phys. Lett. B* **46** no. 1, (1973) 138–140.

[225] J. N. Bahcall and C. Pena-Garay, "Solar models and solar neutrino oscillations," *New J. Phys.* **6** (2004) 63, arXiv:hep-ph/0404061 [hep-ph].

[226] J.-W. Chen *et al.*, "Low-energy electronic recoil in xenon detectors by solar neutrinos," *Phys. Lett. B* **774** (2017) 656–661, arXiv:1610.04177 [hep-ex].

[227] G. Cowan, *Statistical Data Analysis*. Oxford University Press, 1997.

[228] G. Cowan, K. Cranmer, E. Gross, and O. Vitells, "Asymptotic formulae for likelihood-based tests of new physics," *Eur. Phys. J. C* **71** (2011) 1554, arXiv:1007.1727 [physics.data-an].

[229] E. Gross and O. Vitells, "Trial factors for the look elsewhere effect in high energy physics," *Eur. Phys. J. C* **70** (2010) 525–530, arXiv:1005.1891 [physics.data-an].

[230] W. A. Rolke, A. M. Lopez, and J. Conrad, "Limits and confidence intervals in the presence of nuisance parameters," *Nucl. Instrum. Meth. A* **A551** (2005) 493–503, arXiv:physics/0403059 [physics].

[231] S. Wilks, "The Large-Sample Distribution of the Likelihood Ratio for Testing Composite Hypotheses," *The Annals of Mathematical Statistics* **9** no. 1, (1938) 60–62.

[232] G. J. Feldman and R. D. Cousins, "A Unified approach to the classical statistical analysis of small signals," *Phys. Rev. D* **57** (1998) 3873–3889, arXiv:physics/9711021 [physics.data-an].

[233] I. Antcheva *et al.*, "ROOT: A C++ framework for petabyte data storage, statistical analysis and visualization," *Comput. Phys. Commun.* **180** (2009) 2499–2512, arXiv:1508.07749 [physics.data-an].

[234] L. Moneta, K. Belasco, K. S. Cranmer, S. Kreiss, A. Lazzaro, D. Piparo, G. Schott, W. Verkerke, and M. Wolf, "The RooStats Project," *Proc. of Sci.* **ACAT2010** (2010) 057, arXiv:1009.1003 [physics.data-an].

[235] N. Metropolis, A. W. Rosenbluth, M. N. Rosenbluth, A. H. Teller, and E. Teller, "Equation of state calculations by fast computing machines," *J. Chem. Phys.* **21** no. 6, (1953) 1087–1092.

[236] W. K. Hastings, "Monte Carlo sampling methods using Markov chains and their applications," *Biometrika* **57** no. 1, (1970) 97–109.

[237] C. M. Bishop, *Pattern Recognition and Machine Learning*. Springer-Verlag, 2006.

[238] J. N. Bahcall and A. M. Serenelli, "How Do Uncertainties in the Surface Chemical Composition of the Sun Affect the Predicted Solar Neutrino Fluxes?," *Astrophys. J.* **626** no. 1, (2005) 530–542.

[239] "Table de Radioncléides (LNHB),". http://www.nucleide.org/DDEP_WG/Nuclides/Pb-212_tables.pdf.

[240] J. Kotila and F. Iachello, "Phase space factors for double-β decay," *Phys. Rev. C* **85** (2012) 034316, arXiv:1209.5722 [nucl-th].

[241] M. Selvi, "Review of Monte Carlo simulations for backgrounds from radioactivity," *AIP Conference Proceedings* **1549** no. 1, (2013) 213–218.

[242] **SNO** Collaboration, B. Aharmim *et al.*, "Combined Analysis of all Three Phases of Solar Neutrino Data from the Sudbury Neutrino Observatory," *Phys. Rev. C* **88** (2013) 025501, `arXiv:1109.0763 [nucl-ex]`.

[243] S. Horiuchi, J. F. Beacom, and E. Dwek, "Diffuse supernova neutrino background is detectable in super-kamiokande," *Phys. Rev. C* **79** (2009) 083013.

[244] K. Okumura *et al.*, "Measurements of the atmospheric neutrino flux by super-kamiokande: energy spectra, geomagnetic effects, and solar modulation," *J. Phys.: Conf. Ser.* **888** (2017) 012116.

[245] **XENON** Collaboration, E. Aprile *et al.*, "First Dark Matter Search Results from the XENON1T Experiment," *Phys. Rev. Lett.* **119** no. 18, (2017) 181301, `arXiv:1705.06655 [astro-ph.CO]`.

[246] A. L. Read, "Modified frequentist analysis of search results (The CL(s) method)," in *Workshop on confidence limits, CERN, Geneva, Switzerland, 17-18 Jan 2000: Proceedings*, pp. 81–101. 2000.

[247] G. Cowan, K. Cranmer, E. Gross, and O. Vitells, "Power-Constrained Limits," `arXiv:1105.3166 [physics.data-an]`.

[248] **GAMBIT** Collaboration, P. Athron *et al.*, "A global fit of the MSSM with GAMBIT," *Eur. Phys. J. C* **77** no. 12, (2017) 879, `arXiv:1705.07917 [hep-ph]`.

[249] **ATLAS** Collaboration, M. Aaboud *et al.*, "Search for dark matter at $\sqrt{s} = 13$ TeV in final states containing an energetic photon and large missing transverse momentum with the ATLAS detector," *Eur. Phys. J. C* **77** no. 6, (2017) 393, `arXiv:1704.03848 [hep-ex]`.

[250] **CMS** Collaboration, A. M. Sirunyan *et al.*, "Search for dark matter produced with an energetic jet or a hadronically decaying W or Z boson at $\sqrt{s} = 13$ TeV," *JHEP* **07** (2017) 014, `arXiv:1703.01651 [hep-ex]`.

[251] **XENON** Collaboration, E. Aprile *et al.*, "Constraining the spin-dependent WIMP-nucleon cross sections with XENON1T," *Phys. Rev. Lett.* **122** no. 14, (2019) 141301, `arXiv:1902.03234 [astro-ph.CO]`.

[252] **PandaX-II** Collaboration, J. Xia *et al.*, "PandaX-II Constraints on Spin-Dependent WIMP-Nucleon Effective Interactions," *Phys. Lett. B* **792** (2019) 193–198, `arXiv:1807.01936 [hep-ex]`.

[253] **PICO** Collaboration, C. Amole *et al.*, "Dark Matter Search Results from the Complete Exposure of the PICO-60 C_3F_8 Bubble Chamber," `arXiv:1902.04031 [astro-ph.CO]`.

[254] **Super-Kamiokande** Collaboration, K. Choi *et al.*, "Search for neutrinos from annihilation of captured low-mass dark matter particles in the Sun by Super-Kamiokande," *Phys. Rev. Lett.* **114** no. 14, (2015) 141301, `arXiv:1503.04858 [hep-ex]`.

[255] G. Monari *et al.*, "The escape speed curve of the Galaxy obtained from Gaia DR2 implies a heavy Milky Way," *Astropart. Phys.* **616** (2018) L9, arXiv:1807.04565 [astro-ph.GA].

[256] L. E. Strigari, "Galactic Searches for Dark Matter," *Phys. Rep.* **531** (2013) 1–88, arXiv:1211.7090 [astro-ph.CO].

[257] A. M. Green, "Astrophysical uncertainties on the local dark matter distribution and direct detection experiments," *J. Phys. G: Nuc. Phys.* **44** no. 8, (2017) 084001, arXiv:1703.10102 [astro-ph.CO].

[258] N. W. Evans, C. A. J. O'Hare, and C. McCabe, "Refinement of the standard halo model for dark matter searches in light of the Gaia Sausage," *Phys. Rev. D* **99** no. 2, (2019) 023012, arXiv:1810.11468 [astro-ph.GA].

[259] **GRAVITY** Collaboration, R. Abuter *et al.*, "Detection of the gravitational redshift in the orbit of the star S2 near the Galactic centre massive black hole," *Astronom. & Astrophys.* **615** (2018) L15, arXiv:1807.09409 [astro-ph.GA].

[260] L. Necib, M. Lisanti, and V. Belokurov, "Inferred Evidence for Dark Matter Kinematic Substructure with SDSS–Gaia," *Astrophys. J.* **874** no. 1, (2019) 3, arXiv:1807.02519.

[261] N. Bozorgnia *et al.*, "The dark matter component of the Gaia radially anisotropic substructure," arXiv:1910.07536 [astro-ph.GA].

[262] **LUX** Collaboration, D. S. Akerib *et al.*, "3D Modeling of Electric Fields in the LUX Detector," *JINST* **12** no. 11, (2017) P11022, arXiv:1709.00095 [physics.ins-det].

[263] K. Cranmer, "Practical Statistics for the LHC," in *Proceedings, 2011 European School of High-Energy Physics (ESHEP 2011)*, pp. 267–308. 2015. arXiv:1503.07622 [physics.data-an].

[264] C. Strege *et al.*, "Fundamental statistical limitations of future dark matter direct detection experiments," *Phys. Rev. D* **86** (2012) 023507.

[265] L. E. Strigari and R. Trotta, "Reconstructing WIMP Properties in Direct Detection Experiments Including Galactic Dark Matter Distribution Uncertainties," *JCAP* **0911** (2009) 019, arXiv:0906.5361 [astro-ph.HE].

[266] M. Pato, L. E. Strigari, R. Trotta, and G. Bertone, "Taming astrophysical bias in direct dark matter searches," *J. Cosmol. Astropart. Phys.* **1302** (2013) 041, arXiv:1211.7063 [astro-ph.CO].